

SPECTRALLY SELECTIVE FILTERS WITH ROUGH SURFACES AND  
MULTILAYER COATINGS

by

NILOUFAR PIROUZFAM

Submitted to the Graduate School of Sabanci University in partial fulfilment of the  
requirements for the degree of Doctor of Philosophy

Sabanci University  
June 2022

© Niloufar Pirouzfam 2022

All Rights Reserved

## ABSTRACT

### SPECTRALLY SELECTIVE FILTERS WITH ROUGH SURFACES AND MULTILAYER COATINGS

NILOUFAR PIROUZFAM

Ph.D. Thesis, June 2022

Supervisor: Prof. Dr. Ibrahim Kürşat Şendur

Keywords: Spectrally selective filters, electromagnetic spectrum, rough surfaces, colored radiative cooling, black silicon

Due to the energy crisis and major environmental concerns, new energy sources are being researched for environmentally friendly and efficient energy conversion and consumption techniques. Optical surfaces, which have shown remarkable promise and are presently being applied globally, are among of the promising technologies for energy management. The reflectance, absorption, and transmission characteristics of an object are determined by the material and structural parameters of the object. Impact of surface texture on optical performance of the surface is unavoidable. In order to alter the spectral features (transmission, reflection, and absorption) of light, light-matter interactions can be altered by multilayer coatings, nanostructures, and rough surfaces. As a result, design of micro and nano structures that can act as spectrally selective filters for reflection and emission over a broadband spectrum became an important consideration. The purpose of this thesis is to provide design methodologies for spectral selective emission surfaces with various applications, such as spectrally selective filters with rough surfaces and multilayer coatings, colored radiative cooling, and absorption mechanism of black silicon, which in all of them it is required to do surface engineering to do spectrally selective in both broadband and narrowband. Various aspects are evaluated throughout the designing process and used to assess the generated characteristics. The methods utilized in this thesis create innovative designs that may be used in a variety of applications.

## ÖZET

### PÜRÜZLÜ YÜZEYLER VE ÇOK KATMANLI KAPLAMALI SPEKRAL SEÇİCİ FİLTRELER

Niloufar Pirouzfam

Doktora Tezi, Haziran 2022

Tez Danışmanı: Prof. Dr. İbrahim Kürşat Şendur

Anahtar Kelimeler: Spektral olarak seçici, elektromanyetik tayf, ışımsal soğutma, siyah silikon

Enerji krizi ve büyük çevresel kaygılar nedeniyle, çevre dostu ve verimli enerji dönüşüm ve tüketim teknikleri için yeni enerji kaynakları araştırılmaktadır. Dikkat çekici umutlar veren ve şu anda dünya çapında uygulanmakta olan optik yüzeyler, enerji yönetimi için gelecek vaat eden teknolojiler arasındadır. Bir nesnenin yansıtma, soğurma ve iletme özellikleri, nesnenin malzeme ve yapısal parametreleri tarafından belirlenir. Yüzey dokusunun yüzeyin optik performansı üzerindeki etkisi kaçınılmazdır. Işığın spektral özelliklerini (iletim, yansıma ve absorpsiyon) değiştirmek için, ışık-madde etkileşimleri çok katmanlı kaplamalar, nano yapılar ve pürüzlü yüzeyler tarafından değiştirilebilir. Sonuç olarak, geniş bant spektrumu üzerinde yansıma ve emisyon için spektral olarak seçici filtreler olarak hareket edebilen mikro ve nano yapıların tasarımı önemli bir husus haline geldi. Bu tezin amacı, pürüzlü yüzeyli ve çok katmanlı kaplamalı spektral seçici filtreler, renkli ışınımlı soğutma ve hepsinde gerekli olan siyah silikonun absorpsiyon mekanizması gibi çeşitli uygulamalarla spektral seçici emisyon yüzeyleri için tasarım metodolojileri sağlamaktır. Hem geniş bantta hem de dar bantta spektral seçicilik yapmak için yüzey mühendisliği yapmak. Tasarım süreci boyunca çeşitli yönler değerlendirilir ve oluşturulan özellikleri değerlendirmek için kullanılır. Bu tezde kullanılan yöntemler, çeşitli uygulamalarda kullanılabilecek yenilikçi tasarımlar yaratmaktadır.

## ACKNOWLEDGEMENT

My Ph.D. is a journey that has involved the support of numerous people. I would like to take this opportunity to express my gratitude to everyone who has contributed to the successful completion of my Ph.D. I would especially like to further recognize certain people who have made a noticeable impact to help me accomplish this extraordinary milestone.

First and foremost, I would like to thank my advisor, Prof. Dr. Kurşat Şendur for accepting me as graduate student in his research group. His mentorship and guidance over the years have played a vital role in my growth as a researcher and individual. He always supports me not only in research but also in my personal life during my stay in Turkey. I am confident that I will continue to use the skillsets I developed working with him well after graduate school.

Additionally, I would also like to thank my committee members, Prof. Dr. Ali Koşar and Prof. Dr. Burç Misirlioğlu for attending my doctoral defense. They not only gave me many practical suggestions for improving my work, but also always generously gave their time and consulting me which allowing me to improve my project. I also have been fortunate to learn from Prof. Dr. Pinar Menguç during my PhD. He is one of the best in my research field and it was honor for me to have his idea in my research.

I would like to recognize all my amazing friends who have brought joy into this memorable journey. I cannot fully express what your friendship has meant to me over the years. You were all there to cheer me on when things got tough, and you were there to celebrate when a milestone was reached. I cannot imagine this part of my life without you in it. To my friends, thank you for your friendship up to this point, and I look forward to many more conversations, laughter, and activities with you all.

Lastly, I would like to convey my deepest gratitude to my husband, my parents and brother. Mom and Dad, you have always motivated me to be the best version of myself and to use my talents to benefit others. Your unconditional love and encouragement were an essential source of energy to get me through the toughest times. Thank you for all your sacrifice and for being my greatest inspiration. You have supported me in so many ways throughout my life and I am so proud to be your sister. My wonderful husband Ali, thank you for your constant love and support. Thank you for your always being by my side and never failing to make me laugh. You are not only my husband you are my best friend in my life, and I am very happy to have you in my life. I love you with all of my heart, soul, and spirit.

## **DEDICATION**

This dissertation is dedicated to my amazing family for their love and support, and my love Ali who has been a source of support and encouragement.

## TABLE OF CONTENTS

<b>ACKNOWLEDGEMENT</b> .....	<b>iii</b>
<b>DEDICATION</b> .....	<b>iv</b>
<b>LIST OF FIGURES</b> .....	<b>vii</b>
<b>LIST OF TABLES</b> .....	<b>xi</b>
<b>1. INTRODUCTION</b> .....	<b>1</b>
1.1. Background & Motivation.....	1
1.2. Literature Survey .....	4
1.2.1. Spectrally Selective Absorbers.....	4
1.2.2. Colored radiative cooling .....	6
1.2.3. Broadband Absorption in deterministic and rough surfaces .....	9
1.3. Aims & Objectives .....	12
1.4. Contributions .....	13
1.5. Thesis Outline.....	16
<b>2. TUNGSTEN BASED SPECTRALLY SELECTIVE ABSORBERS WITH ANISOTROPIC ROUGH SURFACE TEXTURE</b> .....	<b>17</b>
2.1. Materials and Methods .....	18
2.2. Results and Discussion.....	23
<b>3. COLORAZATION OF PASSIVE RADIATIVE COOLING COATINGS USING PLASMONIC EFFECTS</b> .....	<b>32</b>
3.1. Materials and Methods .....	32
3.1.1. Principle of Radiative Cooling.....	33
3.1.2. Principle of Color Display.....	37
3.2. Results and discussion .....	41

<b>4. ORIGINS OF THE ENHANCED BROADBAND ABSORPTION IN BLACK SILICON .....</b>	<b>49</b>
4.1. Methodology.....	50
4.1.1. Rough Surface Generation .....	50
4.1.2. Optical Properties .....	53
4.2. Results & Discussions .....	58
<b>5. CONCLUSION .....</b>	<b>72</b>
<b>6. FUTURE WORK.....</b>	<b>75</b>
<b>BIBLIOGRAPHY .....</b>	<b>76</b>



## LIST OF FIGURES

Figure 2.1: Schematic of proposed selective absorber (a) Solar radiation spectrum (b) Comparison of absorption spectrum for flat surface and rough surface (c) Scattering from isotropic random rough surface (d) Scattering from anisotropic random rough surfaces (e) Top view of isotropic rough surface (f) Top view of anisotropic rough surface.....	19
Figure 2. 2: The real and imaginary part of the permittivity of the Tungsten .....	22
Figure 2. 3: Anisotropic random roughness texture formed by random Gaussians .....	23
Figure 2. 4: Comparing Absorbance of Flat and rough ( $l_x=100$ nm, $l_y=100$ nm and $h=50$ nm) Tungsten finite thickness film by FDTD solution.....	24
Figure 2. 5: The effect of (a) Correlation length and (b) RMS height in the absorption spectra of an isotropic random rough surface of Tungsten.....	26
Figure 2. 6: The RMS height effect on bandwidth of absorbance .....	27
Figure 2.7: (a) The effect of correlation length for W anisotropic rough surface (b) Isotropic rough surface with $l=200$ nm and $h=100$ nm. (c) Anisotropic rough surface with $l_x=100$ nm, $l_y= 400$ nm, and $h=100$ nm. (d) Anisotropic rough surface with $l_x=200$ nm, $l_y=400$ nm, and $h=100$ nm .....	28
Figure 2.8: The RMS height effect on the absorbance of the anisotropic rough surface of Tungsten with $l_x=100$ nm, $l_y=400$ nm.....	29
Figure 2. 9: Polarization direction effect on absorption spectrum for (a) isotropic surface ( $l= 200$ nm, $h=180$ nm) (b) anisotropic surface ( $l_x=100$ nm, $l_y= 400$ nm, and $h=180$ nm) .....	30

Figure 2.10: Absorbance spectrum regarding to different incidence angles for an isotropic random rough surface .....	31
Figure 3.1: Schematic of designed non-color radiative cooling.....	46
Figure 3.2: The ideal optical response of radiative cooling, AM 1.5 solar spectrum (red) and atmosphere transmission (blue) .....	37
Figure 3.3: (a) Schematic diagram of Colored radiative cooling structure (b) exploded view of bowtie nanoantenna on top of reflector layers (c) color place in chromaticity diagram (d) reflection spectrum of non-color and color radiative cooling.....	39
Figure 3.4: (a) Reflection spectrum of layered radiative cooling with a various number of layers for non-color radiative cooling design. (c) The cooling power corresponds to each layered radiative cooling.....	42
Figure 3.5:(a) The reflection spectra of various colored radiative coolers structures at the normal incident (b) the corresponding colors of structures in the chromaticity diagram. (c) the displayed color of colored radiative cooling structures.....	44
Figure 3.6: (a)-(d) Gap effect of nanoantenna on reflection spectrum. (e)-(h) Length effect of nanoantenna on the reflection spectrum. (i)-(l) Height effect of nanoantenna on the reflection spectrum .....	46
Figure 3.7: The electric field around bow tie nano antennas for different gap size. (a)-(d) $g=20$ nm (e)-(h) $g=30$ nm (i)-(l) $g= 50$ nm.....	47
Figure 3.8: Reflection field as a function of (a) angular emission and wavelength (b) thickness of nanoantenna and wavelength (c) resultant colors from various nanoantenna thickness.....	48
Figure 4. 1: a) Example 3D visual of random texture formed by random Gaussians. b) Example 3D visual of periodicity controlled deterministic texture. c) 2D scheme for random texture with geometric parameters. d) 2D scheme for deterministic texture with geometric parameters.....	50

Figure 4.2: Random roughness texture generated by different PSD functions (a) Gaussian spectrum (b) Power-Law spectrum (c) Exponential spectrum. ....	53
Figure 4. 3: a) Real and imaginary part of the permittivity of the undoped silicon retrieved from [56]. b) Reflectance, transmittance and absorptance of Si film of finite thickness. ....	54
Figure 4. 4: a-b-c) Comparison of real and imaginary part of the permittivity given in [56] and fit values for undoped silicon, and reflectance obtained from it and the fit. ....	56
Figure 4. 5: a-b) Imaginary part of the permittivity of Si with doping concentrations of $1.5 \times 10^{10}$ , $10^{14}$ , $5 \times 10^{15} \text{ cm}^{-3}$ . c) Absorptivity of silicon with carrier concentrations of $1.5 \times 10^{10}$ , $10^{14}$ , $5 \times 10^{15} \text{ cm}^{-3}$ . ....	57
Figure 4. 6: a) An example random texture generated by setting $l = 0.1 \text{ } \mu\text{m}$ , $h_{\text{rms}} = 0.3 \text{ } \mu\text{m}$ , $p = 1 \text{ } \mu\text{m}$ . b) An example random texture generated by setting $l = 1.1 \text{ } \mu\text{m}$ , $h_{\text{rms}} = 0.8 \text{ } \mu\text{m}$ , $p = 4 \text{ } \mu\text{m}$ . c) An example random texture generated by setting $l = 0.6 \text{ } \mu\text{m}$ , $h_{\text{rms}} = 0.8 \text{ } \mu\text{m}$ , $p = 4 \text{ } \mu\text{m}$ . ....	59
Figure 4. 7: a) Comparison of spectral absorption of untextured (film) and textures silicon with varying $l$ and $h_{\text{rms}}$ . b) $ E(\lambda) ^2$ distribution of untextured Si. c) $ E(\lambda) ^2$ distribution of textured silicon with $l = 0.1 \text{ } \mu\text{m}$ and $h_{\text{rms}} = 0.3 \text{ } \mu\text{m}$ . d) $ E(\lambda = 0.5 \text{ } \mu\text{m}) ^2$ distribution of the texture with $l = 1.1 \text{ } \mu\text{m}$ , $h_{\text{rms}} = 0.8 \text{ } \mu\text{m}$ at $\lambda = 0.5 \text{ } \mu\text{m}$ . ....	60
Figure 4. 8: a) Spectral absorptions of random textures for $N = 10^{14}$ and $5 \times 10^{15} \text{ cm}^{-3}$ . b-c) Spatial absorption profiles for $N = 10^{14}$ and $5 \times 10^{15} \text{ cm}^{-3}$ at $\lambda = 0.5 \text{ } \mu\text{m}$ . d) Absorption of a random texture and deterministic texture with varying $p$ for $N = 5 \times 10^{15} \text{ cm}^{-3}$ . e) $ E(\lambda = 0.5 \text{ } \mu\text{m}) ^2$ distribution for the deterministic texture with $p = 1 \text{ } \mu\text{m}$ . ....	61
Figure 4.9: a-b-c) $ E(\lambda) ^2$ at wavelengths of 0.75, 1.5 and 3 $\mu\text{m}$ for the pyramid dimensions of $p = 1 \text{ } \mu\text{m}$ , $h = 3 \text{ } \mu\text{m}$ and carrier concentration of $10^{14} \text{ cm}^{-3}$ ....	62
Figure 4.10: a-b-c) $ E(\lambda) ^2 \times \sigma(\lambda)$ at wavelengths of 0.75, 1.5 and 3 $\mu\text{m}$ for the pyramid dimensions of $p = 1 \text{ } \mu\text{m}$ , $h = 3 \text{ } \mu\text{m}$ and carrier concentration of $10^{14} \text{ cm}^{-3}$ ....	63
Figure 4.11: Scheme for analogy between silicon pyramid and stacked half-wave antennas ....	64

Figure 4.12: a) Representation of individual half-wave antenna with thickness  $2R$  and length  $L$ , on the pyramid silicon. b) Calculated resonance condition for varying  $R$  values and corresponding  $L$  values. Lower and upper bounds of the error bars stand for  $R = \lambda/50$  and  $\lambda/20$ .  $L = \lambda_{\text{Eff}}/2$  values are obtained at  $R = \lambda_1/45$ ,  $R = \lambda_2/37$  and  $R = \lambda_3/22$  which is equal to the width of the pyramid where first side mode occurs. .... 65

Figure 4.13: a-b-c)  $|E(\lambda)|^2$  distributions at  $\lambda = 3 \mu\text{m}$  wavelength for  $p = 1 \mu\text{m}$ ,  $2 \mu\text{m}$  and  $4 \mu\text{m}$  respectively. d-e-f)  $|E(\lambda)|^2 \times \sigma(\lambda)$  distributions at  $\lambda = 3 \mu\text{m}$  wavelength for  $p = 1 \mu\text{m}$ ,  $2 \mu\text{m}$  and  $4 \mu\text{m}$  respectively. .... 67

Figure 4.14: a) Scheme for the black silicon as a waveguide problem composed of high index (core) and low index (cladding). b-c-d) Dispersion diagrams for  $d = 0.06, 0.2$  and  $0.35 \mu\text{m}$  at which effective wavelength matching condition is satisfied for wavelengths of  $0.5, 1.5$  and  $3 \mu\text{m}$  wavelengths. .... 68

Figure 4.15: a-b-c) Dispersion diagrams for  $d = 0.7, 1$  and  $2 \mu\text{m}$  and supported TM modes with cut-off wavelengths labeled ..... 70

## LIST OF TABLES

Table 3.1. Cost function definitions in thickness optimization using GA optimization.	36
Table 3.2: Detailed cooling power performance of conventional and colored coolers at a normal incident .....	45
Table 4. 1: List of parameters and their values for fitting Drude-Lorentz formalism given in Eq. (3) to optical properties of Si given in [55] .....	55

# 1. INTRODUCTION

## 1.1. Background & Motivation

All objects emit energy, which propagates as electromagnetic (EM) waves. As the EM waves encounter matter, incident energy on the material is either reflected, absorbed, or transmitted. Based on the geometrical and materials features of the object, transmission, reflection, and absorption is altered by objects ability to tailor interactions between light and matter. Transmission, reflection, and absorption by the object is also affected by the wavelength or frequency. Because spectrum information is significantly influenced by the object's structural characteristics, such as shape, size, and periodicity on the surface, optical characteristics are very sensitive to these parameters. A detailed and systematic assessment of these geometric and materials parameters on the spectral reflection, transmission and absorption of surfaces is necessary.

Radiative characteristics of surfaces are influenced by several factors, including surface roughness and degree of polish, material purity, and the thickness of any thin layer (e.g., oxide) or paint coating on the surface. Surface reflectance and emissivity throughout the electromagnetic spectrum can be modified by optical structures. This spectral light modification can be accomplished by nano structuring of surfaces, which can significantly alter their optical characteristics [1,2]. With recent developments in solar thermal [3] and thermophotovoltaic [4] systems, as well as broadband reflection/emission [5] applications, surface structure engineering, particularly for materials that can withstand high temperatures, has become critical. Controlling light absorption and emission properties permits the creation of solar and thermal energy conversion systems with high efficiencies. It may also be utilized to make sensors, infrared sources and incandescent light sources with excellent efficiency. Several methods for controlling light

absorption and emission from surfaces have been studied such as metamaterials [6], nanoparticles[7,8], multilayers thin film [9], coating [10,11] and nanostructures [12,13]. The thickness of the coating, its material characteristics, and temperature may all impact the amount of radiation absorbed by the material or the amount of radiation exiting the surface, and in many processes. Moreover, surface roughness is very common and inevitable in nature, also they could be obtained as a result of manufacturing and could affect strongly on the spectral properties. Their correlation length and height of peaks are two important factors which alter the radiation absorbed or reflected. Multiple interfaces in natural systems, such as metal and graphene surfaces, sea surface temperatures, and two-dimensional turbulence, are often represented as rough surfaces [2,12,14].

Mechanical, physical, and dielectric characteristics of most materials, particularly in thin layers or films, are highly dependent on their surface topography. For example, the roughness of a biaxially oriented polypropylene film affects its breaking strength [15]. The wear rate and friction coefficient of a polymer or ceramic composite are both greatly influenced by its surface roughness [16]. Adherence to battery electrode materials is mostly determined by the roughness of aluminum foil [17]. Many optoelectronic applications, including optical imaging [18,19], chemical detection [20], target recognition [21,22], and solar energy harvesting [23] rely on spectral selectivity. Solar cells and other optoelectronic devices may benefit from spectral selectivity for heat management by reflecting undesired wavelengths that would otherwise be parasitically absorbed in the interfaces or other device layers [24,25]. Spectral selectivity by optical trapping of solar radiation is often accomplished by the modification of a surface's texture. High solar absorption in metals may be achieved by developing textured surfaces with porous, granular, or needle-like metal structures, which provide numerous reflections that efficiently capture the solar energy.

Reflecting incoming radiation, dissipating thermal energy to cool an environment, or absorbing thermal energy to heat a space are all potentially useful properties depending on the application. Conduction, convection, or radiation heat transfer may all play significant roles in a given situation, but the dominating mode of heat transfer ultimately depends on the specifics of the targeted application. Thermal radiation is basically caused by random energy level transitions in matter, implying that any object at a certain temperature may accomplish thermal energy emission [26,27]. One of the most prevalent

natural mechanisms of energy transmission is radiative heat transfer. The peculiarity of radiative cooling is its capacity to accomplish cooling without any additional energy input. Due to climate change, intense heatwaves are expected to become more common in the future decades, and this passive cooling technique may help release some of that heat to space [28]. Utilizing highly reflective metal or porous construction, radiative coolers may achieve high solar reflectivity. Currently, there are some approaches for daytime passive radiative cooling including multilayers design of radiative cooling, using surface morphology, using metamaterials, and utilizing nanoparticles. To increase the efficiency of coolers sometimes the combination of some methods and materials is utilizing. Based on the application, it is desired to select a suitable, single, cost-effective design as daytime passive radiative cooling with both high solar reflectivity and selective thermal radiation performance.

The primary goal of this thesis is engineering optical surfaces with spectral selective properties for various applications. For that purpose, rough surfaces as a kind of surface texture are going to be investigated. Although deterministic structures, e.g., patterned surfaces with certain periodicity, is widely studied for narrowband applications for transmission purposes, e.g., waveguides, due to their resonant nature, the roughness surfaces which are more common in nature and easier to fabricate are not studied in detailed in literature. Rough refractory metals with high melting point which can be used in aerospace application and their broadband spectral behaviors not studied yet. At first step, random rough surfaces are going to be studied to enhance the broadband absorption of Tungsten surface. In this study, by using the characteristics of random rough surfaces and controlling them, the use of this kind of surfaces as a spectral absorber will be investigated. Moreover, the effect of anisotropic random rough surfaces for the application of spectrally selective filters will be studied. It is known that a wide bandwidth is desired for the spectrally selective absorbers. Then we will go one step further, and we will study the effect of coating and patterns in cooling application with aesthetic consideration. For this purpose, a formulation will be developed to design passive radiative cooling with broadband optical thin-film filters. Then the thickness of layers will be optimized for minimum use of materials. Then to make it colorful for decoration purpose a plasmonic structure will be implemented to extract required narrow band absorption in visible spectrum. At the end, the underlying electromagnetic mechanisms which are responsible for enhanced spectral features of black silicon is studied. A detailed



studied to see the difference between random roughness texture and deterministic textures to highlight the absorption of black silicon is reported. Numerical simulation tools (FEM and FDTD) are going to be used to analyze the response of the developed structures. Once completed, research in this thesis and corresponding results will be a complete guideline for broadband engineering of spectral behaviors for various applications.

## **1.2. Literature Survey**

In this chapter, the relevant literature for the topics stated in the preceding section is presented. With the literature review, missing aspects in the relevant literature are summarized and potential solutions, which are the subject of this dissertation, are discussed.

### **1.2.1. Spectrally Selective Absorbers**

Thermal solar [29–31], solar thermophotovoltaic [32], nuclear fusion [33–35], and aerospace applications [36] rely heavily on materials capable of operating at high temperatures. These materials must be able to operate at temperatures exceeding 1500 °C [37]. Tungsten (W) is increasingly being used for different applications, such as solar devices, due to its outstanding chemical and thermal stability, high melting point, wear-resistance and the ability to store energy for over long periods of time [38–40]. Moreover, Tungsten is one of the refractory metals with intrinsic absorption in the VIS to NIR region that operates at high temperatures for the applications in which a high absorption is needed. Tungsten has high absorption in the visible range, but its large real part of the dielectric constant leads to a high reflection in the infrared regime. This causes flat films to have 60% or less absorption [41]. Tungsten can be textured in the shape of a pyramid micro/nanostructures to boost absorption [42]. Detailed modal analysis predicted periodic Tungsten absorbs light in a wide angular range; however, oxidation effects result in low stability of textured Tungsten at high temperatures [42].

Several strategies for manipulating surfaces' optical properties, including absorption and emission of light, have been established in the literature, including photonic crystals [43,44], optical metamaterials [45,46], nanoparticles [1,47], multilayer thin films [48], and micro/nanotextured structures [49]. Since the 1970s, the principle of using surface structures and surface patterns has been used as an alternative to thin-film coatings for controlling spectral reflection and absorption. Anti-reflective treatments are used extensively in the optic industry for applications ranging from lenses, lasers, cameras, solar cells, and visible and near-infrared light systems to windows, missile domes, defense, and infrared laser systems [50,51]. In military, aerospace, and some industrial applications, which primarily utilizes infrared (IR) spectrum, reflection is a major issue. A common approach to improve optical reflection is to use several thin layers of dielectric materials that are mounted on the exterior surface of the window or optical component [52]. Enhancing photon absorption by increasing the active layer thickness is a relatively simple method, but the balance between charge and absorption also limits the thickness of the layer. One of many techniques for enhancing absorption without raising the actual layer thickness is to pursue a light attenuating structure, allowing the number of internal passes inside the functioning layer to improve the total length of the optical path [53]. At higher frequencies, the surface texture has a significant impact on the material's interaction with the electromagnetic wave [54]. Textured or porous layers can scatter light, and hence, intensify the duration of light travel through the absorber. Recently, significant progress was made in modeling and manufacturing nanostructures to handle surface optical absorption and emission properties [1,55].

In the case of high optical power, the optical properties of material are no longer linearly related to the intensity of the incident light. One effect is nonlinear absorption, which may cause heating. This nonlinearity changes the propagation of intense light through the medium [56]. Incident light energy may be efficiently concentrated in resonant nanostructures, and this causes the temperature of nanostructure increase [57]. The activation of surface plasmon resonance results in this phenomenon, which manifests a sufficient increase in optical absorption. Light is absorbed almost entirely by free electron transitions inside the conduction band in metals [58,59]. On the optical side, heating changes a nanostructure's optical response, which is dependent on the nanostructure's and environment's dielectric characteristics [60]. Optical heating can be used in various application including water heating [61], biomedical application [62],

surface coloring [63] and many other fields. On the other hand, this increase in the temperature of surface could affect the act of surface as a sensor which should be taken into consideration in sensitive applications. In the literature, the temperature dependency of the thermal expansion coefficient of water, as well as thermal boundary conductance at the interface, are taken into account [64]. Moreover, it is shown that by changing the temperature of the nano resonator, the emitted signal can be modulated [65].

Selective absorbers are commonly used in various fields due to their high absorptivity at specific wavelengths [66]. Spectrally selective filters can be used in various of applications involving solar absorbers [67], sensors [68], passive cooling [48,69], and thermophotovoltaic devices [70]. Optimization of energy use could be achieved by using the control of solar spectra. In addition to the consideration of cost, having the right transition wavelength can increase the efficiency of a solar absorber for specific applications significantly. Solar selective coatings are more common spectral selective absorbers studied in the literature [71]. Nanostructures can act as spectrally selective absorbers on the substrates [72]. While several studies exist in the literature regarding nanostructures' effect on the absorption spectra, the ability of random textures to use as spectrally selective absorbers has not been studied yet. The non-periodic structures can achieve high absorption rates, with structural sizes of one micron [73].

### **1.2.2. Colored radiative cooling**

Passive radiative cooling, an innovative approach for cooling of buildings, electronic equipment, and other devices is based on the variations of spectral properties of paints and coatings. Its main idea is to design coating to have spectral properties that allows an object to radiate more to the atmosphere at the atmospheric transmission window (8-13  $\mu\text{m}$ ), while minimizing the absorption at the visible (peak-solar) spectrum (0.4-1.0  $\mu\text{m}$ ). The importance of radiative cooling and other passive techniques will be more important because of increasing emphasis due to the need for energy efficiency and cooling techniques with minimum electricity use [74–76]. Radiative cooling has been successfully considered in a variety of applications, including buildings [77], temperature-sensitive electronic and optoelectronic devices, such as photovoltaics [78–

80], power electronics [81], infrared detectors [82], and thermophotovoltaics [83,84]. Using the spectral selectivity of materials, the thermal load of exterior surfaces can be controlled for efficient thermal management of devices. Its use for buildings is particularly important as building use almost one-third of the energy globally, and in many regions almost one third of that energy is used for cooling, due to the incident solar energy on them. If solar energy absorption by the building surfaces is minimized, and if the surfaces emit more energy at longer wavelengths, naturally the heating load and the requirement for the HVAC systems would decrease.

Generally, white color is preferred to minimize the solar energy absorption. However, without considering the full spectrum, this assumption cannot be made. Not all white paints and coatings are the same; a detailed discussion of them are recently provided by Ruan et. al, [85] who showed that their ‘white’ is whiter than the other similar paints. In some colder locations, on the other hand, the dark colors are popular to enhance the surface absorption and hence heating of buildings. In this case a smooth, low-emissivity, metal base covered by a thin surface layer which is visibly dark but substantially transparent in the infrared can be used [86].

To achieve passive radiative cooling, a variety of materials and designs have been employed for thermal management of buildings [77] and structures [87]. Besides the effect of material properties on spectral selectivity, the other principle of passive radiative cooling relies on adjusting the spectrum emittance from a surface, which requires surface structural alterations. Spectral emission divergence was controlled by designing and implementing a selective structure to reduce solar input. Research shows that surface spectral characteristics may be manipulated using thin-film layers or nanostructures [2,12,48,88,89].

To achieve high levels of radiative cooling, the visible portion of the incident light must be reflected to provide the best cooling performance, by using spectrally selective emitters, as discussed in [48,90]. However, usually the color of such surfaces is not considered. For decorative, aesthetic and architectural acceptance of the new types of paints, the spectral variations in visible range which gives rise to color sensation must be taken into consideration [91]. Typically, an object's color in sunlight is determined by its selective absorption within the solar spectrum. Colorization of the surfaces reduces the

cooling efficiency due to solar absorption in the visible range; hence, selective narrowband absorption in the visible area is needed to minimize radiative cooling power loss. As a result, it is desirable to achieve passive daytime radiative coatings with high cooling rates from energy efficiency and simultaneously have the ability to achieve vibrant and decorative colors [92].

To achieve a desired color while maintaining high levels of radiative cooling power, visible narrowband absorption is necessary. In the literature, various methods exist to achieve narrowband spectral features. Among these methods, resonant phenomena, such as Fabry-Pérot resonances [93], Tamm plasmons [91], or localized surface plasmon resonances [94] were used to achieve narrowband spectral features. Structural colors, for instance, are created by microscopic structures that are small enough to interfere with visible light. Blandre et al. [87] demonstrated a basic structure for sky radiative cooling applications using electromagnetic simulations. The structure consists of a surface-textured silica layer placed on a silver substrate. They show that this sort of structure is efficient because it allows for the excitation of surface phonon-polaritons to achieve near-perfect emissivity. Metal-insulator-metal (MIM) nano resonators, which consist of an insulator sandwiched between two metallic materials, may also function as color filters [95]. By adding the MIM component into the thermal emission structure, Lee et al. [93] designed a radiative cooling device with subtractive primary colors. According to their results, the steady-state temperature was found to be 3.9 °C colder than that of the ambient. Sheng et al. [91] introduced a radiative cooling device aided by the optical Tamm resonance, which achieves the radiative cooling function as well as the subtractive primary colors. A MIM and grating combination may also effectively divide white light into a specific wavelength with a different color. The MIM-grating color filter is made up of Al-ZnSe-Al resonators. Diffraction at the bottom Al grating layer facilitates the coupling of the incoming light to plasmon waveguide modes, while scattering at the top Al grating layer reconverts the detained plasmon to a propagating wave. This MIM grating design provides a number of benefits, including compactness, high transmission efficiency, and a narrow bandwidth [96].

It is known that photonic and plasmonic selective emitters can be effectively controlled to radiate heat through a sky into space and provide passive cooling for objects [97]. Several photonic structures, including multilayer planar photonic thin films [98], 2D

and 3D photonic devices [99], metamaterials [100], and plasmonic structures [101], have been suggested and tested to maximize emissivity in the atmospheric window while maintaining high reflectivity in the solar spectrum. Plasmonic nanostructures can act as a structural color filter since it has nano-scale features that interacts with incident light to reflect or absorb light at a specific wavelength. Nano-antennas with a bow-tie configuration is a kind of plasmonic structure that is commonly employed in optical applications to generate high electric fields inside a restricted volume. The coupling of localized surface plasmon resonances (LSPRs) in the antenna gap localizes and confines optical radiation, resulting in high electric field enhancement [102]. In the literature, it is shown that bow-tie nanoantenna could enhance the electric field around the surface, and using the parameter of antenna, the absorption peak can be controlled [103,104].

### **1.2.3. Broadband Absorption in deterministic and rough surfaces**

Silicon devices with high absorptivity is heavily utilized in various applications of photonics including photodiodes [105–108], photodetectors [109–111] and solar cells [112–116]. Demand for high absorptivity attracts the attention of the researchers, and therefore lead to various type of silicon based photonic structures with high absorptivity, which are also known as black silicon [117][118]. In the literature, black silicon is achieved by introducing geometrical textures on the surface of silicon. Although high absorptivity over a broad spectral band is reported with surfaces with various textures, the underlying physical mechanisms that lead to high broadband absorptivity, is still an area that requires further research.

Black silicon has attracted attention of the researchers when it was fabricated by reactive ion etching (RIE) in which microstructures with high depth to width ratios were observed [118]. Later, black silicon with high absorptance in the 0.5 -2.5  $\mu\text{m}$  spectrum band is demonstrated [117] by fabricating the surface textures using laser chemical etching. Enhanced absorption is attributed to the increased light trapping effect due to the spikes with high depth to width ratio. While abundant several studies exist in the literature

regarding the experiments and fabrication techniques for micro-structured black silicon [119,120], fundamental physical mechanisms that yields this behavior have not been equally investigated. Scattering characteristics of electromagnetic waves from such random rough surfaces for various applications have been studied in the literature.

These studies include communication over rough ocean surfaces [121,122], remote sensing applications involving terrestrial applications and buried objects [123,124], surface texturing in solar cells [125,126], and surface plasmon excitation with rough surfaces [127–130]. Despite this established literature on rough surface scattering from surfaces, surface roughness effects leading to broadband absorption in black silicon have been largely ignored [131,132]. In [131], response of the random texture is analyzed by calculating the field distribution of periodically arranged surface texture. Strong correlation between the absorptivity of the random and periodic textures are observed and enhanced absorptivity is attributed to increased field intensity in the geometry. However, underlying mechanisms responsible from high field intensity are not explored.

There is also abundant literature for surfaces with deterministic textures for absorption/emission enhancement. In recent years, with the advancements in nanotechnology, periodically arranged surface textures are heavily utilized in the field of photonics due to the capability of resonance excitement. Frequency selective structures composed of silicon is reported for mid-infrared applications [133][134]. Issue with these structures suffer from low bandwidth of absorption due to resonant based nature. To overcome low bandwidth issue, different structures that combines multi-resonances together are studied in the literature [135][136]. However, those structures suffer from reduced absorption efficiency due to the destructive interference of different resonance modes. Besides the mid-infrared applications, periodically arranged surface textures are also developed for applications in visible and near-infrared spectrums [137][138]. In [137], structures are capable of strongly trapping the light in silicon for solar cell applications. Another study [138] proposed a hybrid structure, which sandwiches silicon structure between a polymer and a textured gold layer. Hybrid structure traps the light inside the silicon very effectively, thus resulting in high absorption in 0.3 -2  $\mu\text{m}$  interval reaching up to 90 % levels. However due to the hybrid nature, such structure requires several fabrication steps which makes it less feasible for fabrication. Black silicon devices composed of periodically arranged textures, for which some of the examples are given

above, owe the absorptance enhancement to the field enhancement inside the silicon. High field enhancements in these devices are either attributed to resonance or light trapping effects due to sandwiched silicon. However, physics of the field enhancement in pure silicon structure, which neither support plasmonic resonances nor benefit from multiple reflections, is not clarified. Absorptance spectra of pyramid like textures composed of pure silicon is approximated by a multilayer structure with effective medium theory in [139]. Although computational results well agree with the experimental results, such approach does not able to explain the underlying physics. It shows that absorptance spectra of periodic surface textures can be mimicked with a multilayer structure which benefits from destructive interference of the reflected beams on the front surface.

It is important to uncover the mechanisms of the enhanced broadband absorption in micro-structured silicon with random and deterministic textures, especially at wavelengths above its bandgap. To address this, texture geometry and doping concentration as major influential parameters on the absorptivity of the black silicon and linked those parameters to electromagnetic phenomena, which induce high field intensities is compared with a random texture. Random texture geometries are analyzed by expressing them by random Gaussian surfaces and spectral characteristics are obtained. Surface geometry is characterized by root-mean-square (RMS) of surface height,  $h_{rms}$  and transverse correlation length  $l_c$ . Electromagnetic responses of those structures are analyzed by finite difference time domain (FDTD) [140] simulations. Then, spectral characteristics of random textures are compared to periodicity controlled deterministic patterns, and the field distributions are calculated for analysis with FDTD [140]. The findings show that overall field enhancement in the pure-silicon structure stem from these two different phenomena depending on the width of the features of the textures. These findings reveal the underlying physics of the broadband absorptivity enhancement in black silicon, which can aid the future studies in the field.



### 1.3. Aims & Objectives

The primary goal of this thesis is the engineering surfaces via altering surface features, multilayer coatings, or plasmonic nanostructures to control the spectral characteristic of the surface. The underlying mechanism and proposed designs combined with material properties and different coatings is studied in this thesis. The following applications and contributions to the connected area are presented and shortly summarized:

- Tungsten based spectrally selective absorber: Improving the spectral selectivity of the absorber is of interest nowadays. The emissivity of solar absorbers is particularly important for use at high temperatures. Significant work has been done recently to take advantage of solar-selective absorber coatings that maintain their effectiveness even at very high temperatures. Various method such as coatings, using plasmonic structures, metamaterials and nanoparticles is utilized in literature to enhance the spectral selectivity. Although promising results has obtained with those methods, but all these methods add cost to the system. In this thesis, rough surface features with varying feature profiles and depth is used to obtain high absorption in Tungsten. Here, we use this concept for Tungsten surfaces, a stable thermomechanical material, to increase the length of the optical path in a thin absorber layer significantly. Our approach goes one more step to demonstrate broadband spectrally selective absorber using Tungsten anisotropic rough surfaces. As opposed to previous methods, which designed spectrally selective absorbers by adding extra materials, we propose to have same effect only with roughening the surface and control over spectral characteristics by controlling roughness parameters.
- Colored passive radiative cooling: Radiative cooling is a passive technique that depend on radiative heat transfer to cool the surface. For passive radiative cooling the goal is to provide a surface that rejects incident radiation while maximizing surface emission. Recently, the concept of radiative cooling has been applied to reduce building energy costs via surface coatings. The most important factor in designing a passive radiative cooling using coating the layers is optimizing the thickness of layers

to obtain maximum cooling power with minimum material. However, lots of effort have been done in the literature for designing radiative cooling with maximum cooling power but its aesthetic aspect has not been considered and most of the designed device show white in color. This aspect becomes important specially when it comes to wearable applications, cloth, or outer surface of buildings. Recently some methods proposed to add coloration to radiative cooling however most of them done by adding extra layers and the control over coloration is by changing the thickness of the layer or using metamaterials. Here in this thesis, we proposed a new plasmonic structure which can be added to layered radiative cooling to obtain colors. The control over colors is simply done by changing the parameter of this structure.

- **Broadband Absorption in deterministic and rough surfaces (Black Silicon):** Black silicon is a superior antireflective and light-trapping material that has the potential to exceed commercially from available optically textured surfaces. It has been shown that the black silicon surfaces regularly outperform their micron-scale pyramid counterparts, both in terms of decreased broadband surface reflectance and scattering of incoming photons at larger polar angles. In literature the different fabrication methods for producing black silicon is introduced also it is used in various applications as an absorber such as solar cell. However, the underlying processes responsible for such behavior are not described. Therefore, in this thesis, rather than proposing a method for making black silicon, more focuses is on analyzing underlying mechanics which are responsible for enhanced spectral features.

#### **1.4. Contributions**

The research presented in this dissertation makes contributions to the controlling optical properties specially absorption, reflection and transmission. Particularly, it proposed novel design techniques for the field of spectrally selective surfaces, optical coatings for energy harvesting and thermal control while preserving decoration and provided explanations for the resulting behaviors. Following is a brief overview of the

suggested solutions to various challenges and their respective contributions to the relevant field:

- Tungsten based spectrally selective absorber: A design methodology using anisotropic random rough surface is implemented to control spectral selectivity. Scattering at rough interfaces between the absorber layers causes a change in the electromagnetic field angle of incidence within the absorber layers. This leads to a phenomenon known as internal coupling, which allows light to couple inside the absorber [141]. Using this concept, randomly textured surface substrates have been successfully used for the integration into solar cells of rough interfaces. In this case, the formation of anisotropic surface can be achieved by stretching an isotropic surface in certain directions, resulting in different lateral correlation lengths. It represents random rough surface interface with varying correlation length in the x and y directions. In this study, we propose a technique to engineer the surface morphology based on anisotropic surface roughness for improving the surface optical characteristics. Isotropic and anisotropic random rough surfaces of Tungsten with various RMS height and correlation length are investigated. The random rough surface in this study is characterized by Gaussian power spectral density (PSD) with RMS height and correlation length. Surface properties of textured tungsten surface are modeled using the finite-difference time-domain (FDTD) technique, which enables analysis of textured Tungsten surface absorbance. Using this method, a high absorption over a broad spectral band is obtained without adding any extra layers or coatings.
- Colored passive radiative cooling: Extensive research on passive radiative cooling as a method to cool the outside of buildings and cut down on cooling costs for interior spaces has been conducted. There are lots of proposed models in literature to tried achieving high cooling power but most of them looks white in color which is not desirable when the coloration is important. Here the coloration of passive radiative cooling using plasmonic nanoantenna to have benefits of having coloration in aesthetic applications as well as radiative cooling function is studied. In this thesis, we begin by outlining an approach to design a daytime passive radiative cooling structure with optimized thin-film layers with the aim of cooling power maximization. Then, to add color to the system, a plasmonic nanostructure is proposed and analyzed,

which is defined as a silver plasmonic bowtie nanoantenna that is placed between reflector and emitter layers to have both high cooling power and coloration together in our structure. The finite-difference time-domain (FDTD) approach is used in order to carry out numerical investigations into the optical characteristics of the plasmonic nanoantenna. These features include the absorption spectra, gap enhancement, and electric field distribution. The effects of the nanoantenna parameters on the resonance wavelengths of the proposed structure to examine the display color of radiative cooling is also studied. As a result, the present research introduces a novel idea for daytime radiative cooling systems that include equivalent attention to technical design but with the purpose of developing systems that deliver aesthetically appealing colors.

- **Broadband Absorption in deterministic and rough surfaces (Black Silicon):** According to the literature, black silicon is obtained by adding geometrical textures on the surface of silicon. Although strong absorptivity across a wide spectral range has been reported for surfaces with varying textures, the underlying physical processes that contribute to high broadband absorptivity are yet unknown. In this study, black silicon is created by increasing surface roughness, either randomly or deterministically. According to the findings, two distinct electromagnetic processes occur in the textures, resulting in higher field intensity and, as a result, enhanced absorption. Provided results, elaborated on the underlying principles, and gave light on the origins of the broadband absorption in black silicon.

Several scientific publications have already been published as a result of the research presented in this dissertation, and more are in the process of being written. The following are the published works:

- Pirouzfam, Niloufar, and Kursat Sendur. "Tungsten Based Spectrally Selective Absorbers with Anisotropic Rough Surface Texture." *Nanomaterials* 11, no. 8 (2021): 2018.[2]
- Kecebas, Muhammed Ali, Niloufar Pirouzfam, and Kursat Sendur. "Origins of the enhanced broadband absorption in black silicon." *Journal of Applied Physics* 129, no. 16 (2021): 163103.[12]

The following manuscript in preparation for submission to a scientific journal:

- Pirouzfam, Niloufar et al. "Colorization of Passive Radiative Cooling Coatings using Plasmonic Effects," *in preparation*.

## 1.5. Thesis Outline

In addition to this chapter, this thesis consists of four chapters, in each chapter corresponding methodologies, associated results, and discussions for the relevant field and concluding remarks are presented.

In chapter 2, a spectrally selective absorber made of Tungsten material is proposed. A new design using anisotropic random rough surfaces is introduced to control the absorptivity spectrum. Using finite difference time domain, the surface is optimized to have broad absorptivity.

In chapter 3, a colored radiative cooling is designed using plasmonic nanoantenna as a coloration module. The thickness of coated layers is optimized using genetic algorithms to have maximum cooling power while be suitable for coloration purpose. The effect of geometrical parameters of plasmonic structure to control the generated colors are also studied in this chapter.

Chapter 4 investigates the origins of broadband high absorption in black silicon. The absorption spectra and field distribution over random texture and deterministic texture are analyzed and compared to find the underlying physics of the broadband absorptivity enhancement in black silicon. Spectral characteristics of random textures are compared to periodicity controlled deterministic patterns, and the field distributions are calculated for analysis. By using effective wavelength matching and waveguide modes, the occurrence conditions of local high field enhancements and phenomena that interfere with local enhancements are evaluated.

Chapter 5 presents the concluding remarks and the future work.

## **2. TUNGSTEN BASED SPECTRALLY SELECTIVE ABSORBERS WITH ANISOTROPIC ROUGH SURFACE TEXTURE**

In this study, a random distribution of surface features with varying feature profiles and depth is used to obtain high absorption in Tungsten. Scattering at rough interfaces between the absorber layers causes a change in the electromagnetic field angle of incidence within the absorber layers. This leads to a phenomenon known as internal coupling, which allows light to couple inside the absorber [141]. Using this concept, randomly textured surface substrates have been successfully used for the integration into solar cells of rough interfaces [141]. Here, we use this concept for Tungsten surfaces, a stable thermomechanical material, to increase the length of the optical path in a thin absorber layer significantly. Our approach goes one more step to demonstrate broadband spectrally selective absorber using Tungsten anisotropic rough surfaces. In this case, the formation of anisotropic surface can be achieved by stretching an isotropic surface in certain directions, resulting in different lateral correlation lengths. It represents random rough surface interface with varying correlation length in the x and y directions. We propose a technique to engineer the surface morphology based on anisotropic surface roughness for improving the surface optical characteristics. Isotropic and anisotropic random rough surfaces of Tungsten with various RMS height and correlation length are investigated. The random rough surface in this study is characterized by Gaussian power spectral density (PSD) with RMS height and correlation length. Surface properties of textured tungsten surface are modeled using the finite-difference time-domain (FDTD) technique, which enables analysis of textured Tungsten surface absorbance. Using this method, a high absorption over a broad spectral band is obtained without adding any extra layers or coatings.

## 2.1. Materials and Methods

In this section, first, we describe the methodology to form a randomly rough surface made of Tungsten. After that, a numerical approach is applied to obtain the optical properties and spectral absorption of random rough surfaces in the wavelength range of 300-3000 nm. The procedure for obtaining optical properties from random rough surfaces is summarized. In the next step, the anisotropic random rough surface of Tungsten is examined, and the effect of this random texture on the optical properties of surface and Absorbance bandwidth is reported. The data in this manuscript are obtained theoretically using rough surface interfaces described with Gaussian power spectral densities and by using a Gaussian random number generator [142]. The size of 3D grids is  $10 \times 10 \times 10 \text{ nm}^3$  in our models and the uncertainty was set to  $1e-05$ . Rough surfaces with Gaussian power spectral densities are common when representing a variety of interfaces in natural systems including rough metal surfaces, rough graphene surfaces, sea surface temperatures, and 2D turbulence [14].

The schematic of the proposed system is shown in Fig. 2.1. As shown in Fig. 2.1, the isotropic and anisotropic random rough surface could increase the absorption in the VIS and NIR regions. Solar irradiance spectrum covers a wide range of wavelengths as can be seen in Fig. 2.1 (a). The curve (that starts at about 300 nm) shows the incident solar power per square meter at each wavelength just above the Earth's atmosphere. The solar spectrum is separated into three different parts including UV, visible, and infrared which is shown by a solid line in Fig. 2.1 (a). Moreover, in panel (b) of Fig. 2.1 the effect of roughness over a flat surface and the comparison of isotropic and anisotropic random rough surfaces is shown. As we will discuss later in the manuscript, the absorption spectrum increases when the surface is rough. In addition, modifying the surface anisotropy impacts the absorption especially in the visible and near infrared regions. A schematic of isotropic and anisotropic random rough surfaces and their working principle in the scattering of light is displayed in Fig 2.1 (c) and Fig. 2.1(d). It is observed that all the UV and VIS light and some parts of infrared light are absorbed using anisotropic rough surfaces. Moreover, the top view of both isotropic and anisotropic random rough texture can be seen in Fig. 2.1 (e) and Fig. 2.1(f).

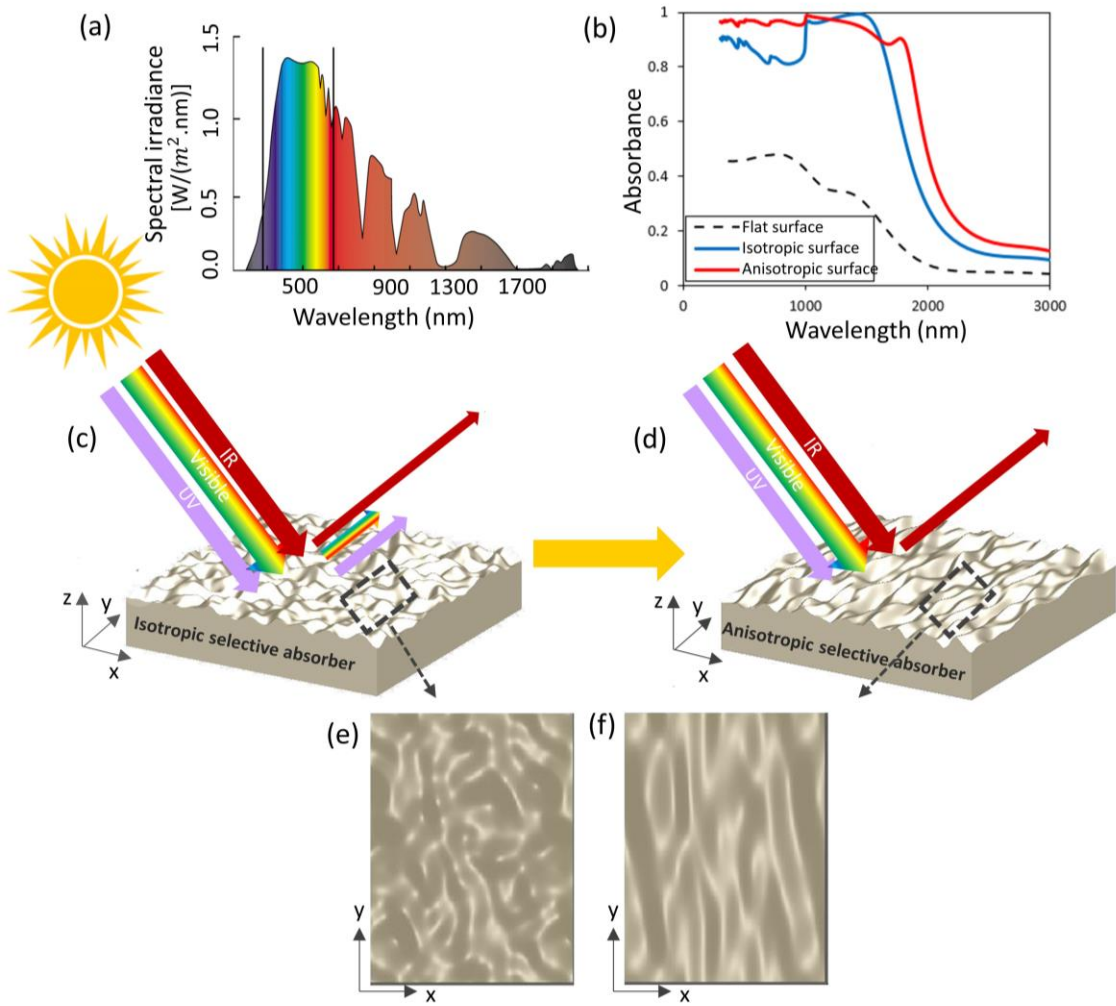


Figure 2. 1: Schematic of proposed selective absorber (a) Solar radiation spectrum (b) Comparison of absorption spectrum for flat surface and rough surface (c) Scattering from isotropic random rough surface (d) Scattering from anisotropic random rough surfaces (e) Top view of isotropic rough surface (f) Top view of anisotropic rough surface

Rough surfaces exhibit less reflectance and better absorption than flat surfaces [143,144]. In reality, different types of surface defects and roughness can manifest while using mechanical machining or material synthesizing processes, which results in different PSD spectra. Surface roughness is one of the important factors affecting the reflectivity/emissivity due to the incident angle change on different facets [145]. In the current study, random texture geometries are characterized by their statistical properties, height distribution and correlation length. The height distribution specified as sigma RMS, determines the variation of heights from a smooth planar and represent the standard deviation of the distribution of surface heights. Correlation length ( $L_c$ ) defines a short



distance between two points for which the heights of a rough surface are correlated with each other.

Surface roughness is quantified using PSD functions as the spread of height deviations from a mean plane and the lateral distribution/distance over which the height variation occurs. The Gaussian surface described using the Gaussian PSD function is one of the simple approximations of random surface roughness. The three-dimensional Gaussian randomness being achieved from specifying a given spectral density referring to [146]:

$$W = \left( \frac{l_x l_y h^2}{4\pi} \right) \exp \left[ - \left( \frac{K_x l_x}{2} \right)^2 - \left( \frac{K_y l_y}{2} \right)^2 \right] \quad (2.1)$$

where  $h$  is the root mean square (RMS),  $l_x$  and  $l_y$  are the correlation length along the x and y directions, respectively and  $K = \sqrt{(k_x)^2 + (k_y)^2}$  is the wavevector in the radial direction. Moreover,  $K_x = 2\pi x/l_x$  and  $K_y = 2\pi y/l_y$ . The autocorrelation function corresponding to Eq. (2.1) is,

$$\rho(x, y) = h^2 \exp \left[ - \left( \frac{x}{l_x} \right)^2 - \left( \frac{y}{l_y} \right)^2 \right] \quad (2.2)$$

To get a better understanding of the light absorption characteristics of W refractory metal, the finite difference time domain (FDTD) simulations were carried out to obtain the full-wave solution of Maxwell's equations. The FDTD [147] approach is one of the most appealing techniques for studying light absorption from randomly formed small particles in computational electromagnetics. It produces a frequency-domain electric-field and magnetic-field distributions for all frequencies of interest. The geometry of random rough surface is inserted to the commercial simulation software (Lumerical) as a developed script based on Gaussian distribution which is mentioned above. Our simulation is set in 3-D, and the upper and bottom surfaces in the z-direction are subjected to the perfectly matched layer (PML) boundary condition, and the periodic boundary condition is applied on the side surfaces in the FDTD simulation region. A broad frequency plane wave is incident from the top of the surface with the linear polarization along the x-axis. The transmittance and reflectance monitor are set on the bottom and top sides of the surface, respectively, to collect the propagated light. The light absorption

spectrum is then visualized at different absorption resonance wavelengths. Also, the magnetic (H) and electric (E) components of the incident electromagnetic radiation are parallel to the surface, while the wavevector  $k$  (direction of oscillation) is perpendicular to the structure. The permittivity of Tungsten is taken from Palik's book [148] and the real and imaginary part of permittivity is illustrated in Fig. 2.2. Under these conditions, the light reflection, transmission, absorption properties of random rough surfaces are evaluated. The thickness of the samples is 1000 nm. For this thickness, Tungsten's transmission in the entire spectral range is nearly zero, indicating an almost total absence of transmission. The power flow across a surface on an averaged time basis is defined by [149]:

$$P = \int S ds = \int \frac{1}{2} \text{Re}[E \times H^*] ds \quad (2.3)$$

in above formula  $S$  is Poynting vector which is cross product of  $E$  and  $H$  vector.  $E$  and  $H$  are the electric and magnetic field intensities, respectively. Here,  $H^*$  denotes the magnetic field vector's complex conjugate, and  $s$  denotes the surface area. The reflectivity is given as:

$$R = \frac{P_r}{P_i} \quad (2.4)$$

where  $P_r$  represents the reflected light's power and  $P_i$  represents the incident light's power. Then to calculate the absorption coefficient of a solar absorber below formulated is used: [150]

$$A(\omega) = 1 - T(\omega) - R(\omega) \quad (2.5)$$

where  $T(\omega)$  and  $R(\omega)$  are the frequency-dependent transmission and reflection parameters, respectively. Maximum absorption is obtained when the reflection and transmission coefficients are minimized. Since the optical properties of the material can be affected by both the intrinsic properties and the surface morphology, the study of surface engineering could be an excellent approach to change the optical properties.

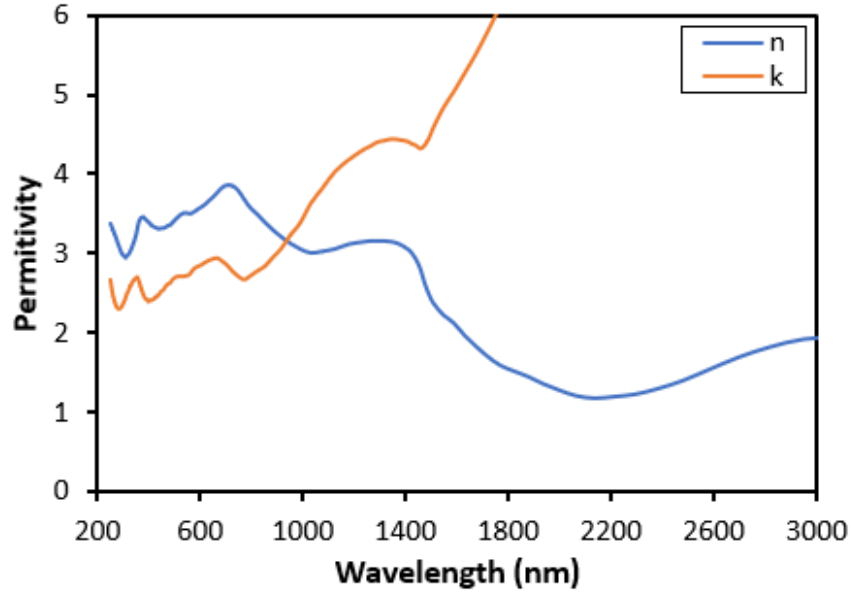


Figure 2. 2: The real and imaginary part of the permittivity of the Tungsten

Numerous studies have been conducted on the control of absorption using surface microstructures such as shallow grating [151–153]. One advantage of optical control via surface gratings is the high thermal stability of optical devices, which are typically fabricated on bulk materials and thus do not contain thermal discontinuities, in contrast to multiple antireflection or filtering coatings. This indicates that spectral control via surface gratings is an appealing prospect for high-temperature applications.

Inspired by the grating coupler, anisotropic random rough surfaces are taken into consideration in the next part. Anisotropic surfaces increase the absorption by acting as a more effective light trapping structures and they can act as effective passive spectrally selective absorbers. The anisotropic rough surfaces can be generated when a randomly rough surface has two different correlation lengths along  $x$ ,  $y$ , marked as  $l_x$ ,  $l_y$  respectively, and the reflection and absorption of the surface is affected. Tungsten is chosen as the refractory metal which can use in high temperature and in compared to noble metals such as Ag and Au, has high thermal stability.

The proposed technique has advantages over additional top layers. Using the proposed method as a spectrally selective device reduces the cost as no extra material are needed over the rough tungsten surface. Spectral filters with additional top layers also involve additional steps for patterning. In the proposed technique, there is no need to use any special mask for producing pattern in the lithography step to act as spectral selective

filters. Additional manufacturing steps can be eliminated, which involves patterns on top of a surface as these steps need a clean room environment and different stages including deposition, lithography and etching. On the other hand, manufacturing a random rough surface can be obtain using different methods such as powder metallurgy, direct laser deposition [154], chemical methods [155] and mechanical machining, most of which are direct methods without the need for a cleanroom environment. In addition, there are some new techniques to produce a nano-size surface roughness to be used in optical devices such as single-point diamond turning technology [156]. The top view of various correlation lengths for an anisotropic random rough surface can be seen in Fig. 2.3. The dark grey color in the figure shows the higher heights (peaks) and the light grey shows the lower heights.

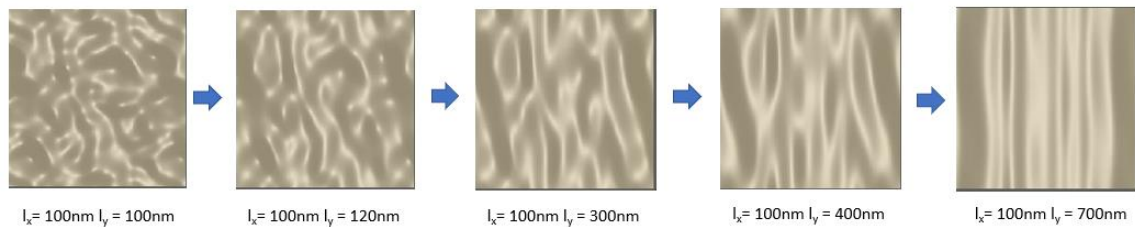


Figure 2. 3: Anisotropic random roughness texture formed by random Gaussians

## 2.2. Results and Discussion

We first studied the effect of surface roughness on Tungsten surfaces. To analyze the influence of surface morphology on spectral absorption of Tungsten surfaces in the VIS and NIR spectral regions, the absorption spectra of the flat and roughened Tungsten surface are compared in Figure 2. 4. In this case, the rough surface is isotropic with correlation lengths  $l_x=100$  nm,  $l_y=100$  nm, and RMS surface height  $h=50$  nm. As shown in Fig. 2.4, the spectral absorption of Tungsten increases significantly for a rough surface compared to a flat Tungsten surface, especially for wavelength below 1500 nm. This phenomenon comes from the wave interactions and the corresponding effects on absorption. It is worth noting that in the spectral region of interest, 0.4-1.5  $\mu\text{m}$ , Tungsten does not support surface plasmons. Tungsten has shown a nonzero value of 2.5–4 for the

real and imaginary parts of its permittivity. Within this spectral range,  $n$  decreased gradually while  $k$  increased monotonically as previously shown in Fig. 2.2. Please note that, the absorption reduces in the longer wavelengths, and there is not a notable difference between flat and rough surfaces. Our results indicate a strong relationship between the absorption spectra of rough Tungsten surfaces and the correlation length and RMS height of the rough surface.

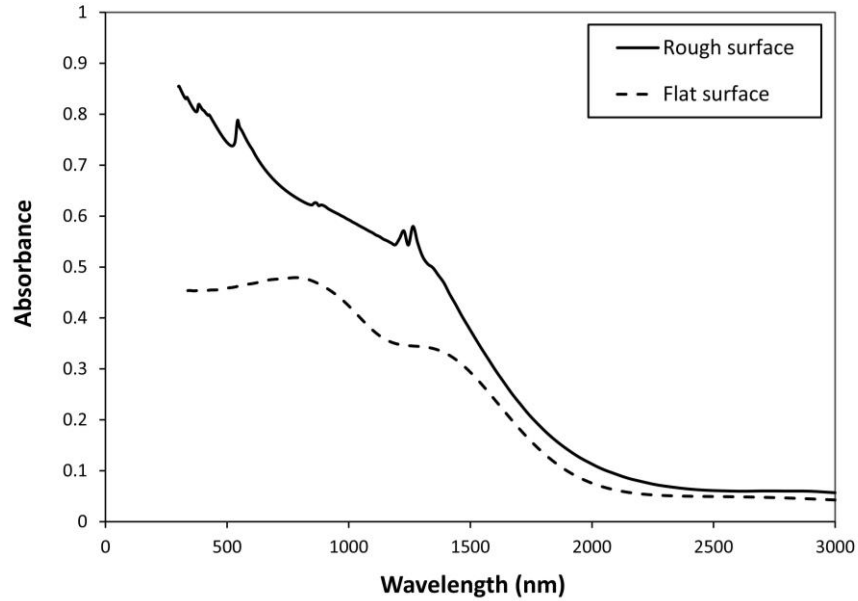


Figure 2. 4: Comparing Absorbance of Flat and rough ( $l_x=100$  nm,  $l_y=100$  nm and  $h=50$  nm) Tungsten finite thickness film by FDTD solution

In Fig. 2.5(a), the absorption spectra of various surfaces with different correlation lengths at a fixed RMS height of  $h=50$  nm are given. As shown in Fig. 2.5(a), increasing the roughness by reducing the correlation length, which increases the slope of the surface facets at a fixed RMS height, enhances the absorption of Tungsten. A similar effect can be observed in Fig. 2.5(b), where the absorption spectra is given for various heights at a fixed correlation length of  $l=100$  nm. Both Fig. 2.5(a) and Fig. 2.5(b) shows no significant difference between textures with varying  $l$  and  $h$  at longer wavelengths such as with decreasing the correlation length in the isotropic case. The absorption increases in the VIS region, as shown in Fig. 2.5(a). As we increase the correlation length to values larger than 200 nm, a peak in the absorption spectra is observed. It is noted that when the correlation length becomes larger than  $\lambda/5$ , a peak resonance is observed in the absorption

spectra. This effect intensifies by increasing the RMS height of rough texture, and the peak point in the absorption spectra reaches unity. When optical coupling happens, absorption peaks occur. The physical mechanism that increases the interaction of electrons in the media with polarized light can be explained as more efficient light trapping through curved surfaces and an increased optical path during the scattering processes. The correlation length in the optimal structures provides the effective slopes for light trapping and increases the optical path. Based on the optimized values obtained in Figs. 2.5(a) and 2.5(b), a correlation length of 200 nm and a minimum height of 100 nm is selected to have an absorption peak in a specified wavelength region. Our results indicate that the spectral reflection from the samples is sensitive to the height, the correlation length, and the anisotropy of the tungsten surfaces. The features in the spectral reflection distributions thus can be an interesting future perspective to retrieve information about the height, the correlation length and the anisotropy of the samples. The cluster analysis techniques are particularly promising to retrieve these geometric parameters, as it was applied recently to discriminate the dimensions of metal nano disks [157].

The spectral distribution of the absorption of Tungsten surfaces can be influenced by the surface roughness by selectively changing the correlation length and RMS height of the random rough surface as shown in Fig. 2.6. In particular, the bandwidth of the spectral distribution can be greatly enhanced. This phenomenon can be used in the spectral selective absorbers, in which high absorption is needed at a specific wavelength. Based on the results in Fig. 2.6, a surface with a correlation length of 200 nm and a RMS height of more than 100 nm shows nearly 100% absorption at the wavelength in range of 1000-1500 nm. A relatively narrowband absorption is observed for systems with a lower RMS height. Additionally, the VIS region has a lower spectral absorption. These characteristics are primarily due to the decreased optical coupling efficiency and narrow bandwidth of the resonances supported by the small surface peaks. Increasing the height of rough texture increases not only the absorptions in the VIS region but also the broad bandwidth of absorption. Furthermore, the near-unity absorption is accessible over a larger bandwidth. The underlying reason for this trend is that the rough surface height increases the degree of interaction between resonance and trapping light.

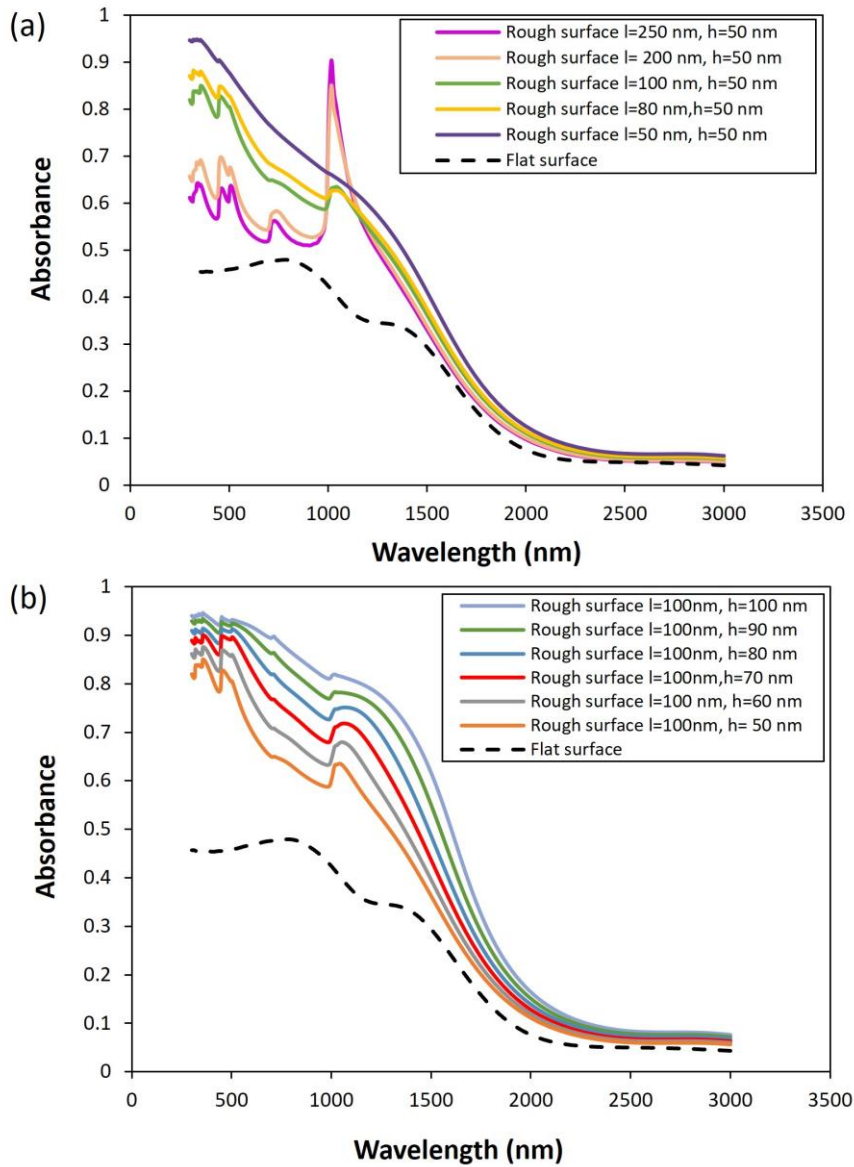


Figure 2. 5: The effect of (a) Correlation length and (b) RMS height in the absorption spectra of an isotropic random rough surface of Tungsten

Note that the higher the surface height, the more light trapping at long-wavelength. It should be noted that the absorption curve at low wavelengths (approximately up to 1000 nm) is flatter with a higher RMS height value. The results point out that the correlation length and RMS height can be used as controlling factors for a spectrally selective absorber. It is shown that for the wavelength in the range of 1000- 1600 nm, a high absorption with a value around 0.95 is obtained just by the roughness of the surface without any additional coatings. In addition, an average of 47% improvement in the absorption is observed in the wavelength in the range of 300-1000 nm for the case of

$l=200$  nm and  $h=180$  nm in comparison to the flat surface. Simulation results show that increasing the RMS height with a selected correlation length increases the bandwidth of the absorption. This increase in absorption is caused by the coupling between the surface peaks' resonant modes. For an RMS height of 180 nm, the absorption curve is over 85% in a wide wavelength range of 300–600 nm. At the same time, for the wavelengths of 1000–1600 nm, the absorption value is more than 95%. For higher RMS height values, the coupling between the surface peak's resonance modes occurs in a wider range of wavelength, which cause a broader bandwidth of absorption.

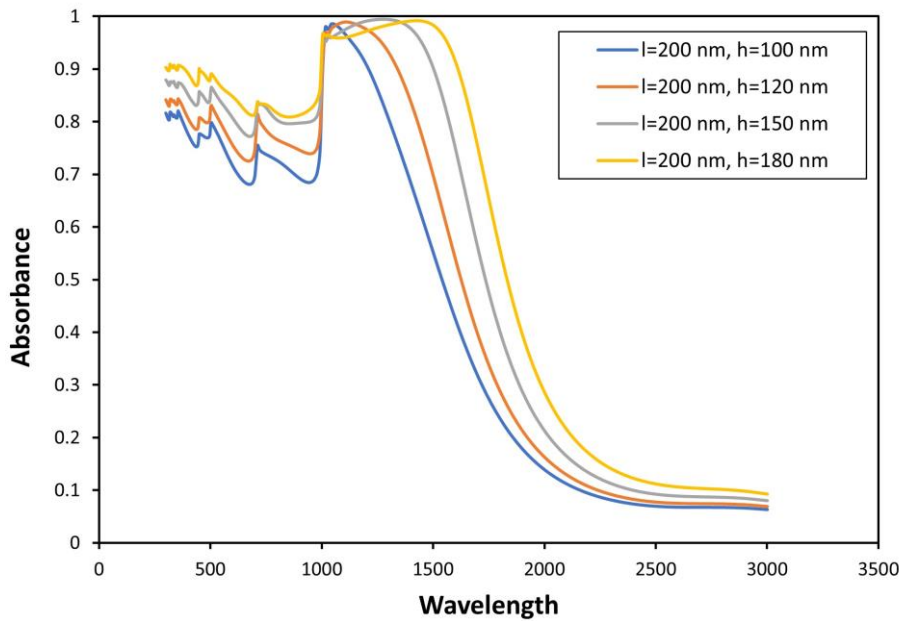


Figure 2. 6: The RMS height effect on bandwidth of absorbance

In the next step, inspired by grating couplers to control the light-matter interaction at material surfaces, we investigated the effect of anisotropic rough surfaces. Anisotropic surface roughness is obtained by a Gaussian surface with two different correlation lengths along  $x$ ,  $y$ , marked as  $l_x$ ,  $l_y$  respectively. Fig. 2.7 illustrates the absorption spectra for various anisotropic surfaces. The results in Figure 2.7 indicate that the absorption of the anisotropic rough surface is smaller than the isotropic rough surface with the same correlation length ( $l_x=200$  nm, Fig. 2.7 (b)) in the  $x$ -direction, which is shown with a black dash line in Fig 2.7 (a). It indicates that with the same correlation length in the  $x$ -direction, increasing the correlation length in  $y$ -direction which causes a drop in absorption values. However, smaller correlation length in  $x$ -direction ( $l_x=100$  nm) in the anisotropic case leads to more absorption in the VIS spectrum (red dash line in Fig. 2.7 (a) and 2.7 (c)).



Moreover, higher absorption can be obtained in the infrared region for the anisotropic case of  $l_x=100$  nm,  $l_y=400$  nm, and  $h=100$  nm. The absorption results of Tungsten anisotropic rough surface with  $l_x=200$  nm and  $l_y=800$  nm, which is shown in Fig. 2.7 (d), shows two clear resonance peaks in its spectrum the first one is in 533 nm with 85% absorption, and the second one is 1082 nm with 87% absorption. In addition, the results show that anisotropic rough surfaces with lower correlation length in the x-direction can be used to obtain higher absorption in comparison to the isotropic rough surfaces with higher RMS height. In other words, at the same RMS height, anisotropic rough surfaces with lower correlation length can be used instead of isotropic rough surfaces to have more absorption in VIS and near-infrared region.

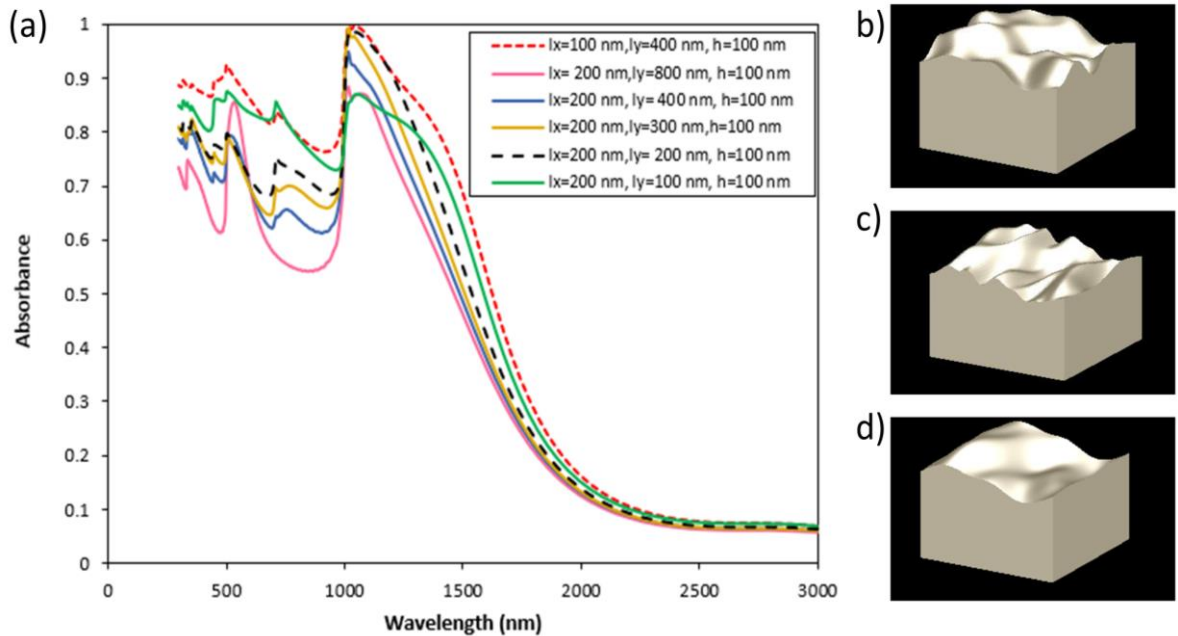


Figure 2.7: (a) The effect of correlation length for W anisotropic rough surface (b) Isotropic rough surface with  $l=200$  nm and  $h=100$  nm. (c) Anisotropic rough surface with  $l_x=100$  nm,  $l_y=400$  nm, and  $h=100$  nm. (d) Anisotropic rough surface with  $l_x=200$  nm,  $l_y=400$  nm, and  $h=100$  nm

An interesting observation in Fig. 2.7 involves the two cases with a red dashed line ( $l_x=100$  nm,  $l_y=400$  nm) and a green solid line ( $l_x=200$  nm,  $l_y=100$  nm) with  $h=100$  nm. At an initial glance, even though the green solid line seems rougher than the red one, the red dashed line has higher absorption. The main reason for this is the polarization direction of the incident electric field and how it interacts with the anisotropic surfaces.

In this case, the incident electric field is polarized in the x-direction. As a result, the x-polarized incident field is more sensitive to the roughness in the x-direction. In this case, the red dashed line is rougher in the x-direction ( $l_x=100$  nm) compared to the green solid line ( $l_x=200$  nm). This leads to a stronger absorption of the x-polarized incident field, even though the overall roughness of the green solid line is larger. An important consequence for anisotropic rough surfaces is that the roughness in the direction of polarization is more important than the overall roughness.

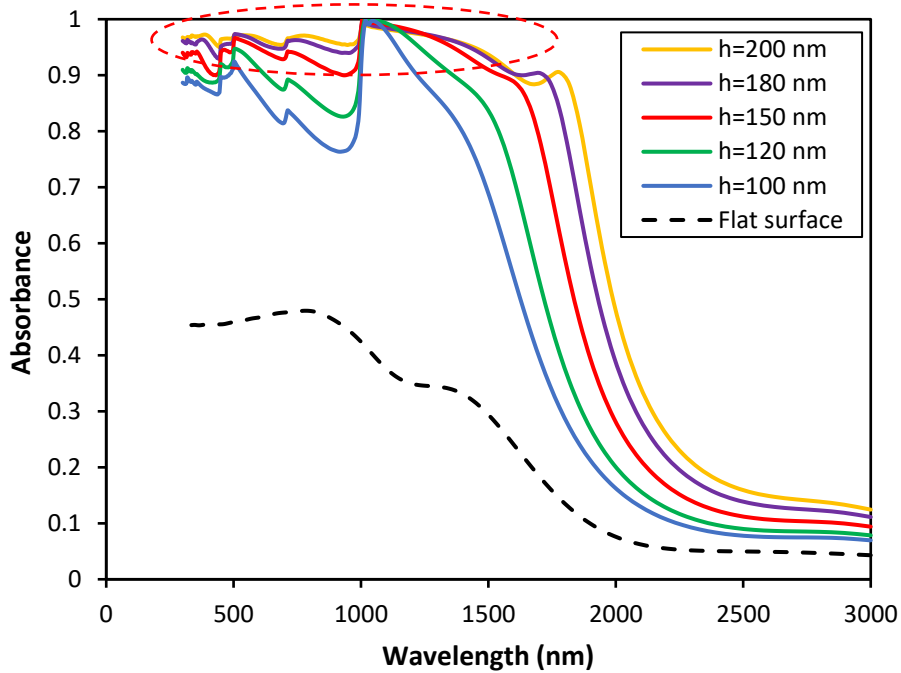


Figure 2. 8: The RMS height effect on the absorbance of the anisotropic rough surface of Tungsten with  $l_x=100$  nm,  $l_y=400$  nm

In Fig. 2.8, the effect of RMS height on the spectral absorption is investigated. As mentioned before, for isotropic rough surfaces with increasing the RMS height, the absorption bandwidth increases. It is observed that starting from  $\lambda=1000$  nm; the perfect absorption spectrum is continuously broadened. For anisotropic random rough surfaces, a broad bandwidth is obtained with increasing the RMS height of the surface. This broad spectral region starts from  $\lambda=300$  nm and continues up to  $\lambda=1500$  nm. It is shown that for the case of the anisotropic rough surface with  $l_x=100$  nm and  $l_y=400$  nm and RMS height of 150 nm the absorption is more than 90%. While taking this into account, the absorption

curve has a maximum in the wavelength range of 300 nm to 1700 nm and covers the visible and near-infrared region. Moreover, for the RMS height of 180 nm the absorption reaches to more than 95% which is a significant improvement in comparison to a smooth surface. Broad absorption spectra were previously reported in the literature, but in all cases another material coating was added on to Tungsten to achieve such high absorptions [29,146]. We report such broad absorption spectra by surface modifications. Moreover, in comparison to the flat Tungsten surface, the absorption enhanced around 52% in the VIS region and approximately 80% for larger wavelengths from 1500-2000 nm.

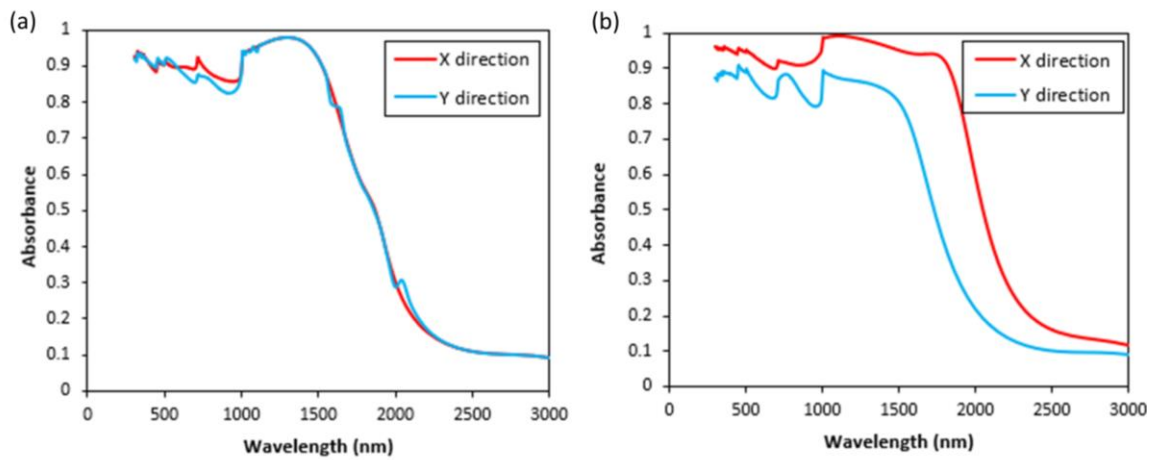


Figure 2. 9: Polarization direction effect on absorption spectrum for (a) isotropic surface ( $l=200$  nm,  $h=180$  nm) (b) anisotropic surface ( $l_x=100$  nm,  $l_y=400$  nm, and  $h=180$  nm)

As mentioned earlier a plane wave is used to illuminate the structures in our simulations. Moreover, the electric field is parallel to the surface and polarized in the x direction and k vector is perpendicular to the structure. Polarization direction and angle of incidence are two other factors in studying scattering from a random rough surface. In this regard, the polarization direction in x and y direction corresponding to different wavelength is plotted in Fig. 2.9 for isotropic and anisotropic surfaces. For isotropic structures, changing the polarization does not affect the absorption spectrum as can be seen from Fig. 2.9 (a), since the incident wave interacts similarly with features in both directions for the isotropic case. However, changing the polarization affects the results for the anisotropic case. As is shown from Fig. 2.9 (b) polarization in the y direction will cause a reduction in absorption values for the anisotropic surface in this case.

Fig. 2.10 illustrates the absorption spectrum for various incidence angles ranging from 0 to 60 degree for an isotropic rough surface with  $l=200$  nm and  $h=180$  nm. As studied in the literature [158] the incident angle is an important factor in studying the light scattering from a metal rough surface. To show the importance of incident angle some studies have been done to introduce a structure to have a broadband absorption in most incident angles [159,160]. For the structure introduced in this study as a selective absorber, it can be seen from the figure only in 0 degree of incident we have a broadband absorption (red line). Moreover, by increasing the degree of incident the peak band becomes narrow but redshifts to longer wavelength. In addition, the overall absorption decreases when the incidence angle increases. Especially in the infrared range a significant decrease in absorption is observed by increasing the incidence angle for this particular surface geometry.

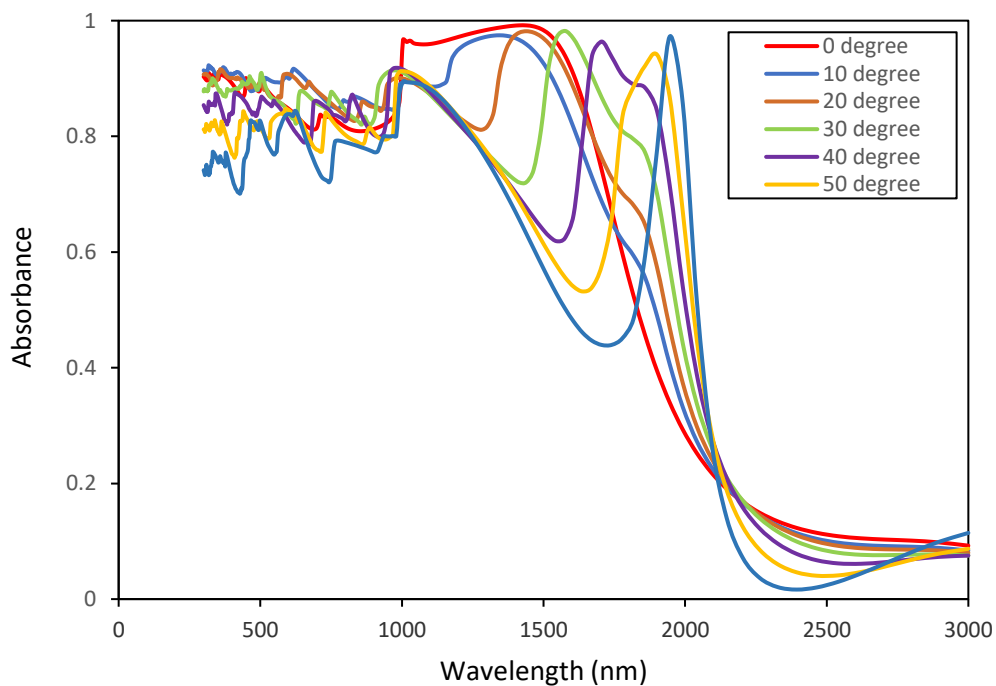


Figure 2.10: Absorbance spectrum regarding to different incidence angles for an isotropic random rough surface

### **3. COLORAZATION OF PASSIVE RADIATIVE COOLING COATINGS USING PLASMONIC EFFECTS**

In this work, we address the colorization of passive radiative cooling surfaces by using a plasmonic nanoantenna to achieve structural color for aesthetic purposes, while maintaining the radiative cooling power. First, we outline a methodology to design a daytime passive radiative cooling structure with optimized thin-film layers with the aim of cooling power maximization. Then, to add color to the system a plasmonic nanostructure is proposed and analyzed, which is defined as a silver plasmonic bowtie nanoantenna that is placed between reflector and emitter layers to have both high cooling power and colorization together. The optical properties of the plasmonic nanoantenna, including absorption spectra, gap enhancement, and electric field distribution in this study, are numerically investigated by means of the finite-difference time-domain (FDTD) method. We also examine the effects of the nanoantenna parameters on the resonance wavelengths of the proposed structure to examine the display color of radiative cooling.

#### **3.1. Materials and Methods**

To cool a surface under direct sunlight, the design of radiative cooling materials must meet two criteria simultaneously. First thermal emission within the atmospheric transparent window ( $8 \leq \lambda \leq 13 \mu\text{m}$ ), and second, reflection at the rest bands ( $0.3\text{--}8 \mu\text{m}$  and  $13\text{--}24 \mu\text{m}$ ). In this section, a detailed methodology for designing passive radiative cooling is presented, and a new design using the plasmonic nanostructure is introduced to add color.

### 3.1.1. Principle of Radiative Cooling

Passive radiative cooling relies on the reflection of undesired radiative components and the radiative transfer of heat away from the surface to the cold outside environment. The net cooling power per unit area of a structure is denoted as  $P_{Cool}(T)$ , is calculated by

$$P_{Cool}(T) = P_{rad}(T) - P_{atm}(T_{amb}) - P_{sun} \quad (3.1)$$

Where,  $P_{rad}(T)$  is the power radiated by the structure per unit area and define as,

$$P_{rad}(T) = \int d\Omega \cos \theta \int_0^{\infty} d\lambda I_{BB}(T, \lambda) \epsilon(\lambda, \Omega) \quad (3.2)$$

In this equation,  $\epsilon$  is the object's emissivity. The absorbed power per unit area emerging from the atmosphere is presented as  $P_{atm}(T_{amb})$  and define by

$$P_{atm}(T_{amb}) = \int d\Omega \cos \theta \int_0^{\infty} d\lambda I_{BB}(T_{amb}, \lambda) \epsilon(\lambda, \Omega) \epsilon_{atm}(\lambda, \Omega) \quad (3.3)$$

Where,  $T_{amb}$  is the ambient temperature and  $\epsilon_{atm}$  is the emissivity of the atmosphere.  $P_{sun}$  is the amount of solar power that is absorbed by the structure per unit area.

$$P_{sun} = \int_0^{\infty} d\lambda \epsilon(\lambda, \theta_{sun}) I_{solar}(\lambda) \quad (3.4)$$

In above equation,  $I_{solar}$  is the AM1.5 Global tilt spectrum, which is given in Ref [161]. For a given incidence angle,  $\theta_{sun}$ , and wavelength, the quantity of absorbed radiation may be computed by multiplying incident solar irradiation,  $I_{solar}$ , by the emissivity/absorptivity of the object. In Eqs. (3.2) and (3.3),  $I_{BB}$  represents the blackbody radiation which defines by Planck's law as below

$$I_{BB}(T, \lambda) = \frac{2hc^2}{\lambda^5} \frac{1}{e^{hc/\lambda k_B T} - 1} \quad (3.5)$$

Where  $h$  represents the Planck constant,  $c$  represents the speed of light,  $k_B$  represents the Boltzmann constant, and  $T$  represents the temperature. These equations are used to evaluate the cooling power of the structures under consideration.

As a non-color radiative cooling device, we designed a layered structure comprising of thin coatings on a metal Ag to obtain high reflectivity in the solar spectrum and strong absorption in the mid-infrared band for passive daytime radiative cooling below the ambient temperature.

Figure 3.1 shows the geometry of the designed cooler. To control the reflected light in the visible spectrum and the emitted light in the atmospheric spectrum, separate optimizations for the thickness of reflector layers and emitter layers were performed in this study to have high reflectance in the solar spectrum while having high cooling power; this means that the reflected coatings should reflect in the spectrums with high solar energy as well as where the atmosphere is opaque. The emission, on the other hand, should be increased in the transparency window to increase the quantity of energy released to the sky by the object. To achieve this, SiO<sub>2</sub> and TiO<sub>2</sub> layers are used due to their low absorption in the visible and near-infrared spectra but considerable absorption in the 8–13 μm region. Moreover, Ag is also applied to the bottom of the structure to achieve high reflection in the visible and near-infrared spectral ranges. The material properties of TiO<sub>2</sub> and SiO<sub>2</sub> are referred from Palik’s handbook [162,163]. The thickness of layers is optimized using a genetic algorithm (GA) with the aim of maximizing the cooling power which is shown in

Figure 3.1.

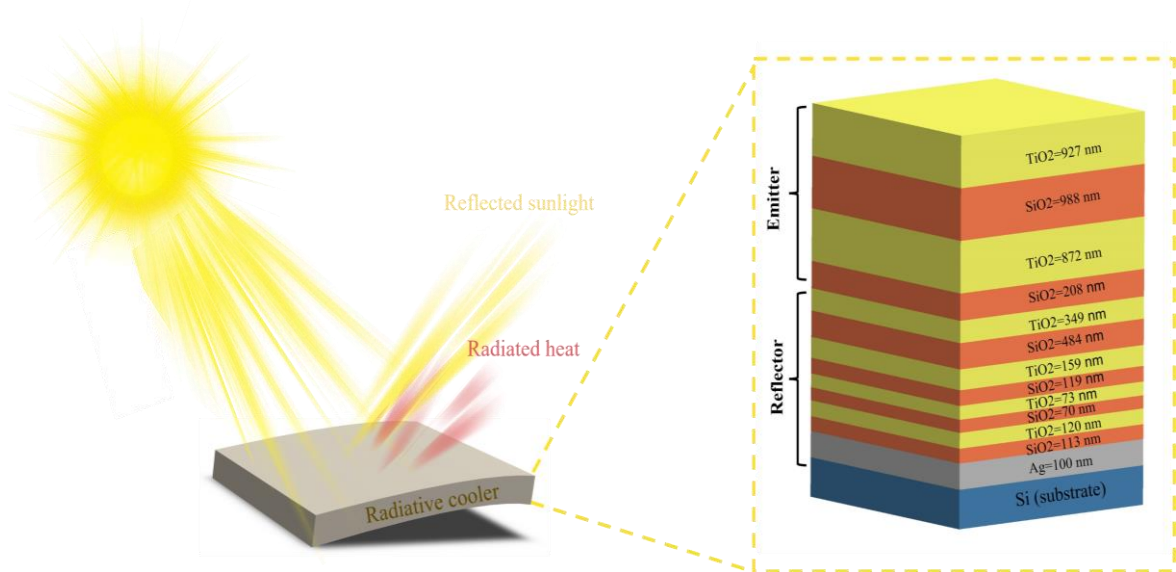


Figure 3.1: Schematic of designed non-color radiative cooling

The details of thickness optimization for our proposed structure is given in reference [48]. As it is discussed in this study, to emphasize the effect of spectral behavior on cooling power, optimization is done based on maximizing cooling power which is define as  $\max P_{cool} = P_{rad} - P_{atm} - P_{sun}$  . In this optimization procedure after defining number of layers and materials, the surface impedance of the final structure is formed by taking layer thickness as a variable. Then the reflectance coefficients calculated using Eq. (3.6).

$$\Gamma_1 = \frac{Z_1 - Z_0}{Z_1 + Z_0} \quad (3.6)$$

Where  $Z_1$  is the impedances for the front surface and  $Z_0$  is the impedances for free space. Then the surface impedance values are mapped to the complex gamma plane by normalizing reflection coefficients using Eq. (3.7).

$$\Gamma_{Norm} = \frac{Z_1/Z_0 - 1}{Z_1/Z_0 + 1} \quad (3.7)$$

Where  $\Gamma_{Norm}$  is the normalized reflectance coefficient. At the end the residual errors are defined from the normalized gamma values and inserted to the cost function, where the layer thicknesses are calculated.

In this study in optimization using GA, the cost function defined as Table 3.1 for optimizing thickness of reflector layers and emitter layers. As it is written in Table 3.1, in optimizing reflector layers more weighting goes to reflection part because in our design it is crucial to have high reflection in solar spectrum specially in visible region. In this table mean (Reflection) is the max reflection that could obtain with an optimized thickness of reflector layers. Weighting values are selected based on obtained average reflection in the defined wavelength range. The selective reflectivity is achieved by putting high index- low index layers that is highly reflective inside the solar spectrum on the top of a strong reflector Ag. The thin layer coatings of the reflector part result in a higher reflection percentage in the visible and near-infrared spectrums. The thicker layers are obtained for emitter layers. The emitter part radiates thermal energy towards space within the atmospheric window range while the thinner reflector layers reflect the unfavorable irradiation.



Table 3.1. Cost function definitions in thickness optimization using GA optimization

Reflector layers	Emitter layers	Spectral region
Cost1 = max {Reflection (region 1)}	Cost1 = min {reflectance (region 2)}+ max {reflectance (region 3)}	Region 1: $\lambda \leq 8 \mu\text{m}$
Cost2 = max $P_{\text{cool}} = P_{\text{rad}} - P_{\text{atm}} - P_{\text{sun}}$	Cost2 = max $P_{\text{cool}} = P_{\text{rad}} - P_{\text{atm}} - P_{\text{sun}}$	Region 2: $8 \leq \lambda \leq 13 \mu\text{m}$
Cost = (weight) Cost1+ (1-weight) Cost2 Weight = 0.9	Cost = (weight) Cost1+ (1-weight) Cost2 Weight = 0.5	Region 3: $13 \leq \lambda \leq 24 \mu\text{m}$

The number of layers obtained from a parametric study using the FDTD method and the final structure is selected based on calculated cooling power using Eqs (3.2) - (3.4). It is obvious that adding extra coating increase the cooling power but after 12 layers the rate of this increasing slow down so adding extra coatings in compared to the cost we add to the system is not logical. On the other hand, the reflection value with 12 layers in solar spectrum is higher. As a result, a total of 8 layers of reflector coating and 4 layers of emitter coating is selected. In this structure, the first eight layers, beginning with Ag, are responsible for solar reflection, while the top four larger layers operate as absorptive portions. While the presence of a strong metal at the bottom of the stack is responsible for the reflection, the interference between the layers above further improves the reflection. The incoming wave is partially reflected in the visible and near-infrared spectrums by each layer above the Ag, whereas the remainder is transmitted to the bottom layer. The remaining of the wave's energy is reflected once it hits the silver layer. In this research, average reflectance and emission values are derived by averaging over the wavelength. A reflection of approximately 97% and an emission of almost 70% are obtained in the 0.3–4  $\mu\text{m}$  spectrum and 8–13  $\mu\text{m}$  spectrum, respectively.

An ideal radiative cooling structure is shown in Figure 3.2, which has no absorption in the solar spectrum and near-infrared between 0.3 and 8  $\mu\text{m}$  but has a unity emissivity across the infrared spectrum from 8 to 13  $\mu\text{m}$ . In this figure, the AM1.5 solar spectrum and atmospheric transmittance are shown as a reference. The red line in this figure shows the ideal reflection for radiative cooling, and the blue line shows the ideal emissivity for radiative cooling. Consequently, such a radiative cooler may effectively dissipate heat while being completely sun reflective and having a high thermal emissivity. The cooling power of 122.3  $W/m^2$  is calculated using Eq. (3.1) to (3.5) for this ideal radiative cooling. However, it should be mentioned that in general, no multilayer structure can reach the exact target spectral radiative features. Therefore, it is only possible to find a

design of a multilayer structure with radiative properties relatively close to the target features. Here in this study, we aim to design a structure to have radiative properties near the ideal radiative cooling

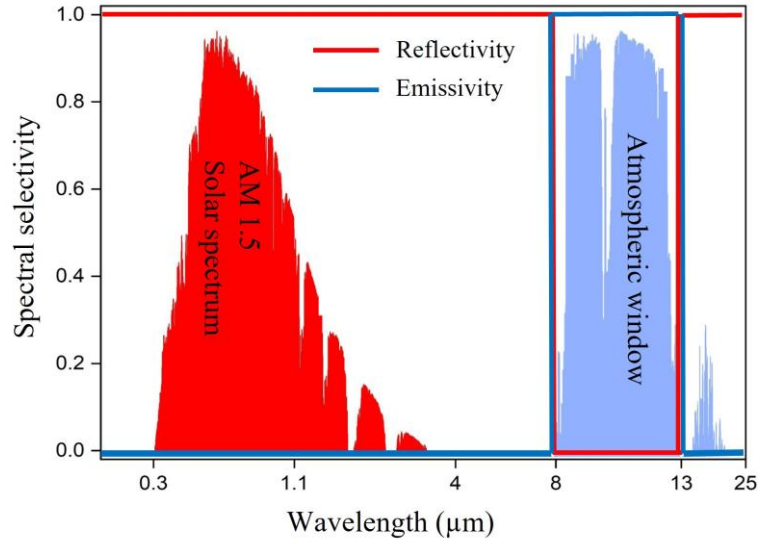


Figure 3.2: The ideal optical response of radiative cooling, AM 1.5 solar spectrum (red) and atmosphere transmission (blue)

### 3.1.2. Principle of Color Display

To provide high-purity colors, colored radiative coolers must not only meet the spectral parameters of the conventional radiative cooler stated in the previous section, but also display reflectance dips at the wavelengths of the subtractive primary colors (visible region 300-800 nm). In literature, the colorization is achieved by changing the thickness of MIM layers [87,93,164], using photonic structures [86], changing the size of nanoparticles inserted into the materials [165], and similar methods. Most of them decrease the cooling power significantly, and in some of them, the need to increase the thickness of Ag layer caused an increase in the cost of design. However, in this study, we proposed a bowtie shape nanoantenna structure as the color-displaying structure to absorb light of a specific spectrum in the visible region due to the enhanced electric field in the gap between nano antennae. Strong plasmonic coupling occurs between the two triangular nano prisms at the gap of the nanoantenna, altering the emissivity and increasing the absorptivity, which is desired for color generation. In our proposed design, the layer thicknesses are commensurate with those of a traditional radiative cooler. For color display we combined the concept of adding metal on top of reflector layers for producing

colors and concept of plasmonic structure to control the colors. The interaction between light and metallic surface and the enhanced electric field due to the dipole effect of bowtie nano antenna cause strong but narrow absorption in visible range. The schematic model of the proposed bowtie shaped nanoantenna on top of reflector layers are shown in Figure 3.3 (a)–(b). As shown in this figure, the length of each triangle  $L$ , the width of the triangle  $H$ , the apex angle  $\alpha$ , the gap between two triangles  $g$ , and the thickness  $t$  are the fundamental characteristics of the bowtie. The proposed bowtie nano antenna as a plasmonic nano structure which can absorb light in the visible region is placed on top of the reflector layers in conventional radiative cooling. The range of colors obtained in this study using this structure is shown in Figure 3.3(c). To display the effect of the plasmonic nanoantenna on the reflection spectrum in Figure 3.3(d), the reflection spectrum of non-color radiative cooling and colored radiative cooling is plotted.

To figure out the color of the surfaces, the reflection spectrum should be converted to a color. The color of an object depends on a number of factors, including the illuminant's spectral power distribution, the item's reflectivity in the visible spectrum, and color matching functions. The first one depends on the surroundings, such as the sun, the light source, etc. The second may be altered by modifying the materials and structures. The last is a numerical representation of the human eye's chromatic response, which was empirically defined in 1931 by the CIE (International Committee on Illumination)-XYZ color space. The computed reflectivity spectra of the coatings and the spectral intensity of the light source are used to determine the reflected spectral intensity. D65 lighting, a CIE standard depicting outside illumination that takes the environment into consideration, is employed as the source. It is multiplied by the coating's reflectance to get the reflected spectral intensity. The CIE model is then used to convert the spectrum to colors. CIE19 defines color matching functions that relate the spectrum reflected intensity to the color. These capabilities correspond to the way the human eye senses color, namely by the use of three detectors (cone cells) capable of detecting red, blue, and green. Using the spectral reflected intensity and color matching functions, it is possible to determine the parameters  $X$ ,  $Y$ , and  $Z$ , which correspond to CIE color space coordinates. To determine the spectral reflection of the proposed radiative cooling structure with nano-antennas, numerical research using the FDTD technique has been conducted across a wavelength range of 0.3 to 25  $\mu\text{m}$ . To prevent field reflections in the  $z$ -direction, the periodic boundary conditions along the  $x$  and  $y$  directions and the perfectly matched layer (PML) boundary condition

are applied. The illumination is provided by a plane wave light source with propagation direction and polarization along the negative z-axis and x-axis, respectively. Silver is employed as the nano-antenna material between reflector layers and emitter layers.

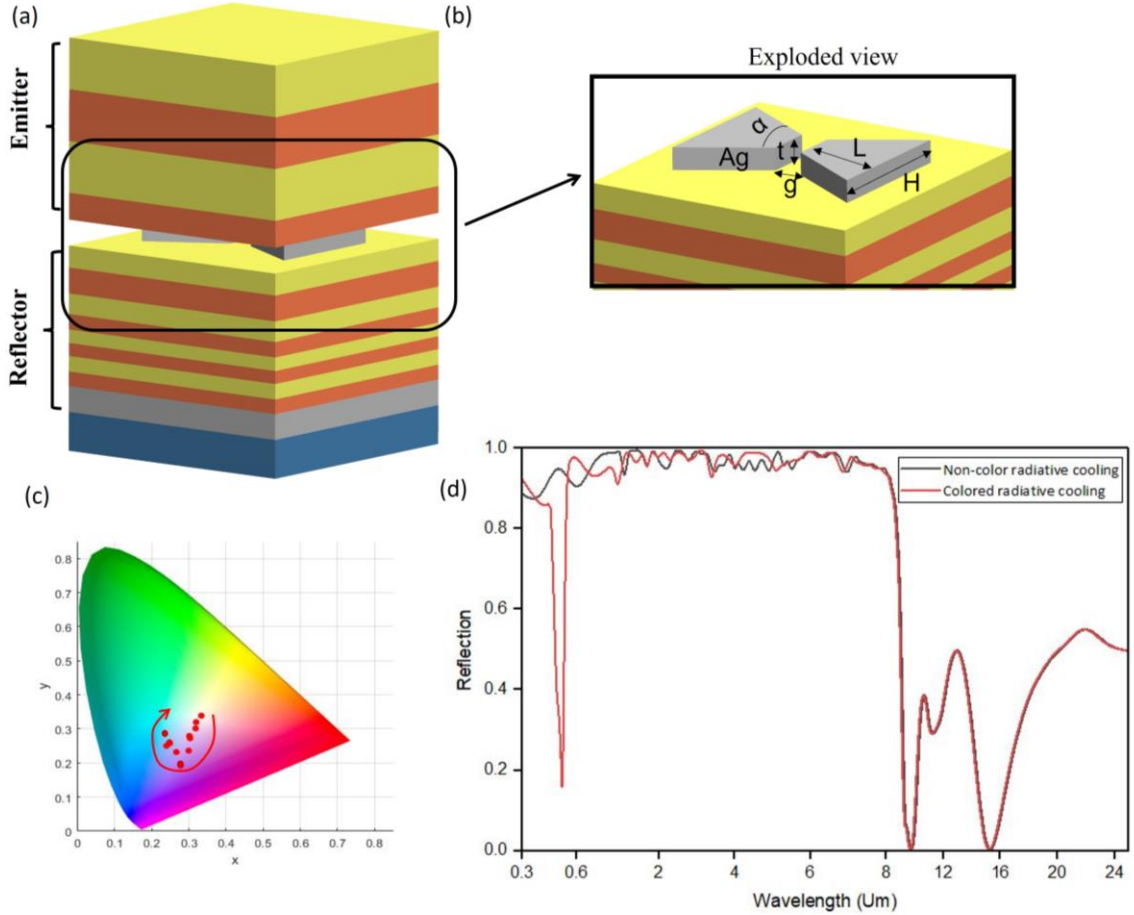


Figure 3.3: (a) Schematic diagram of Colored radiative cooling structure (b) exploded view of bowtie nanoantenna on top of reflector layers (c) color place in chromaticity diagram (d) reflection spectrum of non-color and color radiative cooling

To transform a reflection spectrum into an assessment of color in the CIE system, the stimulus quantities X, Y, and Z for the three fundamental colors should be calculated in order to theoretically assign all colors.

$$X = \frac{\int R(\lambda)I(\lambda)\bar{x}(\lambda)d\lambda}{I(\lambda)\bar{y}(\lambda)} \quad (3.6)$$

$$Y = \frac{\int R(\lambda)I(\lambda)\bar{y}(\lambda)d\lambda}{I(\lambda)\bar{y}(\lambda)} \quad (3.7)$$

$$Z = \frac{\int R(\lambda)I(\lambda)\bar{z}(\lambda)d\lambda}{I(\lambda)\bar{y}(\lambda)} \quad (3.8)$$

where  $I(\lambda)$  denote the spectral power distribution,  $R(\lambda)$  denotes the spectral reflectivity, and  $\bar{x}(\lambda)$ ,  $\bar{y}(\lambda)$ , and  $\bar{z}(\lambda)$  denote the color matching functions, which correspond to the spectral tristimulus values received by the observer under standard chroma. The chromaticity of the color is determined by the normalized parameter below

$$x = \frac{X}{X + Y + Z} \quad (3.9)$$

$$y = \frac{Y}{X + Y + Z} \quad (3.10)$$

$$z = \frac{Z}{X + Y + Z} \quad (3.11)$$

In the chromaticity diagram, the color is represented by the x, and y chromaticity coordinates, which are derived from the 1931CIE-XYZ color system's reflection spectrum. Transposing the XYZ space characteristics into Lab space using the relationships shown below may provide information on the look of the color.

$$L = f\left(\frac{Y}{Y_b}\right) \quad (3.12)$$

$$a = \frac{500}{116} \left| f\left(\frac{X}{X_b}\right) - f\left(\frac{Y}{Y_b}\right) \right| \quad (3.13)$$

$$b = \frac{200}{116} \left| f\left(\frac{Y}{Y_b}\right) - f\left(\frac{Z}{Z_b}\right) \right| \quad (3.14)$$

where,

$$f(A) = 116A^{1/3} - 16 \quad \text{if } f(A) \geq 8 \quad (3.15)$$

$$f(A) = \left(\frac{29}{3}\right)^3 A \quad \text{if } f(A) \leq 8 \quad (3.16)$$

Here, the  $X_b$ ,  $Y_b$  and  $Z_b$  are the three parameters of a white reference that was selected. The white reference in this investigation is the white hue generated by a radiative cooler without a nanoantenna.

### 3.2. Results and discussion

Following the principles outlined above, we construct the multilayer radiative cooler which has an excellent spectrum selectivity from sunlight to infrared bands. To achieve high cooling power while maintaining high solar spectrum reflectivity and transparency-window emissivity, the layers thickness is obtained which is shown in Figure 3.1 and is used in the whole simulations in this paper. In Figure 3.4, the effect of number of layers on reflection spectrum and cooling power is displayed. High reflectance in the sunlight spectrum necessitates the use of constantly shifting layers of high and low index reflectance ( $\text{SiO}_2\text{-TiO}_2$ ). The optimal number of layers is achieved by solving for layers 8 to 14 with the odd number of layers in the simulation. Figure 3.4(a) depicts the spectral distribution of reflectance, with selective emission occurring in the 8–13  $\mu\text{m}$  spectrum and strong reflection occurring in the solar spectrum. It should be emphasized that the normal incidence is considered unless indicated explicitly. Due to the importance of high reflectivity in solar spectrum especially visible range for colorization purpose, it is apparent that 12 number of layers shows better performance in solar spectrum. It can be seen that the average reflectivity of the entire structure can reach above 98% in range of 0.4-4  $\mu\text{m}$  for 12 layers structure. This structure has a near-zero emissivity in the solar incidence band, which allows it to reflect as much solar radiation energy as possible and so attain greater cooling power. As a consequence of having such a high reflectivity in the visible range, a white color display is produced. The cooling power of these structures is then computed and presented in Figure 3.4(b). As seen, there is a clear upward trend in cooling power as the number of layers increases ( $T_{surf} = 300 \text{ K}$  and  $T_{amb} = 297 \text{ K}$ ). With 12 layers on top of the Ag layer the cooling power reaches  $87 \text{ W/m}^2$ , however, increasing the number of layers to 14 does not result in a substantial gain in cooling power, and the reflection values in the solar spectrum slightly reduced. Consequently, the total number of 12 layers was chosen for the non-color radiative cooling structure in this work.

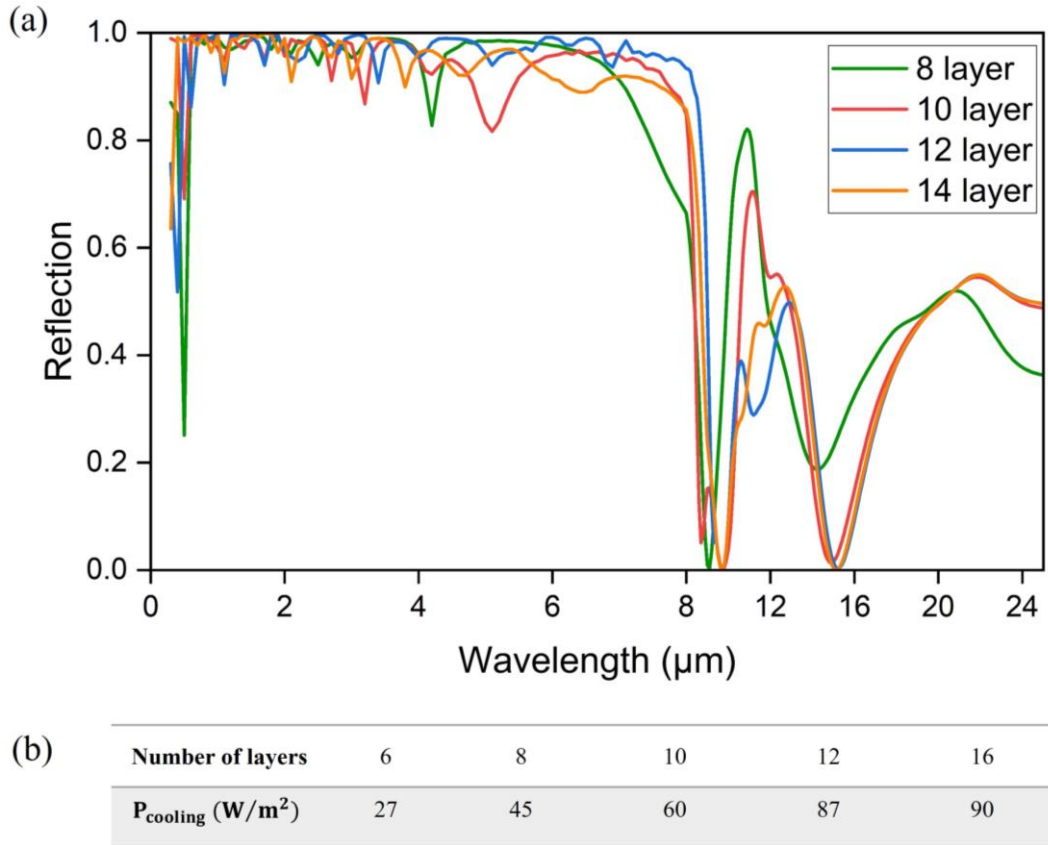


Figure 3.4: (a) Reflection spectrum of layered radiative cooling with a various number of layers for non-color radiative cooling design. (c) The cooling power corresponds to each layered radiative cooling

In order to achieve the color display, we construct a colored radiative cooler, as illustrated in Figure 3.3 (a). Bowtie nanoantenna structure may be readily adjusted to modify the color display characteristics of the colored radiative cooler. The gap between nanoantenna causes the strong field enhancement, where bowtie antennas are coupled to active emitters in order to tailor their emissive properties. These properties can be actively used to obtain colors in radiative cooling. Changing the parameter of the bowtie nanoantenna causes the colored radiative cooler to display different colors. To analyze the colors could obtain using the proposed structure, the thickness of Ag is fixed at 50 nm, and the gap ( $g$ ) between two parts of the nanoantenna, the length ( $L$ ) of the nanoantenna, and the height ( $W$ ) of nanoantenna are changed to determine the range of colors could obtain using the structure. In the absence of the color display module, the remainder of the construction may be seen as a standard white-color radiative cooling module. In contrast to conventional radiative coolers, the colored-displaying structure

displays a greater emissivity and a lower reflectivity in the visible spectrum (400-700 nm), resulting in the production of color. Consequently, the absorbed solar radiation energy  $P_{sun}$  increases from 9 to around 30 W/m<sup>2</sup>, leading to approximately 30% reduction of the net radiation cooling power from 87 to 60 W/m<sup>2</sup>. Essentially, when absorbed solar radiation increases, the radiation cooling power decreases, meaning that the cooling power and the color display are in competition. Consequently, the remaining problem is to find a way to strike a balance between cooling power and color display by varying the structural characteristics of the colored radiative cooler.

Colored radiative cooling structure spectral behavior throughout the whole spectrum from 0.4-25  $\mu\text{m}$  is shown in Figure 3.5. The effect of different parameters of bowtie nanoantenna on the reflection spectrum is plotted in Figure 3.5(a) and the matching color in the chromaticity diagram is shown in Figure 3.5(b), and the resultant color is presented in Figure 3.5(c). It is seen that the reflectivity spectra overlap mostly, and the only difference occurs in the visible spectrum. This structure, in conjunction with colors, may be used to achieve a positive value of radiative cooling; however, a balance between the vividness of the color and the radiative cooling power must be struck since increasing one results in a reduction in the other. It demonstrates that modifying the geometrical parameters results in a change in the reflectance dip and the generation of distinct color combinations. It should be mentioned that the combination of all geometrical properties will result in the creation of new colors. Here in this figure 12 case is assumed and to study the effect of one parameter the other parameters assumed fixed. To study the gap size effect on the reflection spectrum, the two other factors are fixed at  $L=125$  nm and  $H=250$  nm, and when the length of nanoantenna is studied, the  $g=30$  nm is considered while  $H$  is still 250 nm. For the other factor ( $H$  effect) the  $L=125$  nm and  $g=30$  nm are assumed. However, it is clear that changing all the factors together may cause different colors.



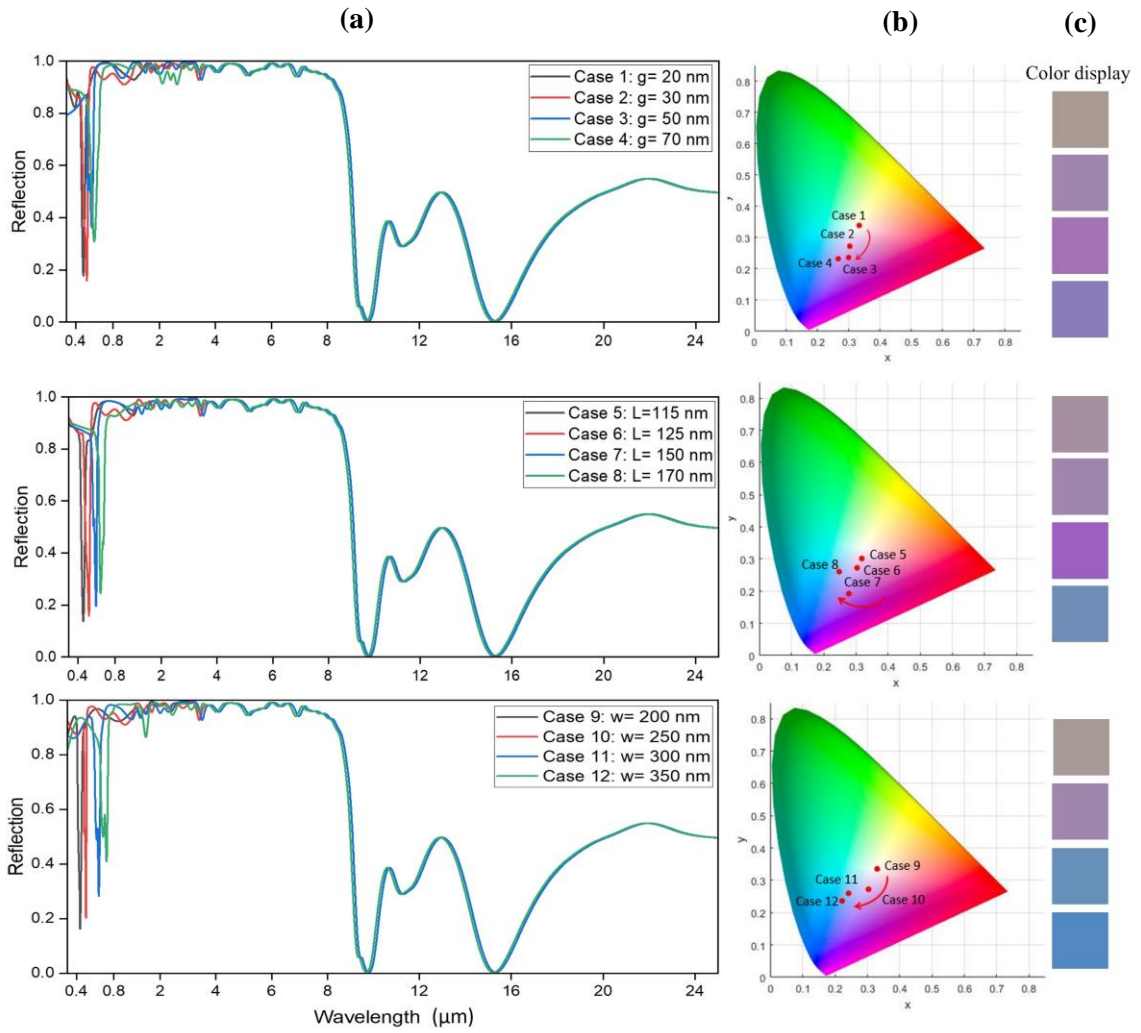


Figure 3.5:(a) The reflection spectra of various colored radiative cooler structures at the normal incident (b) the corresponding colors of structures in the chromaticity diagram. (c) the displayed color of colored radiative cooling structures

It should be noted that the primary difference between conventional and colored radiative coolers lies in their different levels of emissivity/reflectivity in the visible band for color display and that higher levels of emittance and reflection (low reflectivity) in the visible band will cause a reduction in cooling power. As a result, it is clear and reasonable to assume that the introduction of color-display components will result in a reduction in cooling performance to some extent. The precise computation of the cooling effect in Table 3.2 indicates that the addition of color-displaying components will diminish the cooling performance to some degree. In comparison to typical radiative coolers, the incorporation of a color-controlling structure reduces the total reflectivity in the solar spectrum, hence reducing a portion of the cooling power. However, since the cooling structure only affects the visible spectrum and still provides practically adequate cooling power, it is feasible to utilize it when both cooling and coloring are required.

Table 3.2 summarizes the cooling performance of both conventional and colored radiative coolers. Color-display components obviously boost the amount of solar energy received and reduce the amount of radiation that is emitted outward.

Table 3.2: Detailed cooling power performance of conventional and colored coolers at a normal incident




Type of Cooler	Conventional Cooler	Colored Cooler 	Colored Cooler 	Colored Cooler 
$P_{\text{sun}}(\text{W}/\text{m}^2)$	9	28	30	32
$P_{\text{atm}}(\text{W}/\text{m}^2)$	124	124	124	124
$P_{\text{rad}}(\text{W}/\text{m}^2)$	221	213	213	214
$P_{\text{cooling}}(\text{W}/\text{m}^2)$	87	61	59	58

Figure 3.6 (a-l) shows the effects of geometric parameters of bowtie nanoantenna on reflectivity. As can be seen from Figure 3.6 (a-d), the gap (g) between two triangles of nanoantenna affected not only the positions of resonance peaks in the reflection spectrum but also the increasing the gap reduces the value of resonance peak; in other words the emissivity decrease. The smaller gap causes the electric-field intensity to be more strongly localized directly at the gap resulting narrower emissivity spectrum. So, the effect of gap size can lead to two effects: first, there is a rise in field enhancement when there is a shorter gap distance, and second, the resonant wavelength shifts with increasing the gap distance. In Figure 3.6 (e-h), the effect of the length of the nanoantenna on spectral emissivity is displayed. Increasing the length will cause a shift in the resonance peak to a higher wavelength. The height effect is also plotted in Figure 3.6 (i-l), and similar to the other two factors increasing the height of the nanoantenna has an effect on the position of the resonance peak and will cause a decrease in the emissivity values in higher heights. This shift in the position of resonance peak as a result of changing geometrical parameters of a bowtie nanoantenna, and also the strong and weak emissivity values cause generating different colors, which is desired in many applications. This is one of the advantages of the proposed structure for use in radiative cooling applications. With a very narrow layer of Ag and just by changing the geometrical parameters, good range of colors could be obtained. The simple geometry of this plasmonic structure to be used as a color generation

module in layered radiative cooling make it more producible. The bowtie antenna may be made more controllable in the design phase by selecting the proper parameters. One may select the geometric dimensions according to the findings as required.

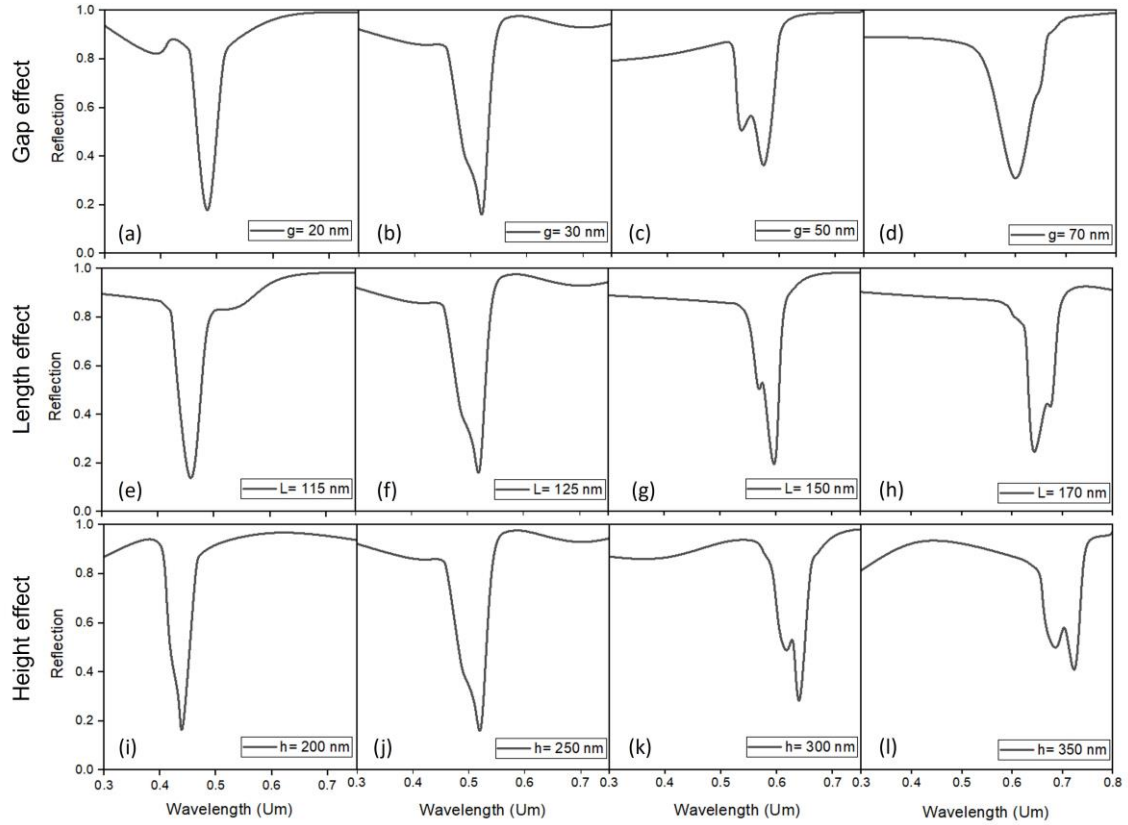


Figure 3.6: (a)-(d) Gap effect of nanoantenna on reflection spectrum. (e)-(h) Length effect of nanoantenna on the reflection spectrum. (i)-(l) Height effect of nanoantenna on the reflection spectrum

Electric field distributions of the proposed nano-antennas corresponding to different gap sizes are presented in Figure 3.7 (a)-(l). According to this figure, when the electric field densities are accumulated more towards the center rather than getting evenly distributed on the long sides of the structures, which demonstrates a large interaction between the triangles of the bowtie, the peak resonance happens, which causes a strong but narrow reduction in reflection spectrum in the visible region which is desired in our application for color generation. This ability can be used in radiative cooling applications to generate colors when a narrow, strong emissivity is needed in visible regions while not altering the rest spectrum. The coupling between the two plasmons of the two triangles produce a plasmon resonance which with increasing the gap size become weaker. From

Figure 3.7 (c),(g),(k), it can be seen that there is a substantial reliance between the electric field and the sensing capabilities of the nano-antennas as in each gap size, the resonance field happens when the high electric field concentration in the gap between nanoantenna due to the strong coupling between the nanoantenna. It is found that as the gap of the bowtie gets smaller, the electric field intensity ( $|E|^2$ ) can reach to higher values which means that resonance happens in lower wavelength as it is shown in Fig. 3.7; at small gap of 20 nm the resonance happened is lower wavelength in compared to bigger gap sizes.

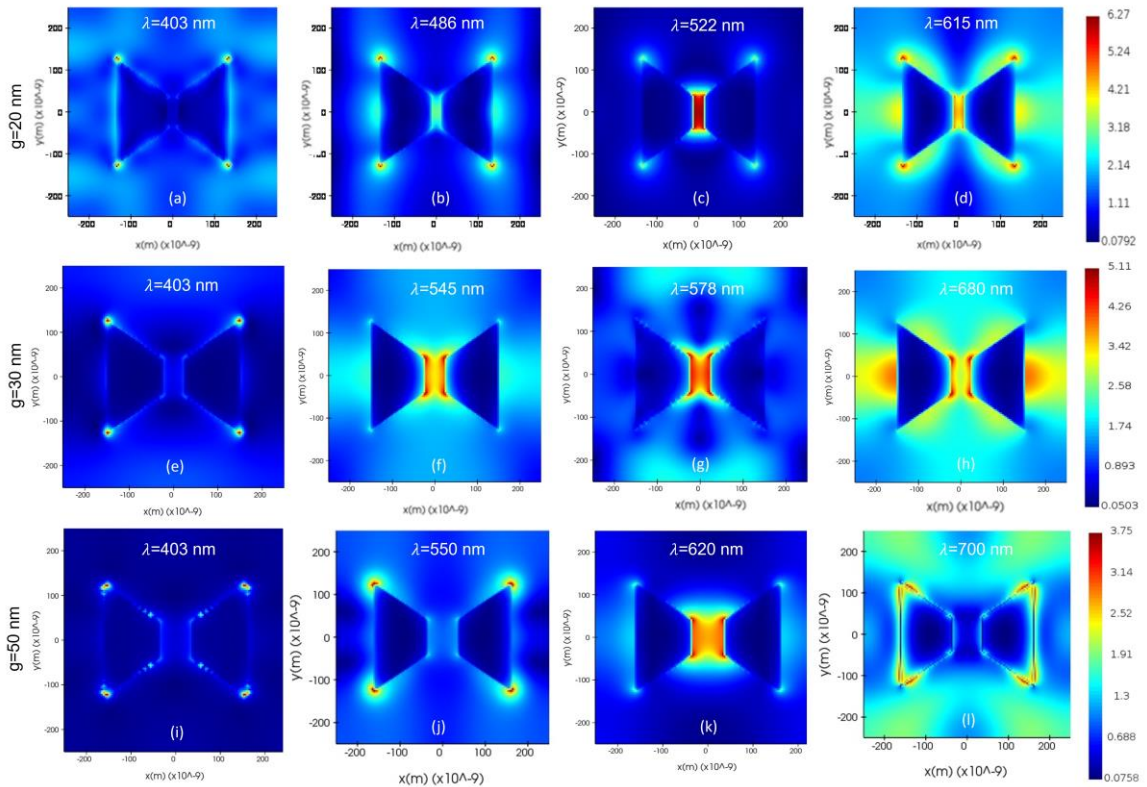


Figure 3.7: The electric field around bow tie nano antennas for different gap size. (a)-(d) g=20 nm (e)-(h) g=30 nm (i)-(l) g= 50 nm

The angular performance of the designed colored radiative cooler is also evaluated. The reflections versus the wavelength and the incident angle for one structure of colored radiative cooling with g=30 nm, L= 125 nm, and W= 250 nm are shown in Figure 3.8 (a). The results indicate that, although the reflection spectra of coolers show the slight shifts with increasing the incident angle but still the colors generate in lighter forms of them; however, due to the reduction of reflection, especially in higher angles, the cooling power decrease dramatically so it couldn't be effective to use it as a radiative cooling in higher angles. To evaluate how nanoantenna thickness affects the optical properties of the

radiative cooling and the resultant color, we evaluated bowties nanoantenna with varying thicknesses ranging from 50 nm to 250 nm. Figure 3.8 (b) shows the reflection spectrum of the colored radiative cooling composed of nanoantenna with thicknesses of 100, 150, 200, and 250 nm; in this figure, color denotes the value of reflectivity. The resultant color from each thickness is displayed in Figure 3.8 (c). As can be seen from the figure, the increasing thickness of nanoantenna leads to a slight change in resonance peak, but its effect on the purity of colors is more prominent. However, the effect of thickness on the sharpness of colors can't be ignored but as reported before, the lighter version of these colors could obtain using a thin film of Ag nanoantenna by changing the other characteristic of it. As a result, what is important is the balance between cooling power, aesthetics, and cost, which could be weight to each of these factors based on the application.

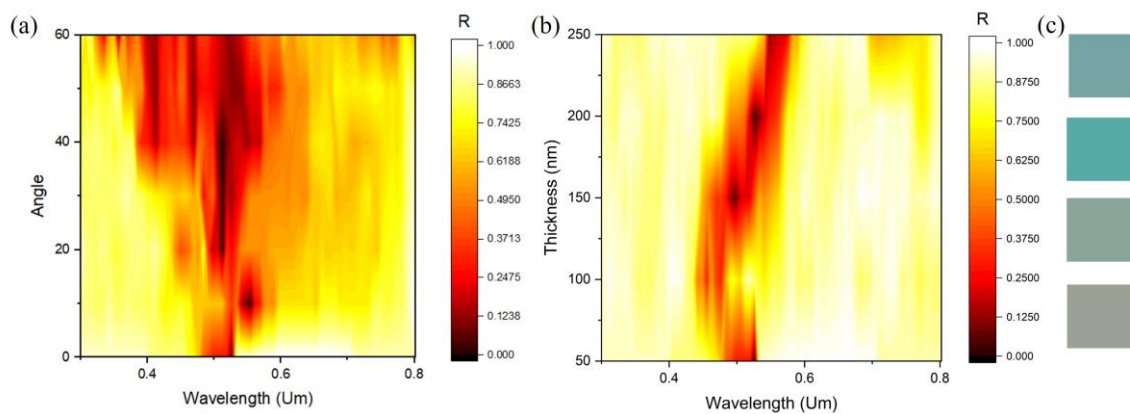


Figure 3.8: Reflection field as a function of (a) angular emission and wavelength (b) thickness of nanoantenna and wavelength (c) resultant colors from various nanoantenna thickness

#### 4. ORIGINS OF THE ENHANCED BROADBAND ABSORPTION IN BLACK SILICON

In this study we uncovered the mechanisms of the enhanced broadband absorption in micro-structured silicon with random and deterministic textures, especially at wavelengths above its bandgap. We considered texture geometry and doping concentration as major influential parameters on the absorptivity of the black silicon and linked those parameters to electromagnetic phenomena, which induce high field intensities. Random texture geometries which is shown in Figure 4. *I(a)*, are analyzed by expressing them by random Gaussian surfaces and spectral characteristics are obtained. Surface geometry is characterized by root-mean-square (RMS) of surface height,  $h_{rms}$  and transverse correlation length  $l_c$ , shown in Figure 4. *I(c)*. Electromagnetic responses of those structures are analyzed by finite difference time domain (FDTD) [140] simulations. Obtained spectral reflection/absorption profiles well agrees with the previously reported results in the literature [117,118,166]. Then, spectral characteristics of random textures are compared to periodicity controlled deterministic patterns, Figure 4. *I(b)* and 4.1(d) and the field distributions are calculated for analysis with FDTD [140]. In summary, geometry of randomly and deterministically textured black silicon structures are studied, results are analyzed based on field distributions. During the analysis, we considered the high field enhancement problem in black silicon as reciprocal of a waveguide problem in which multiple modes are supported throughout the geometry. In addition, high coupling in the transverse directions are observed in the analysis and coupling condition is estimated by adapting an effective wavelength method, which was originally proposed for optical antennas [167]. Our findings show that overall field enhancement in the pure-silicon structure stem from these two different phenomena depending on the width of the features of the textures. These findings reveal the underlying physics of the broadband absorptivity enhancement in black silicon, which can aid the future studies in the field.



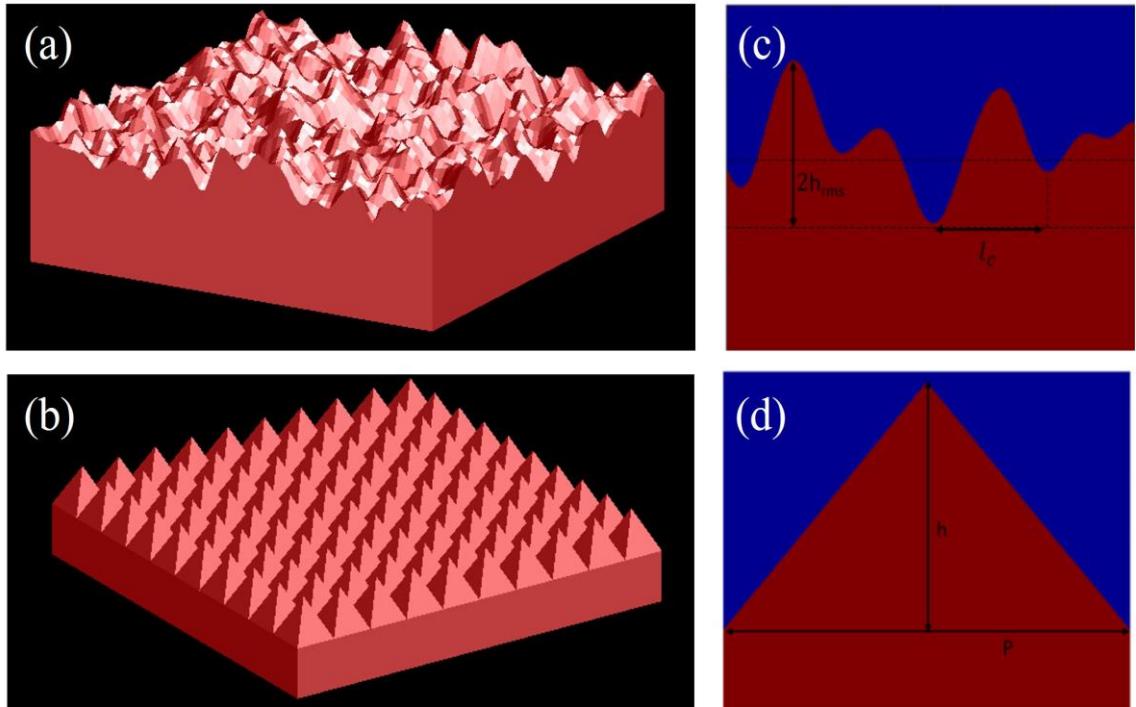


Figure 4. 1: a) Example 3D visual of random texture formed by random Gaussians. b) Example 3D visual of periodicity controlled deterministic texture. c) 2D scheme for random texture with geometric parameters. d) 2D scheme for deterministic texture with geometric parameters.

## 4.1 Methodology

In this section, methodology for random geometry formation and doped optical properties calculations is explained. Generated structures' electromagnetic response is computationally obtained in  $0.3 - 3 \mu\text{m}$  spectrum interval.

### 4.1.1 Rough Surface Generation

A rough surface configuration shown in Fig. 4.1(c) is considered for explaining the random surface roughness effect. The homogeneous random rough surfaces can be generated using spectral density function and discretization of it. In this case, the roughness is characterized by a specified sigma RMS ( $\sigma$ ) which is describing the height

profile and is identical to standard deviation of a random variable and correlation length ( $L_c$ ) which is defining frequencies of spatial variations allowed over the surface. Large correlation length corresponds to small spatial frequencies and vice versa.

The integration of the power spectral density (PSD), which is the Fourier transformation of the surface height self-correlation function [168], over k-space results in the RMS of surface height. Three common spectral density functions are Gaussian, Power-Law and Exponential spectra. For a Gaussian surface, the roughness is randomly distributed with a PSD function, which follows a Gaussian distribution. In this study, Gaussian surface is described with the PSD [169] given as:

$$W = \left( \frac{cl_x cl_y h^2}{4\pi} \right) \exp \left[ - \left( \frac{K_x cl_x}{2} \right)^2 - \left( \frac{K_y cl_y}{2} \right)^2 \right] \quad (4.1)$$

where  $cl_x$  and  $cl_y$  are the correlation length in x and y directions,  $h$  is the standard deviation of height and  $K^2 = (k_x)^2 + (k_y)^2$  is the wave-vector in the radial direction. These quantities are related to the auto correlation function by,

$$\rho(r) = h^2 \exp \left[ - \left( \frac{x}{cl_x} \right)^2 - \left( \frac{y}{cl_y} \right)^2 \right] \quad (4.2)$$

where  $r$  shows the positions on the surface such that the rough surface structure can optionally generate textures as shown in Fig. 4.1(a).

Based on the previous experimental studies on black silicon, wet-chemical etching, which produces isotropic textures, is the most effective way for obtaining damage-free Si texture among various surface treatments including annealing and oxidation [170]. Isotropic distribution assumption is used in previously reported analysis of black silicon [171,172]. In line with those studies, random roughness surface profile is considered to be homogeneous and isotropic. In this study, isotropic gaussian rough surface approximation was utilized and  $cl_x=cl_y=cl$ . A statistically homogeneous surface means the distribution of height is equally possible at any position within the surface. An isotropic surface is that the correlation function of surface heights is independent of the direction between two corresponding surface points' locations.



The roughness is generated by creating a matrix of uniform random numbers in  $k$  space (wave vector). For this purpose, the random number generator is considered in the script of simulations enable us to generate the Gaussian random number. The high frequency components (short wavelengths) which came from conversion of time functions into waves of different frequencies and are rapidly changing in space, are removed, and the resulting values are transformed back to real space. In this case, a single import object (surface option) is used to define the entire object. The upper surface of this object is defined by a 2D matrix containing the surface height as a function of  $x$  and  $y$ . Then the surface matrix in  $k$ -space fills with uniform random numbers. It is then filtered according to the real roughness data extracted from atomic force microscopy (AFM) images to remove all high frequency components [173] and the actual surface is realized by applying the Fourier transform (FT) on the filtered  $k$ -space. The matrix is transformed back into real space, where the amplitude is corrected. Due to the way the Fourier transform is setup, the roughness will be periodic with period  $x, y$  span. This is convenient when using periodic boundary conditions. The import object is then added to the simulation. For other PSDs such as second order Power-Law and exponential spectrum the spectrum density function is given by Eq. (4.3) and (4.5) respectively. For Power-Law PSD is given by

$$w = \left( \frac{cl_x cl_y h^2}{4\pi} \right) \left\{ 1 + \frac{\Gamma^2(N_p - 1/2)}{\Gamma^2(N_p)} \left[ - \left( \frac{K_x cl_x}{2} \right)^2 - \left( \frac{K_y cl_y}{2} \right)^2 \right] \right\}^{-N_p} \quad (4.3)$$

where  $\Gamma$  is the Gamma function,  $N_p$  is the order and the auto-correlation function for Power-Law spectrum comes from:

$$\rho(r) = h^2 \left\{ 1 + \frac{1}{N_p} \left[ - \left( \frac{x}{cl_x} \right)^2 - \left( \frac{y}{cl_y} \right)^2 \right] \right\}^{-N_p} \quad (4.4)$$

and for Exponential spectrum:

$$w = \left( \frac{cl_x cl_y h^2}{\pi^2} \right) \left\{ 1 + (K_x cl_x)^2 + (K_y cl_y)^2 \right\}^{-1} \quad (4.5)$$

The auto correlation length for Exponential spectrum is as follow:

$$\rho(r) = h^2 \exp\left[-\frac{|x|}{cl_x} - \frac{|y|}{cl_y}\right] \quad (4.6)$$

random textures for mentioned PSDs (Gaussian, Power-Law and exponential) are shown in Fig. 4.2. For this paper the Gaussian type is used since it is commonly observed in black silicon structures with random textures [54].

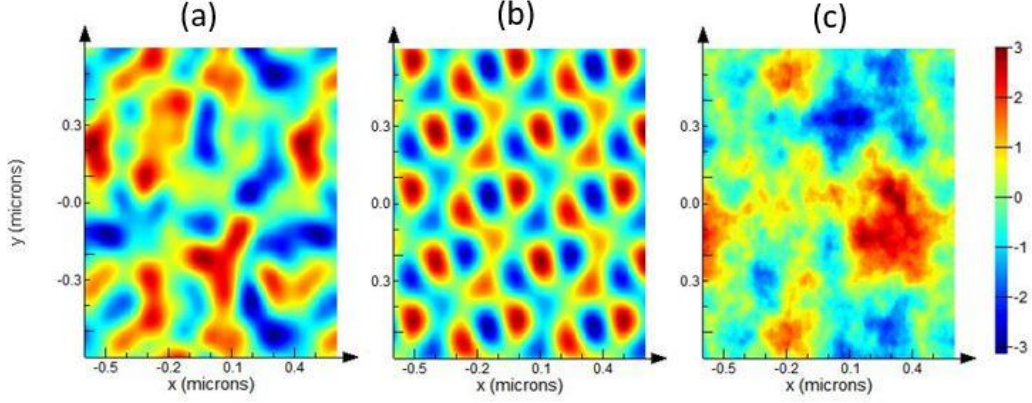


Figure 4. 2: Random roughness texture generated by different PSD functions (a) Gaussian spectrum (b) Power-Law spectrum (c) Exponential spectrum.

Reflection and absorption spectra have been determined in FDTD [140]. Periodic boundary conditions were used in the -x and -y directions, while perfectly matching layers (PML) were used in the lateral directions (-z direction). A broadband plane wave source was employed under normal incidence propagating. Reflection and transmission spectrum are evaluated with defining two monitors above and below the structure respectively. The absorption,  $A$ , is then calculated from reflection,  $R$ , and transmission,  $T$ , as  $A = I - R - T$ , in broadband spectrum. Field distributions over the geometry are also recorded in x-z plane to study the absorption spectra.

#### 4.1.2. Optical Properties

Optical properties of the semiconductors can be modeled by Drude-Lorentz formalism, which is shown in Eq. (4.7),

$$\varepsilon(\omega) = \varepsilon_{\infty} - \frac{\omega_p^2}{\omega^2 + i\gamma\omega} + \sum_{j=1}^m \frac{f_j}{\omega_j^2 - \omega^2 - i\Gamma_j\omega} \quad (4.7)$$

and can be used to characterize dielectric function from spectral measurements [174]. First term in Eq. (4.7),  $\epsilon_\infty$ , is the high frequency permittivity which stands for the contributions from high-frequency electronic transitions. Second term (Drude formalism) is the expression for free electron contribution to the frequency dependent permittivity where  $W_p$  is the plasma frequency and  $\nu$  is the relaxation frequency. Expressions for  $W_p$  and  $\nu$  are given in Eq. (4.8) and (4.9) respectively as,

$$W_p = \sqrt{\frac{4\pi N e^2}{m^*}} \quad (4.8)$$

$$\nu = \frac{e}{\mu_c m^*} \quad (4.9)$$

where  $N$  is the carrier concentration,  $e$  is the electron mass and  $m^*$  is the effective mass in Eq. (4.8) and  $\mu_c$  is the mobility in Eq. (4.9). Last term in Eq. (4.7), Lorentz formalism, stands for the contributions to permittivity coming from lattice vibrations and interband transitions of bond electrons. In Lorentz formalism,  $f_j$  stands for oscillator strength,  $w_j$  for resonance frequency and  $\Gamma_j$  for damping factor.

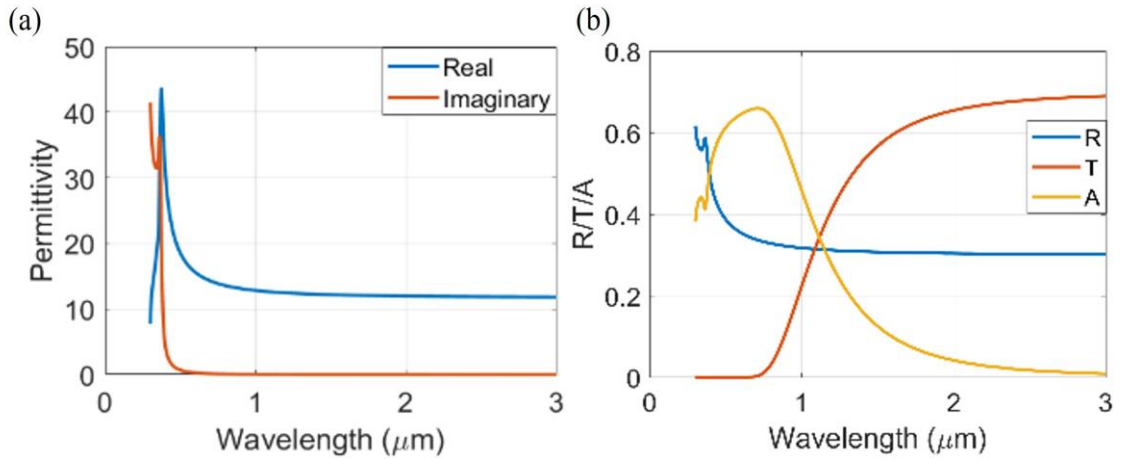


Figure 4. 3: a) Real and imaginary part of the permittivity of the undoped silicon retrieved from [56]. b) Reflectance, transmittance and absorbance of Si film of finite thickness.

Drude formalism is sufficient to model the optical properties of Si for wavelengths longer than 3 μm, where optical properties are dominated by electron plasma of the material. However, to model the properties in wavelengths which are below bandgap energy of the Si, especially in visible spectrum, Lorentz term should be included to

address the interband transitions. In Fig. 4.3(a) permittivity of the Si, retrieved from [175] is demonstrated and reflectance, transmittance and absorptance of Si film of finite thickness is shown in Fig. 4.3(b). As seen from Fig. 4.3(a), real part of the permittivity of the Si is almost constant after 1  $\mu\text{m}$ . However, it has distinct peak around 0.5  $\mu\text{m}$  with finite imaginary part, due to effects of bounded electrons, which give rise to below bandgap absorption as shown in Fig. 4.3(b). Therefore, Drude-Lorentz formalism is required to model the optical properties in 0.3 – 3  $\mu\text{m}$  spectrum interval.

To obtain a Drude-Lorentz model for optical properties of Si, we fit Eq. (4.7) to permittivity data given in Fig. 4.3(a) and obtained the  $\epsilon_\infty$ ,  $W_p$ ,  $\nu$  in Drude term and other Lorentz parameters. We set the number of Lorentz oscillators to 6. Fitting parameters are given in Table 4.1 and reference and fitted permittivity, as well as the spectral reflectance values are compared in Fig. 4.3. Reflectance is obtained by Fresnel equation given in Eq. (4.10).

$$R(w) = \left| \frac{\sqrt{\epsilon(w)} - 1}{\sqrt{\epsilon(w)} + 1} \right|^2 \quad (4.10)$$

Table 4. 1: List of parameters and their values for fitting Drude-Lorentz formalism given in Eq. (3) to optical properties of Si given in [174].

Parameter	Value
$\epsilon_\infty$	5 [F/m]
$W_p$	0.5006 [eV]
$\nu$	$7.33 \cdot 10^{-7}$ [eV]
$f = [f_1:f_6]$	[1.33, 0.18, 1.61, 1.49, 1.53] [eV <sup>2</sup> ]
$w = [W_1:W_6]$	[4.50, 3.40, 3.53, 3.82, 4.50, 4.1] [eV]
$\Gamma = [\Gamma_1: \Gamma_6]$	[ $2.73 \cdot 10^{-5}$ , 0.0025, 0.0874, $2.36 \cdot 10^{-5}$ , 0.064] [eV]

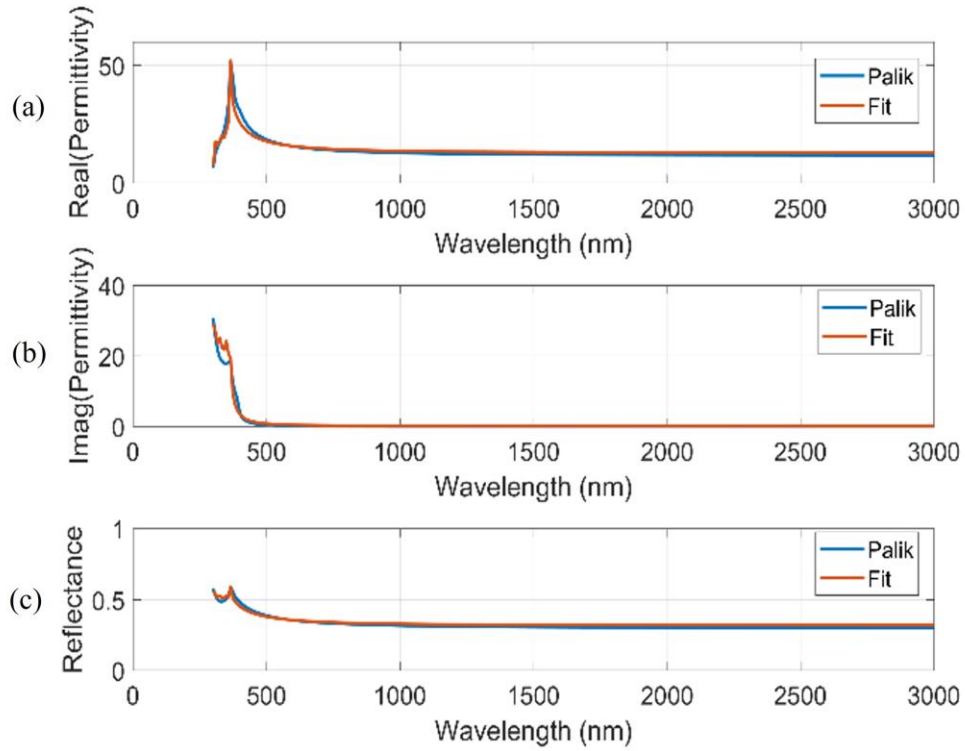


Figure 4. 4: a-b-c) Comparison of real and imaginary part of the permittivity given in [175] and fit values for undoped silicon, and reflectance obtained from it and the fit.

As shown in Fig. 4.4, reference optical properties and obtained properties by fitting agrees well and similar reflectance is obtained over the spectrum of interest. From the Drude-Lorentz equation obtained for pure Si, optical properties of doped silicon for various doping concentrations is obtained.

Doping may significantly alter the optical properties depending on the doping concentration. Optical properties are linked to doping level by carrier concentration in the material. As shown in Eq. (4.8), carrier concentration has proportional relationship with the plasma frequency. In addition, it is also linked to mobility. Both plasma frequency and mobility are in the Drude part of the model, therefore, by modifying the Drude term in Eq. (4.7), permittivity for doped Si is obtained. During the calculations, we assumed constant effective mass for various doping levels. Although we considered n-type doping in analysis, given equations are valid and can be used with corresponding mobility values experimentally reported in [145] and effective mass for -p type doping.

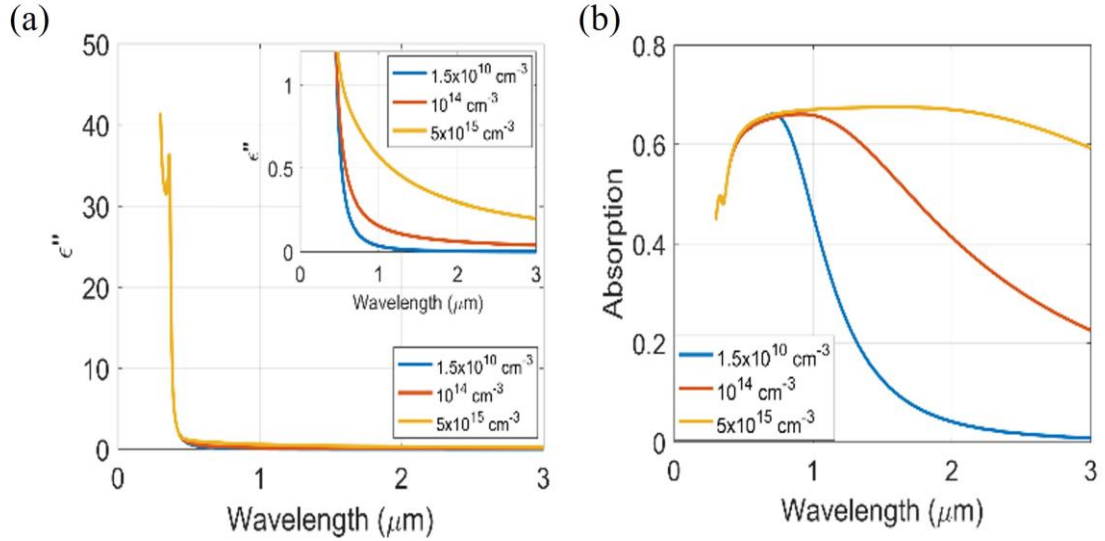


Figure 4. 5: a-b) Imaginary part of the permittivity of Si with doping concentrations of  $1.5 \times 10^{10}$ ,  $10^{14}$ ,  $5 \times 10^{15} \text{ cm}^{-3}$ . c) Absorptivity of silicon with carrier concentrations of  $1.5 \times 10^{10}$ ,  $10^{14}$ ,  $5 \times 10^{15} \text{ cm}^{-3}$ .

Effect of carrier concentration on plasma frequency is evaluated as given in Eq. (4.8). To include the effect of carrier concentration on mobility, experimental values reported in [145], for mobility with respect to carrier concentration, are used in the calculations. We assumed the initial carrier concentration of Si is approximately  $1.5 \times 10^{10} \text{ cm}^{-3}$  and obtained optical properties for n-type doping with different carrier concentrations. In Fig. 4.5, imaginary part of the permittivity of Si with n-type doping concentrations of  $10^{14}$ ,  $5 \times 10^{15} \text{ cm}^{-3}$ .

With the increasing carrier concentration, considerable increase in imaginary part occurs, as shown in Fig. 4.5(a), therefore loss in the material increases. Increased loss in the material results in elevated absorptance/emittance even in the bulk form. As shown, imaginary part of the permittivity is not changed significantly around 3  $\mu\text{m}$  and shorter wavelengths with carrier concentration of  $10^{14} \text{ cm}^{-3}$ . In Fig. 4.5(b), spectral absorptance of Si with the selected doping concentration is demonstrated. As seen, absorptance in broadband spectrum is significantly improved when carrier concentration is increased from  $10^{14}$  to  $5 \times 10^{15} \text{ cm}^{-3}$ . These findings show that even low doping concentrations, give rise to elevated absorptance/emittance in silicon. When combined with surface

roughness/patterns, absorption is further improved by increased coupling with the incident waves and the structure. Absorption of textured structures,  $A(\lambda)$ , are obtained by

$$A(\lambda) = \oint_S (|E(\lambda)|^2 \times \sigma(\lambda)) \cdot ds \quad (4.11)$$

where  $|E(\lambda)|^2$  is the electric field intensity in the geometry and  $\sigma(\lambda)$  is the optical conductivity and dependent on the complex part of the dielectric permittivity,  $\varepsilon = \varepsilon' + i\varepsilon''$ , as

$$\sigma(\lambda) = 2 \times \pi \times f \times \varepsilon''(\lambda) \quad (4.12)$$

## 4.2 Results & Discussions

First, random textures with varying  $l$  and  $h$  are formed with  $p = 4 \mu\text{m}$  for which geometries are depicted in Fig. 4.6 and spectral absorption of those geometries are shown in Fig. 4.7(a). Doping concentration of silicon is fixed to  $10^{14} \text{ cm}^{-3}$ , for which calculation of the corresponding optical properties are described in section 4.1.3. As seen in Fig. 7(a), for doping concentration of  $10^{14} \text{ cm}^{-3}$  near unity absorption is observed in  $0.3 - 1 \mu\text{m}$  spectrum interval for varying correlation lengths and RMS heights when  $p = 4 \mu\text{m}$ . However, high absorptance is decreased to 30 % at longer wavelengths and approach to absorption of smooth film. Such difference over the spectra is attributed to dispersion in optical conductivity where  $\sigma(\lambda=1 \mu\text{m}) \approx 10^{14}$  and  $\sigma(\lambda=2 \mu\text{m}) \approx 10^{13}$ .  $|E(\lambda=0.5 \mu\text{m})|^2$  distributions over the film and texture with  $l=0.2 \mu\text{m}$ ,  $h=0.6 \mu\text{m}$ , geometry depicted in Fig. 4.6(a), are shown in Fig. 4.7(b) and 4.7(c) respectively. As shown in Fig. 4.7(b), uniform distribution of the fields inside the Si is observed when the surface is smooth. Unreflected fields penetrate to the silicon and physical phenomena at the interface can be explained by Fresnel reflections. However, in the case of textured surface, high field enhancements localized near the edges of the individual pyramid-like textures, are observed as shown in Fig. 4.7(c), which are called as side modes throughout the manuscript. As seen, those side modes give rise to higher fields inside the Si spikes, thus lead to elevated absorption. Similar side modes are also observed at different wavelengths in  $0.3-3 \mu\text{m}$  interval. It indicates that such side modes occur in broadband spectrum when

the Si surface is textured and responsible from broadband absorption enhancement. To explore the effect of roughness dimensions on the absorption, field distributions are also analyzed for the geometry depicted in Fig. 4.6(b), which has less peaks and dips in the geometry due to the increased correlation length. In other words, texture in Fig. 4.6(a) has more spikes with small widths, whereas texture in Fig. 4.6(b) has less spikes with wider widths.

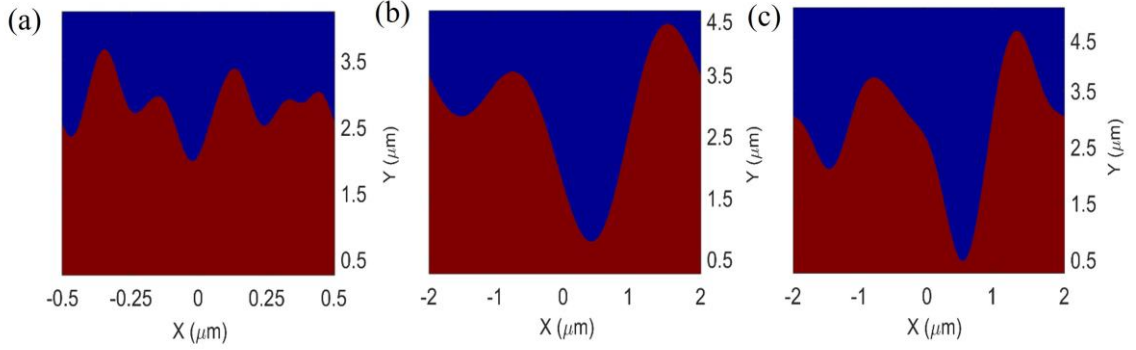


Figure 4. 6: a) An example random texture generated by setting  $l=0.1 \mu\text{m}$ ,  $h_{\text{rms}}=0.3 \mu\text{m}$ ,  $p = 1 \mu\text{m}$ . b) An example random texture generated by setting  $l=1.1 \mu\text{m}$ ,  $h_{\text{rms}}=0.8 \mu\text{m}$ ,  $p = 4 \mu\text{m}$ . c) An example random texture generated by setting  $l=0.6 \mu\text{m}$ ,  $h_{\text{rms}}=0.8 \mu\text{m}$ ,  $p = 4 \mu\text{m}$ .

Although no significant difference between textures with varying  $l$  and  $h$  are observed at longer wavelengths, slight decrease in absorption in visible spectrum is observed for increased  $l$ . To analyze,  $|E(\lambda=0.5 \mu\text{m})|^2$  distribution for the texture with  $l=1.1 \mu\text{m}$ ,  $h=0.8 \mu\text{m}$  is shown in Fig. 4.7(d). As seen in Fig. 4.7(d), side modes also occur in this texture with slightly reduced field intensities inside the spikes. It shows that field enhancement by the side modes are dependent on the width of the individual pyramids. Increased widths lead to reduced intensity, thus resulting in decreased absorption. Effect of doping concentration on the spectral distribution and corresponding spatial absorption profiles for doping concentrations of  $10^{14}$  and  $5 \times 10^{15} \text{ cm}^{-3}$  are also shown in Fig. 4.8. As shown in Fig. 4.8(a), spectral absorption is significantly enhanced with increased doping concentration especially at longer wavelengths.  $|E(\lambda)|^2 x \sigma(\lambda)$  distributions given in Fig. 4.8(b) and 4.8(c) for  $N=10^{14}$  and  $5 \times 10^{15} \text{ cm}^{-3}$  also shows that spatial distribution profile inside the texture is not significantly altered by  $N$ .



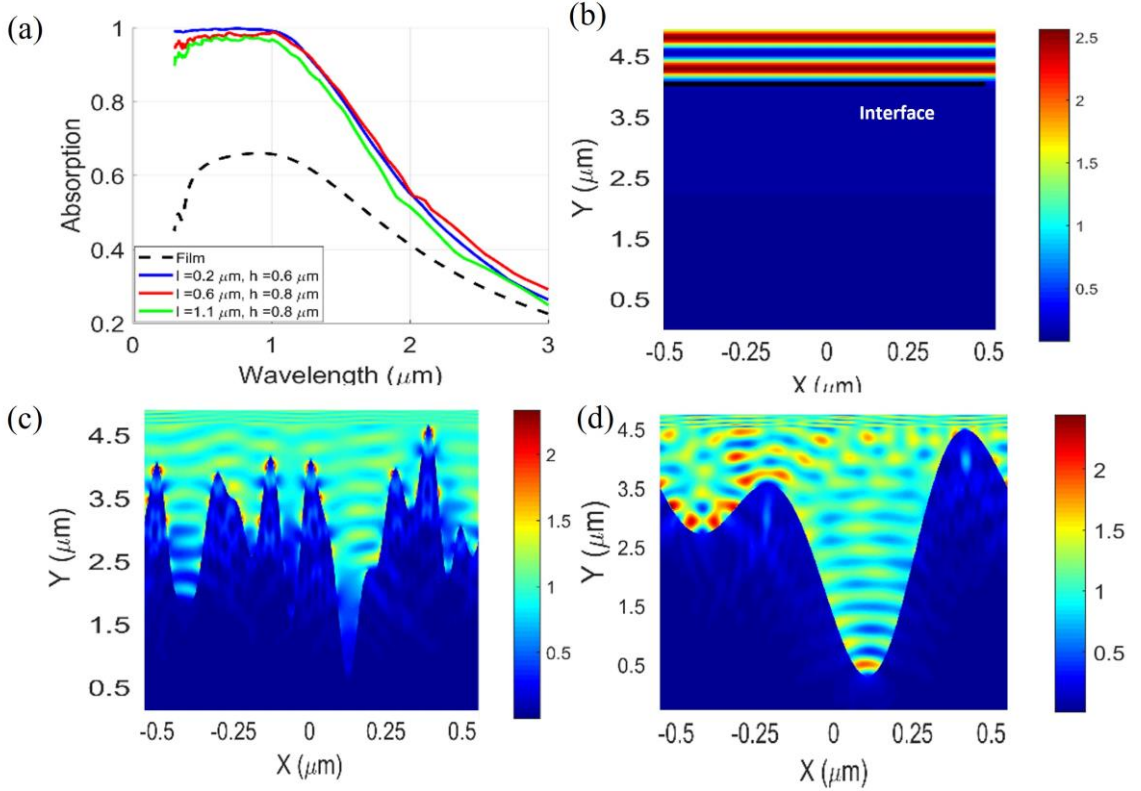


Figure 4. 7: a) Comparison of spectral absorption of untextured (film) and textures silicon with varying  $l$  and  $h_{\text{rms}}$ . b)  $|E(\lambda)|^2$  distribution of untextured Si. c)  $|E(\lambda)|^2$  distribution of textured silicon with  $l=0.1 \mu\text{m}$  and  $h_{\text{rms}}=0.3 \mu\text{m}$ . d)  $|E(\lambda=0.5 \mu\text{m})|^2$  distribution of the texture with  $l=1.1 \mu\text{m}$ ,  $h_{\text{rms}}=0.8 \mu\text{m}$  at  $\lambda=0.5 \mu\text{m}$ .

However, differently from  $N=10^{14} \text{ cm}^{-3}$  case, fields absorbed more on the upper segment of the texture due to increased attenuation with increased  $\epsilon''(\lambda)$ , therefore  $\sigma(\lambda)$ , when  $N$  is set to  $5 \times 10^{15} \text{ cm}^{-3}$ . Finally, spectral absorption of a random texture is compared to deterministic textures with varying periodicities in Fig. 4.8(d).  $|E(\lambda=0.5 \mu\text{m})|^2$  is also depicted in Fig. 4.8(e).

Results depicted in Fig. 4.8(a) shows that spectral absorption of the random textures are very similar to previously reported experimental results [117,118,166]. Also, absorption of deterministic textures is similar to random textures' and are not very sensitive to periodicity in 0.3-3  $\mu\text{m}$  spectrum, except the visible spectrum. Similar change in the visible spectra is also reported for random textures and attributed to reduced field intensity when texture widths are increased. In addition, field distribution for the deterministic texture with  $p=1 \mu\text{m}$  shown in Fig. 4.8(e) shows that side modes are also supported in deterministic textures. such similarity in absorption spectrum and field

distributions allow us to use deterministic textures to understand underlying mechanisms in textured silicon. For analysis, deterministic textures with varying dimensions in broadband spectrum are analyzed.

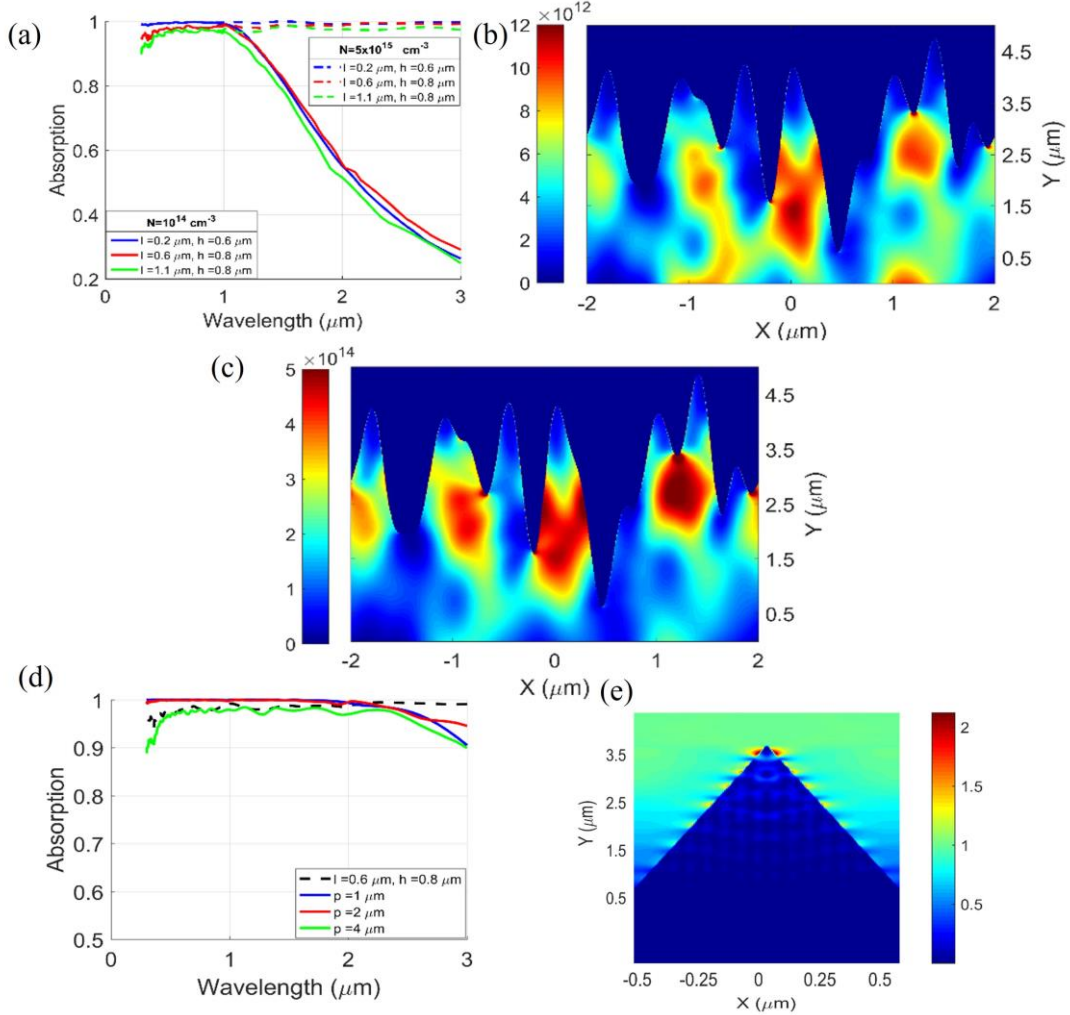


Figure 4. 8: a) Spectral absorptions of random textures for  $N=10^{14}$  and  $5 \times 10^{15} \text{ cm}^{-3}$ . b-c) Spatial absorption profiles for  $N=10^{14}$  and  $5 \times 10^{15} \text{ cm}^{-3}$  at  $\lambda=0.5 \text{ μm}$ . d) Absorption of a random texture and deterministic texture with varying  $p$  for  $N=5 \times 10^{15} \text{ cm}^{-3}$ . e)  $|E(\lambda=0.5 \text{ μm})|^2$  distribution for the deterministic texture with  $p=1 \text{ μm}$ .

In the light of reported results until this point, it is found out that high absorption in broadband spectrum stem from local field enhancements which occur near the edges of the features. Both in random and periodic textures, such side modes are observed. Analysis reveals that field intensity of the side modes are dependent on the width of the individual spikes and are reduced with increased width. This led to reduction in the

absorptance percentage of the periodic textures compared to random textures due to the presence of a single structure with larger width. Source of the observed variations is discussed in the following parts together with the driving mechanisms for the fields. Spatial absorption profiles inside the silicon are found to be insensitive to doping concentration. Finally, it is shown that deterministic textures exhibit similar absorption characteristics compared to random textures.

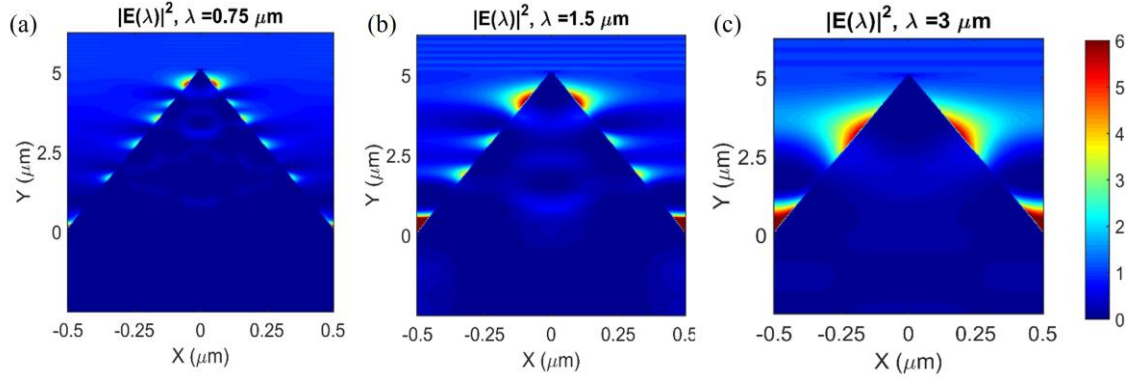


Figure 4. 9: a-b-c)  $|E(\lambda)|^2$  at wavelengths of 0.75, 1.5 and 3  $\mu\text{m}$  for the pyramid dimensions of  $p = 1 \mu\text{m}$ ,  $h = 3 \mu\text{m}$  and carrier concentration of  $10^{14} \text{cm}^{-3}$

To study the underlying mechanism that give rise to side modes, further analysis is carried out with deterministic textures. Deterministic textures are chosen to avoid interference effects in random textures therefore, to be able to characterize the side modes occurring in individual features.  $|E(\lambda)|^2$  and  $|E(\lambda)|^2 \times \sigma(\lambda)$  distributions over the deterministic textures are considered for the analysis.

In Fig. 4.9,  $|E(\lambda)|^2$  for  $\lambda = 0.75 \mu\text{m}$ ,  $\lambda = 1.5 \mu\text{m}$  and  $\lambda = 3 \mu\text{m}$  is demonstrated.  $p$  and  $h$  of the pyramid are set to 1  $\mu\text{m}$  and 3  $\mu\text{m}$  respectively and  $N$  is set to  $10^{14} \text{cm}^{-3}$ . As seen, distinct local field enhancements on the edges of the pyramid are observed. At each wavelength, highest field intensities are obtained near the top of the pyramid. However, number of local field enhancements on the edges of pyramid differ for each wavelength. Those distinctive regions also exist inside the pyramid, as shown in  $|E(\lambda)|^2 \times \sigma(\lambda)$  distributions depicted in Fig. 4.10 for selected wavelengths.

As shown in Fig. 4.10, highest absorption inside the pyramid occurs at the region where side mode with highest intensity penetrates the structure. Field distribution due to

this mode, thus the absorption, inside the pyramid is similar for the selected wavelengths. Results depicted in Fig. 4.9 and 4.10 shows that these textures support resonance modes at different wavelength and resonance conditions are satisfied throughout the geometry multiple times. To analyze, previously reported study regarding to resonance mechanisms in a trapezoid geometry is considered.

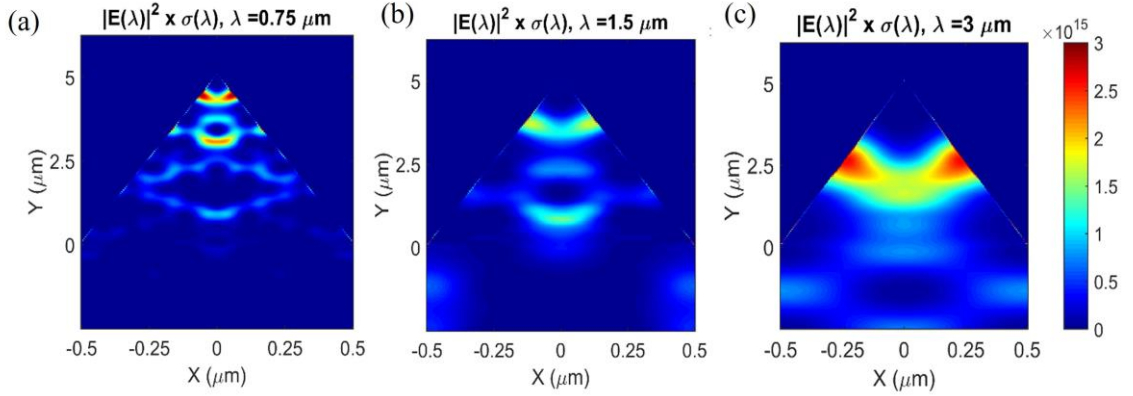


Figure 4. 10: a-b-c)  $|E(\lambda)|^2 \times \sigma(\lambda)$  at wavelengths of 0.75, 1.5 and 3  $\mu\text{m}$  for the pyramid dimensions of  $p = 1 \mu\text{m}$ ,  $h = 3 \mu\text{m}$  and carrier concentration of  $10^{14} \text{cm}^{-3}$ .

In the literature, such position dependent local field enhancements are reported for trapezoidal metal-insulator-metal (MIM) ultra-thin broadband resonators [176]. In [176], it is shown that strong and broadband field enhancement is achieved by exciting multiple resonance modes in different regions of the trapezoidal structure. Similarly, silicon pyramid can support multiple resonance modes due to its trapezoidal geometry and give rise to high field enhancements inside which are absorbed due to the broadband loss introduced in the silicon with doping. Those resonance modes also give rise to strong fields in the silicon air interface on the sides of the pyramid. Resonance condition for different wavelengths is dependent on  $-Z$  direction. Position of the resonance mode with the highest intensity shifts towards to the bottom of the pyramid for increasing wavelength. It indicates that higher pyramid width is required to achieve increased coupling with the structure for longer wavelengths. It is also observed that those modes are repeated throughout the pyramid in  $-Z$  direction. To estimate the resonance condition in the pyramid, an effective wavelength method derived for optical antennas is used here.

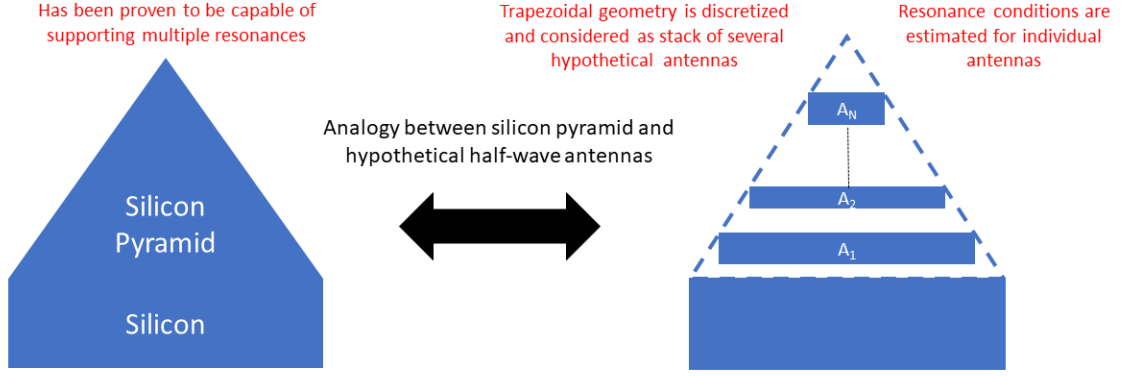


Figure 4.11: Scheme for analogy between silicon pyramid and stacked half-wave antennas

It is known that coupling condition for RF and microwave antennas are strongly correlated with the length of the antenna, e.g. it is  $L = (1/2)\lambda$  [177] for half-wave antennas. Such relationship fails in optical frequencies due to the penetration of the incident wave into the structure and interaction of it with the electron oscillations, whereas structures are nearly perfect conductors in microwave and RF applications, thus penetration does not occur. By considering this difference, an effective wavelength,  $\lambda_{eff}$ , calculation formula is derived in [167] which yields an  $\lambda_{eff}$  inside the antenna that can be used to tune the  $L$ . By utilizing this theory, required width for the resonance at a specific wavelength inside the silicon pyramid is estimated. To apply such analysis, pyramidal geometry is treated as a combination of several half-wave antennas which resonate at different wavelengths. Scheme for such representation is depicted in Fig. 4.11.  $\lambda_{eff}$  calculation is described in detail in [178] and final formula for  $\lambda_{eff}$  is given in Eq. (4.13),

$$\lambda_{Eff} = \frac{\lambda}{\sqrt{\epsilon_s}} \sqrt{\frac{4\pi^2 \epsilon_s \left(\frac{R^2}{\lambda^2}\right) \tilde{z}(\lambda)^2}{1 + 4\pi^2 \epsilon_s \left(\frac{R^2}{\lambda^2}\right) \tilde{z}(\lambda)^2}} \quad (4.13)$$

where  $\lambda$  is the incident wavelength,  $\epsilon_s$  is the permittivity of the incident medium,  $R$  is the thickness of the antenna and  $\tilde{z}$  is an intermediate variable expressed in [167]. Based on this formula,  $L$  for the resonance to occur is obtained as  $\lambda_{eff}/2$  for a half-wave antenna. To create an analogy between half-wave antennas and silicon pyramids,  $L$  is treated as width of the pyramid where a side mode occurs. Therefore, side modes are attributed to half-wave antennas and when stacked together in trapezoidal fashion, multiple resonance modes at different wavelengths are supported.

Effective wavelength calculation with Eq. (4.13) is carried out for the selected wavelengths,  $\lambda_1 = 0.5 \mu\text{m}$ ,  $\lambda_2 = 1.5 \mu\text{m}$  and  $\lambda_3 = 3 \mu\text{m}$ . Hypothetical half-wave antenna with dimensions is schematized on the pyramid and field distribution at  $\lambda_3$  is shown in Fig. 4.12(a). In this case, effective wavelength of  $0.7 \mu\text{m}$  is obtained, with  $R = 0.13 \mu\text{m}$ , from Eq. (13), thus  $L = 0.35 \mu\text{m}$ , which is equal to the width of the pyramid at the location where resonance mode is occurred as shown in Fig. 4.9(c). Smaller effective wavelengths are achieved for wavelengths of  $\lambda_1$  and  $\lambda_2$ , for which field distributions are also shown in Fig. 4.9. To analyze the dependency of  $L$  on  $R$ ,  $L$  values are calculated for varying  $R$  values. To satisfy the  $R \ll \lambda$  requirement given in [167] for Eq. (4.13) to be valid,  $R$  values between  $\lambda/20$  and  $\lambda/50$  are considered and maximum errors are demonstrated in Fig. 12(b) for wavelengths of  $\lambda_1$ ,  $\lambda_2$  and  $\lambda_3$ .

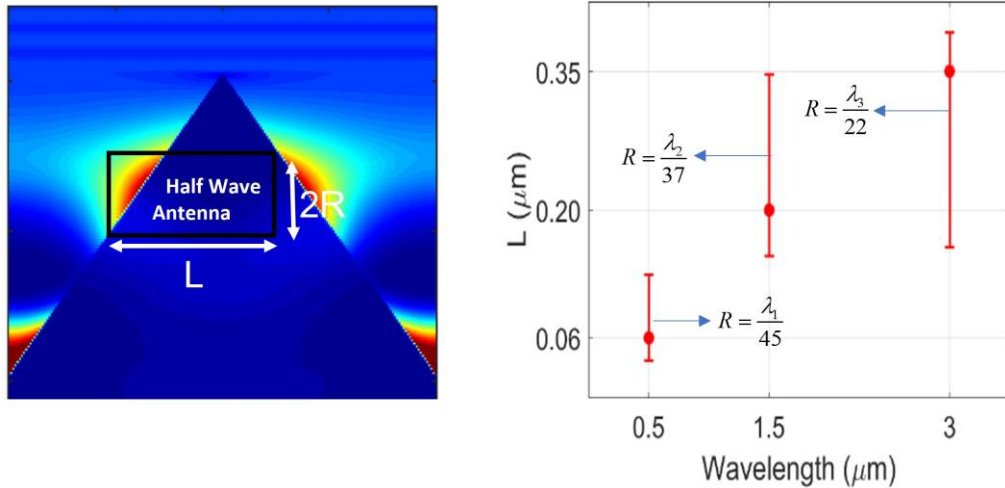


Figure 4. 12: a) Representation of individual half-wave antenna with thickness  $2R$  and length  $L$ , on the pyramid silicon. b) Calculated resonance condition for varying  $R$  values and corresponding  $L$  values. Lower and upper bounds of the error bars stand for  $R = \lambda/50$  and  $\lambda/20$ .  $L = \lambda_{\text{Eff}}/2$  values are obtained at  $R = \lambda_1/45$ ,  $R = \lambda_2/37$  and  $R = \lambda_3/22$  which is equal to the width of the pyramid where first side mode occurs.

As seen from Fig. 4.12(b), maximum errors are  $0.07$ ,  $0.15$  and  $0.18 \mu\text{m}$  which corresponds to  $\lambda_1/7$ ,  $\lambda_2/10$  and  $\lambda_3/15$  for wavelengths of  $\lambda_1$ ,  $\lambda_2$  and  $\lambda_3$ . Estimation accuracy is increased with higher ' $R$ ' at longer wavelengths which indicates that fields are less confined in the geometry for longer wavelengths. Such variations in confinement also shown in Fig. 4.9. Calculated effective wavelengths for the given dimensions of ' $L$ ' and ' $R$ ' shows that absorption occurs in very small dimensions compared to overall size. This

also explains the high absorption at different periodicities which controls the width of the pyramids. Since sufficient width for effective wavelength matching condition is satisfied for  $p = 1, 2$  and  $4 \mu\text{m}$ , high fields, thus absorption, inside the pyramids are achieved. As shown in the field distribution results, these absorptance modes are repeated throughout the geometry. This repetition is attributed to similar resonance condition, which occurs due to the scaling of effective wavelength obtained from Eq. (4.13). In other words, effective wavelength matching conditions are satisfied when the width of the pyramid is extended. Similar behavior is also observed for increased pyramid heights. Higher heights only lead to increased number of side modes, which do not alter the absorptance in broadband. This also indicates that, matching condition is highly dependent on width of the pyramid. As a next step, effects of periodicity of the pyramids, therefore the texture widths, on the field distributions and absorption are investigated.

$|E(\lambda)|^2$  distributions depicted in Fig. 4.13(a), (b) and (c) shows that number of side modes at  $3 \mu\text{m}$  is increased with increasing periodicity. These results indicate that coupling condition inside the pyramid is repeated and it is linked to the periodicity, thus the width of the pyramid. However, different trends are observed in the fields inside the pyramid. In Fig. 4.13(d), a single distinctive high absorption zone is observed inside the pyramid which is linked to side mode shown in Fig. 4.13(a). The highest absorptance zone is shifted towards to the bottom of the pyramid and exhibits a different kind of  $|E(\lambda)|^2 \times \sigma(\lambda)$  distribution when  $p$  is increased to  $2 \mu\text{m}$ .



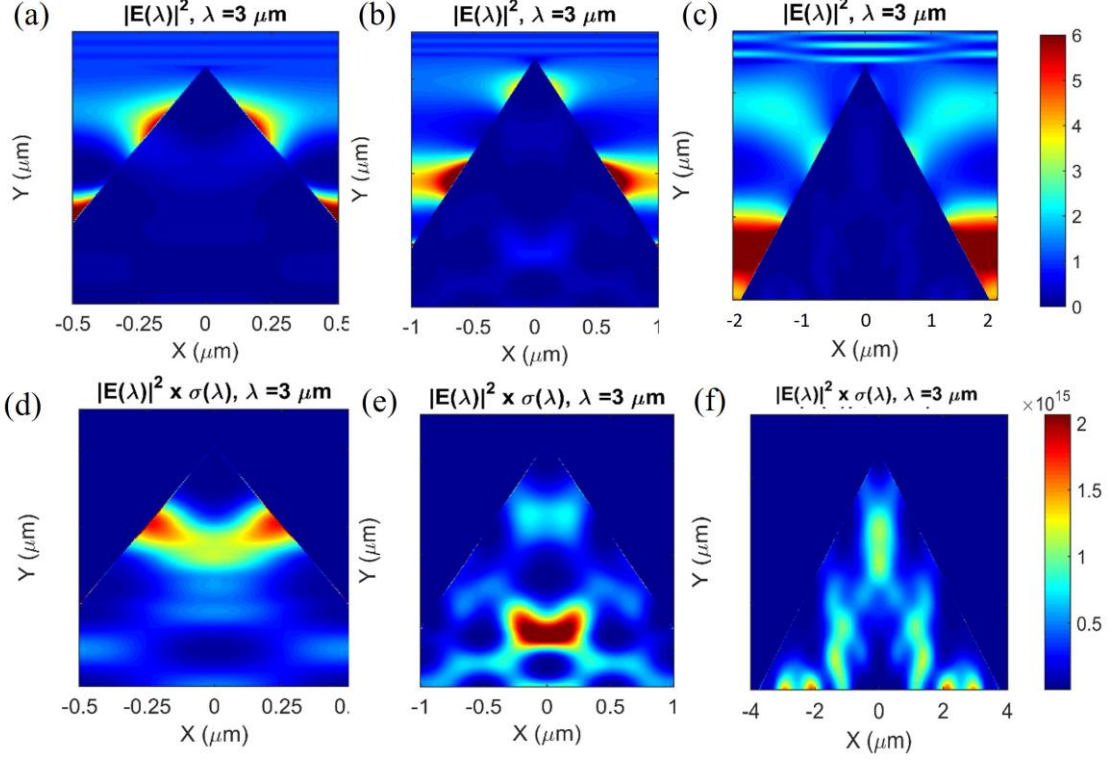


Figure 4. 13: a-b-c)  $|E(\lambda)|^2$  distributions at  $\lambda = 3 \mu\text{m}$  wavelength for  $p = 1 \mu\text{m}, 2 \mu\text{m}$  and  $4 \mu\text{m}$  respectively. d-e-f)  $|E(\lambda)|^2 \times \sigma(\lambda)$  distributions at  $\lambda = 3 \mu\text{m}$  wavelength for  $p = 1 \mu\text{m}, 2 \mu\text{m}$  and  $4 \mu\text{m}$  respectively.

The highest absorptance zone in Fig. 4.13(d) is occurred due to the side modes and a continuous trend between the fields inside and outside of the pyramid is observed. However, a continuous trend is not observed between the highest  $|E(\lambda)|^2 \times \sigma(\lambda)$  region inside the pyramid and side modes shown in Fig. 4.13(e) and 4.13(b) respectively.

A different behavior from these is observed when  $p = 4 \mu\text{m}$ . As seen in Fig. 4.13(f), multiple high  $|E(\lambda)|^2 \times \sigma(\lambda)$  zones are occurred, and they are extended in  $-Z$  direction like propagating modes.  $|E(\lambda)|^2 \times \sigma(\lambda)$  in Fig. 4.13(e) and 4.13(f) indicates that absorptance enhancement inside the pyramids in these geometries does not only stem from effective wavelength matching condition. Although resonance conditions in the pyramid is satisfied as shown in Fig. 4.13(b) and 4.13(c), another phenomenon occurs in these geometries which induces fields that interfere with the resonances. Therefore, distinctive  $|E(\lambda)|^2 \times \sigma(\lambda)$  region in Fig. 4.13(e) is attributed to the interference of the fields induced by multiple electromagnetic phenomenas occurring in the geometry. Finally, results depicted in Fig. 4.13(f) shows that field enhancement in the geometry is dominated by



this second electromagnetic phenomenon which give rise to field enhancements extended in -Z direction and suppresses the fields induced by effective wavelength matching.

It is observed that these pyramids resemble the waveguide geometries that are composed of a high index core surrounded by a low index cladding which supports certain TM modes. In this configuration, silicon acts as high index core and air is the low index cladding material as depicted in Fig. 4.14(a). Due to the tapered geometry, broadband spectrum of wavelengths is supported throughout the geometry and response is analogous to tapered fibers [179]. In tapered fibers, modes with longer wavelengths start to cut-off as the width of the fiber shrinks. In the textured silicon geometries, modes with longer wavelengths start to occur as width of the pyramid increases.

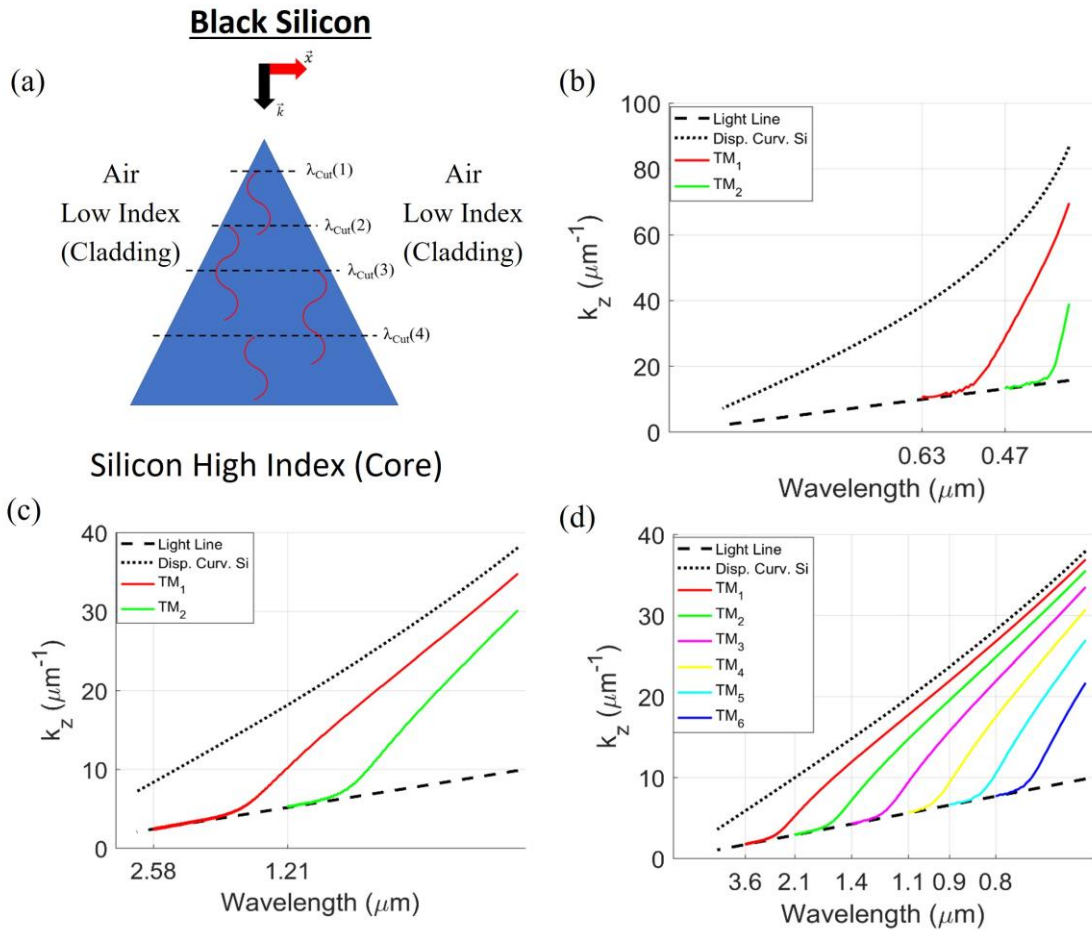


Figure 4. 14: a) Scheme for the black silicon as a waveguide problem composed of high index (core) and low index (cladding). b-c-d) Dispersion diagrams for  $d = 0.06, 0.2$  and  $0.35 \mu\text{m}$  at which effective wavelength matching condition is satisfied for wavelengths of  $0.5, 1.5$  and  $3 \mu\text{m}$  wavelengths.

Therefore, two problems are analogous and similar analysis is adapted based on the reciprocity of the Maxwell's equations. Assuming tapered geometry is composed of rectangular segments for which supported TM modes' cut-off wavelengths are estimated by,

$$k_{cut} = \frac{m\pi}{d\sqrt{1-\frac{\mu_1\varepsilon_1}{\mu_0\varepsilon_0}}} \quad (4.14)$$

and dispersion diagrams are obtained by the following expressions:

$$\left\{ \begin{array}{l} \tan(k_x d) \\ -\cot(k_x d) \end{array} \right\} = \sqrt{\frac{w^2\mu_0(\varepsilon_1-\varepsilon_0)d^2}{(k_x d)^2} - 1} \quad (4.15)$$

$$k_z = \sqrt{w^2\mu_0\varepsilon_1 - k_x^2} \quad (4.16)$$

With the aid of dispersion diagrams, which modes are supported at certain parts of the tapered geometry is estimated. Based on these formulas, dispersion diagrams for different core widths, which corresponds to width of the silicon pyramid. Diagrams for  $d=0.06 \mu\text{m}$ ,  $d=0.2 \mu\text{m}$  and  $d=0.35 \mu\text{m}$ , at which effective wavelength matching is achieved, are obtained and shown in Fig. 4.14.

As seen in Fig. 4.14(b), 4.14(c) and 4.14(d) respectively, only  $\text{TM}_1$  modes exist with a very small wavevector (near cut-off wavelength), for wavelengths of  $0.5 \mu\text{m}$ ,  $1.5 \mu\text{m}$  and  $3 \mu\text{m}$  when  $d$  is set to  $0.06 \mu\text{m}$ ,  $0.2 \mu\text{m}$  and  $0.35 \mu\text{m}$ . This indicates that fields formed due to the effective wavelength matching in these segments do not strongly interfere with TM modes. Therefore,  $E$  fields smoothly travels throughout the pyramid in -X direction and continuous trends are observed. However, this is only valid for the top side mode.

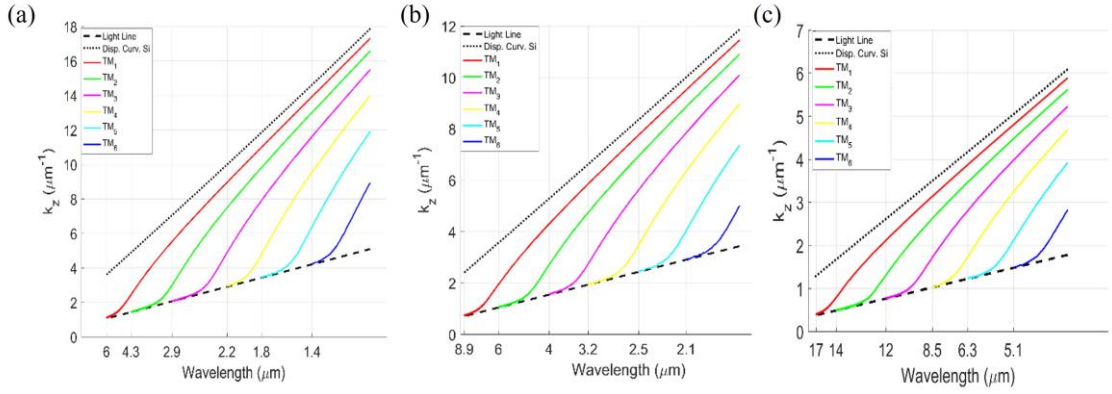


Figure 4. 15: a-b-c) Dispersion diagrams for  $d=0.7, 1$  and  $2 \mu\text{m}$  and supported TM modes with cut-off wavelengths labeled

Although modes that exist when  $d = 0.2 \mu\text{m}$  or  $d=0.35 \mu\text{m}$  do not have high wavevectors at longer wavelengths, it is not the case for shorter wavelengths. As seen in Fig. 4.14(c) and 4.14(d), number of modes and magnitude of the existing modes' wavevectors are increased at shorter wavelengths. This indicates that TM modes at shorter wavelengths start to interfere with fields induced by effective wavelength matching when width is around  $0.2 \mu\text{m}$ . Such interference lead to reduction in absorption in the visible spectrum for the rough surfaces with increased correlation lengths and shown in Fig. 4.7(a). Since width of the individual spikes are increased with increasing correlation lengths, TM modes start to form in the textures and reduction in absorption in shorter wavelengths are observed. To further analyze the effect of texture width,  $d$ , modes in the structures with higher periodicities are analyzed.

As periodicity increased, maximum width of the silicon pyramid is also increased, and multiple effective wavelength matching conditions occur throughout the geometry as shown in Fig. 4.13(b). Increase in maximum possible width also allows the pyramid support other TM modes which have longer cut-off wavelengths. To show this, dispersion diagrams with  $d = 0.7 \mu\text{m}$ ,  $1 \mu\text{m}$  and  $2 \mu\text{m}$  is demonstrated in Fig. 4.15. As shown in Fig. 4.15, with increasing  $d$ , number of TM modes increase and wavevector of the existing modes, e.g.  $\text{TM}_1$ , is increased. Therefore, at wider widths, contributions from TM modes to electric fields are increased. This leads to significant changes in field distributions and reduction in absorption which becomes more dominant at shorter wavelengths. This finding also explains the reduction in absorptance at longer wavelengths in periodic textures compared to deterministic textures, which was attributed

to presence of a single texture with higher width. Due to the stronger interference of the waveguide modes with the fields induced by effective wavelength matching at higher widths, reductions in absorptance spectra of random textures compared to deterministic ones are observed.

Demonstrated dispersion diagrams indicate that waveguide modes are started to be supported at widths larger than 50 nm and their contributions become more distinguishable at larger widths. Their contributions are observed in spatial absorptance profiles depicted in Fig. 4.10 and 4.13(d-f), which shows that these two separate phenomena coexist in broadband spectrum at these geometries. In summary, our analysis regarding to supported TM modes reveal that these modes have significant effect on the field distribution inside the pyramid. It is shown that TM modes becomes dominant in broadband with increased periodicity of the pyramids and compensates the effect fields induced due to the effective wavelength matching throughout the geometry. In other words, TM modes starts to dominate field profile in the geometry at widths around 0.3  $\mu\text{m}$  in broadband and effective wavelength matching is dominant at smaller widths.

## 5. CONCLUSION

Main aim of this thesis is analysis of spectral characteristic of surfaces and surface engineering to enhance the optical properties for selected applications. Using surface textures and controlling its characteristics new methods are proposed to effectively used in spectrally selective applications. With the proposed methods in this thesis, various structure with desired broadband and narrowband features are achieved to be used in desired applications. With explaining underlying mechanism and proposing design and methodology, and reported findings in this thesis, new structure proposed with superior characteristics compared to previously reported ones.

In summary, a spectrally selective absorber surface made of Tungsten using an anisotropic Gaussian rough surface for high-temperature applications is demonstrated. It is shown that the rough surface enhances the absorption spectra both in the visible and near infrared spectral regions. For isotropic random rough surfaces, it is shown that at correlation length higher than 200 nm, a peak started to appear in the absorption curve around the wavelength of 1000 nm. Increasing the RMS height leads to broadening the bandwidth of near-unity absorption for the 1000-1600 nm region. Our investigation shows that using anisotropic random rough surface design yields even more interesting results in terms of the absorption spectrum. Larger than 90% absorption is obtained for the optimized anisotropic random rough surface for the spectral range from 300-1700 nm, suggesting a perfect absorption bandwidth up to 1700 nm in the ultraviolet- visible-near infrared region. These optimized random nanostructures provide multiple resonant modes, which introduce strong optical coupling and result in a broadening of the high absorption spectrum region in the range of 300-1700 nm. The proposed spectrally selective absorber in this study eliminates the need for adding extra layers or nanoparticles to act as spectral selective emitters. Moreover, this technique avoids inserting additional surface thickness by adding coatings of different materials. These findings can be used in tailoring broadband spectrum for different applications in which the surfaces are exposed to high temperatures, such as solar and aerospace applications.

As another spectrally selective structure, multilayer structures using thin film layers with optimized layer thickness is studied. Multilayer structure with broadband spectral selective ability is optimized to be used as a passive radiative cooling. To make it more practical in outer surfaces we also presented a study on layered radiative cooling for aesthetic applications. This approach has been gained by embedding a thin silver bowtie nanoantenna structure between reflector layers and emitter layers in TiO<sub>2</sub>/SiO<sub>2</sub> layered radiative cooling. To insert the color display module, the layers are divided into reflector layers with thin thickness and emitter layers with thick thickness; the color displaying module is added to the top of the reflector layer to alter the emissivity in the visible spectrum. In layer thickness optimization, a new term for maximizing reflection spectrum in solar spectrum along with maximizing the cooling power is added to the cost function to have a maximum reflection in the solar spectrum. Bowtie nanoantenna by enhancing and localizing electric field in the gap between two parts of nanoantenna cause a strong but narrow band absorption in the visible spectrum, which lead to color display of radiative cooling. However, this function happens by the expense of 30% of net cooling power compared to conventional radiative cooling (from 87 to 60 W/m<sup>2</sup>) but still with positive values of cooling power are applicable. The reduced radiative cooling power derives from the additional input solar radiation energy in the visible waveband when adding the color display module.

Moreover, another advantage of our proposed model in addition to the simplicity of the model, is the ability to control the colors by changing the parameters of bowtie nanoantenna such as gap size, length, and width. It is shown that the field enhancement happens in the gap, and strong plasmonic coupling occurs between the two triangular nano prisms at the gap, altering the emissivity spectrum and strong but narrow absorption spectrum creates, which leads to the color generation. In the previous models, the control over coloration was mostly done by increasing the thickness of layers which requires extra materials and increased the cost. Finally, this research provides a new perspective on the development of effective radiative coolers and plasmonic colors. This opens the way for energy-efficient colored surfaces and may be utilized for a variety of applications such as colored buildings, automotive, clothes, or other beautiful products.

Finally, to study the effect and underlying mechanism of surface structure, broadband absorption mechanism of the black silicon is investigated. Field distributions inside the random and deterministic textures show that high field intensities which are confined near the edges of the textures occur. Detailed analysis shows that high coupling in transverse direction occurs and coupling conditions are estimated with effective wavelength matching phenomenon in optical antennas. Further analysis reveals that, TM modes are also supported in the textures and affects the absorption distribution over the geometry. Due to the trapezoidal geometry of the textures, TM modes start to form with increasing width ( $d$ ). It is found out that effective wavelength matching occurs in smaller widths ( $d < 0.3 \mu\text{m}$ ) and are dominant in terms of contribution to absorption. On the other hand, TM modes start to dominate at higher widths ( $d > 0.3 \mu\text{m}$ ) in broadband for which cut-off wavelengths are obtained by waveguide theory. Destructive interference of the fields induced by these two different phenomena lead to slightly reduced spectral absorption. Our findings regarding to driving mechanisms of elevated absorption in black silicon provide a good understanding of those mechanisms which was not discussed in such a detailed manner before.

As a result, in this thesis in order to alter the spectral features (transmission, reflection, and absorption) of light, at the nanoscale, light-matter interactions done by engineering the surface of structure or using nanostructures. Therefore, designing the Micro-nano structures for broadband and direction-selective emission is one of primary goals of this study. This purpose is achieved by providing design methodologies for spectral selective emission surfaces with various applications, such as spectrally selective absorber, colored radiative cooling and absorption mechanism of black silicon, which in all of them it is required to do surface engineering to do spectrally selective in both broadband and narrowband. Altogether, various problems are thoroughly investigated by a well-defined methodology and the outcomes are well described. Although particular problems requiring selectively electromagnetic spectrum are presented in this thesis, but the approaches described in this thesis may be applied to a variety of problems in related fields and may stimulate future research.

## 6. FUTURE WORK

The following headlines are proposed for furthering work based on the research output of this thesis:

- Meta materials as an effective structure can be used on optical surfaces as a spectrally selective structure. Combining multilayer structure with metamaterials by altering optical characteristics can be good topic to be used in various applications. Meta surfaces have a wide range of potential applications in electromagnetics including controllable “smart” surfaces, novel wave-guiding structures, angular-independent surfaces, absorbers and biomedical devices.
- VO<sub>2</sub> has attracted much attention for use as a smart coating in various electro-optic applications due its insulator to metal transition (IMT) at 68 °C (T<sub>c</sub>). VO<sub>2</sub> coatings reflect infrared radiation above T<sub>c</sub>, while transmitting almost the entire optical spectra below T<sub>c</sub>. Due to this phenomena, VO<sub>2</sub> coatings have attracted interest especially for energy efficient smart windows, opto-electronic switching devices, and sensing applications. Based on the experiment results it was observed that surface of VO<sub>2</sub> can be modeled with rough surfaces. The reflectance spectrum of VO<sub>2</sub> and underlying mechanism of optical behavior of it can be an interesting topic to study.
- The ability to selectively and flexibly interact with light has applications in a broad variety of technologies. Due to the interesting properties of nanoparticles recently have seen a notable rise in the amount of research done on nanoparticles. We believe nanoparticles with interesting effect in optical properties can be a good candidate to be used as spectrally selective filters. Material, size, concentration and morphology of nanoparticles can be used as a controlling factor in designing spectral selective structures.
- Control over bandwidth of narrowband\broadband spectrum is another interesting research topic which can be achieved using plasmonic structures. This work could be continuing of our study on designing spectrally selective absorber with anisotropic random rough surfaces. Specifically control over bandwidth of narrowband spectrums make it a good candidate to be used in sensor applications.



## BIBLIOGRAPHY

- [1] M.C. Gupta, C. Ungaro, J.J. Foley IV, S.K. Gray, Optical nanostructures design, fabrication, and applications for solar/thermal energy conversion, *Sol. Energy*. 165 (2018) 100–114.
- [2] N. Pirouzfam, K. Sendur, Tungsten Based Spectrally Selective Absorbers with Anisotropic Rough Surface Texture, *Nanomaterials*. 11 (2021) 2018.
- [3] Y. Tian, C.-Y. Zhao, A review of solar collectors and thermal energy storage in solar thermal applications, *Appl. Energy*. 104 (2013) 538–553.
- [4] C. Ferrari, F. Melino, M. Pinelli, P.R. Spina, M. Venturini, Overview and status of thermophotovoltaic systems, *Energy Procedia*. 45 (2014) 160–169.
- [5] Y.-F. Huang, S. Chattopadhyay, Y.-J. Jen, C.-Y. Peng, T.-A. Liu, Y.-K. Hsu, C.-L. Pan, H.-C. Lo, C.-H. Hsu, Y.-H. Chang, Improved broadband and quasi-omnidirectional anti-reflection properties with biomimetic silicon nanostructures, *Nat. Nanotechnol.* 2 (2007) 770–774.
- [6] L. Lu, R.E. Simpson, S.K. Valiyaveedu, Active hyperbolic metamaterials: progress, materials and design, *J. Opt.* 20 (2018) 103001.
- [7] E. Rahimi, A.B. Koucheh, K. Sendur, Temperature assisted reflection control using VO<sub>2</sub>/Si core-shell nanoparticles, *Opt. Mater. Express*. 12 (2022) 2974–2981.
- [8] M. Bhushan, R. Jha, R. Bhardwaj, Reduced band gap and diffusion controlled spherical n-type ZnS nanoparticles for absorption of UV-Vis region of solar spectrum, *J. Phys. Chem. Solids*. 135 (2019) 109021.
- [9] H.Y. Lee, M.M. Al Ezzi, N. Raghuvanshi, J.Y. Chung, K. Watanabe, T. Taniguchi, S. Garaj, S. Adam, S. Gradecak, Tunable Optical Properties of Thin Films Controlled by the Interface Twist Angle, *Nano Lett.* 21 (2021) 2832–2839.
- [10] A.B. Koucheh, M.A. Kecebas, K. Sendur, Impedance mismatch-based enhancement of broadband reflectance of tungsten with bio-inspired multilayers, *J. Quant. Spectrosc. Radiat. Transf.* 276 (2021) 107899.
- [11] S. Wijewardane, D.Y. Goswami, A review on surface control of thermal radiation by paints and coatings for new energy applications, *Renew. Sustain. Energy Rev.* 16 (2012) 1863–1873.

- [12] M.A. Kecebas, N. Pirouzfam, K. Sendur, Origins of the enhanced broadband absorption in black silicon, *J. Appl. Phys.* 129 (2021) 163103.
- [13] M. Rycenga, C.M. Cobley, J. Zeng, W. Li, C.H. Moran, Q. Zhang, D. Qin, Y. Xia, Controlling the synthesis and assembly of silver nanostructures for plasmonic applications, *Chem. Rev.* 111 (2011) 3669–3712.
- [14] C.P. De Castro, M. Luković, R.F.S. Andrade, H.J. Herrmann, The influence of statistical properties of Fourier coefficients on random Gaussian surfaces, *Sci. Rep.* 7 (2017) 1–8.
- [15] I. Rytöluoto, A. Gitsas, S. Pasanen, K. Lahti, Effect of film structure and morphology on the dielectric breakdown characteristics of cast and biaxially oriented polypropylene films, *Eur. Polym. J.* 95 (2017) 606–624.
- [16] S.F. Tian, L.T. Jiang, Q. Guo, G.H. Wu, Effect of surface roughness on tribological properties of TiB<sub>2</sub>/Al composites, *Mater. Des.* 53 (2014) 129–136.
- [17] N. Billot, T. Günther, D. Schreiner, R. Stahl, J. Kranner, M. Beyer, G. Reinhart, Investigation of the adhesion strength along the electrode manufacturing process for improved lithium-ion anodes, *Energy Technol.* 8 (2020) 1801136.
- [18] S.B. Dworkin, T.J. Nye, Image processing for machine vision measurement of hot formed parts, *J. Mater. Process. Technol.* 174 (2006) 1–6.
- [19] D. Bračun, G. Škulj, M. Kadiš, Spectral selective and difference imaging laser triangulation measurement system for on line measurement of large hot workpieces in precision open die forging, *Int. J. Adv. Manuf. Technol.* 90 (2017) 917–926.
- [20] C.S. Goldenstein, R.M. Spearrin, J.B. Jeffries, R.K. Hanson, Infrared laser-absorption sensing for combustion gases, *Prog. Energy Combust. Sci.* 60 (2017) 132–176.
- [21] J.J. Talghader, A.S. Gawarikar, R.P. Shea, Spectral selectivity in infrared thermal detection, *Light Sci. Appl.* 1 (2012) e24–e24.
- [22] J.A. Ratches, R.H. Vollmerhausen, R.G. Driggers, Target acquisition performance modeling of infrared imaging systems: past, present, and future, *IEEE Sens. J.* 1 (2001) 31–40.
- [23] F. Cao, K. McEnaney, G. Chen, Z. Ren, A review of cermet-based spectrally selective solar absorbers, *Energy Environ. Sci.* 7 (2014) 1615–1627.
- [24] H. Kim, H. Kim, J. Ha, N. Park, S. Yoo, Empowering semi-transparent solar cells with thermal-mirror functionality, *Adv. Energy Mater.* 6 (2016) 1502466.
- [25] A. Makki, S. Omer, H. Sabir, Advancements in hybrid photovoltaic systems for enhanced solar cells performance, *Renew. Sustain. Energy Rev.* 41 (2015) 658–684.
- [26] M.F. Modest, S. Mazumder, Radiative heat transfer, Academic press, 2021.
- [27] Z.M. Zhang, Z.M. Zhang, Luby, Nano/microscale heat transfer, Springer, 2007.
- [28] G.A. Meehl, C. Tebaldi, More intense, more frequent, and longer lasting heat waves in the 21st century, *Science* (80-. ). 305 (2004) 994–997.

- [29] X. Han, K. He, Z. He, Z. Zhang, Tungsten-based highly selective solar absorber using simple nanodisk array, *Opt. Express*. 25 (2017) A1072–A1078.
- [30] K.P. Sibin, S. John, H.C. Barshilia, Control of thermal emittance of stainless steel using sputtered tungsten thin films for solar thermal power applications, *Sol. Energy Mater. Sol. Cells*. 133 (2015) 1–7.
- [31] F. Cao, D. Kraemer, T. Sun, Y. Lan, G. Chen, Z. Ren, Enhanced Thermal Stability of W-Ni-Al<sub>2</sub>O<sub>3</sub> Cermet-Based Spectrally Selective Solar Absorbers with Tungsten Infrared Reflectors, *Adv. Energy Mater.* 5 (2015) 1401042.
- [32] G. Silva-Oelker, C. Jerez-Hanckes, P. Fay, High-temperature tungsten-hafnia optimized selective thermal emitters for thermophotovoltaic applications, *J. Quant. Spectrosc. Radiat. Transf.* 231 (2019) 61–68.
- [33] A. Khan, R. Elliman, C. Corr, J.J.H. Lim, A. Forrest, P. Mummery, L.M. Evans, Effect of rhenium irradiations on the mechanical properties of tungsten for nuclear fusion applications, *J. Nucl. Mater.* 477 (2016) 42–49.
- [34] M. Rieth, S.L. Dudarev, S.M.G. De Vicente, J. Aktaa, T. Ahlgren, S. Antusch, D.E.J. Armstrong, M. Balden, N. Baluc, M.-F. Barthe, Recent progress in research on tungsten materials for nuclear fusion applications in Europe, *J. Nucl. Mater.* 432 (2013) 482–500.
- [35] G. Marinelli, F. Martina, H. Lewtas, D. Hancock, S. Mehraban, N. Lavery, S. Ganguly, S. Williams, Microstructure and thermal properties of unalloyed tungsten deposited by Wire+ Arc Additive Manufacture, *J. Nucl. Mater.* 522 (2019) 45–53.
- [36] R. Liu, Z. Wang, T. Sparks, F. Liou, J. Newkirk, Aerospace applications of laser additive manufacturing, in: *Laser Addit. Manuf.*, Elsevier, 2017: pp. 351–371.
- [37] C. Ungaro, S.K. Gray, M.C. Gupta, Black tungsten for solar power generation, *Appl. Phys. Lett.* 103 (2013) 71105.
- [38] H. Wang, L. Wang, Perfect selective metamaterial solar absorbers, *Opt. Express*. 21 (2013) A1078–A1093.
- [39] J. Song, M. Si, Q. Cheng, Z. Luo, Two-dimensional trilayer grating with a metal/insulator/metal structure as a thermophotovoltaic emitter, *Appl. Opt.* 55 (2016) 1284–1290.
- [40] H. Zhang, M. Luo, Y. Zhou, Y. Ji, L. Chen, Ultra-broadband, polarization-independent, wide-angle near-perfect absorber incorporating a one-dimensional meta-surface with refractory materials from UV to the near-infrared region, *Opt. Mater. Express*. 10 (2020) 484–491.
- [41] A.D. Rakić, A.B. Djurišić, J.M. Elazar, M.L. Majewski, Optical properties of metallic films for vertical-cavity optoelectronic devices, *Appl. Opt.* 37 (1998) 5271–5283.
- [42] E. Rephaeli, S. Fan, Tungsten black absorber for solar light with wide angular operation range, *Appl. Phys. Lett.* 92 (2008) 211107.

- [43] V. Rinnerbauer, A. Lenert, D.M. Bierman, Y.X. Yeng, W.R. Chan, R.D. Geil, J.J. Senkevich, J.D. Joannopoulos, E.N. Wang, M. Soljačić, Metallic photonic crystal absorber-emitter for efficient spectral control in high-temperature solar thermophotovoltaics, *Adv. Energy Mater.* 4 (2014) 1400334.
- [44] I. Celanovic, N. Jovanovic, J. Kassakian, Two-dimensional tungsten photonic crystals as selective thermal emitters, *Appl. Phys. Lett.* 92 (2008) 193101.
- [45] H. Wang, V.P. Sivan, A. Mitchell, G. Rosengarten, P. Phelan, L. Wang, Highly efficient selective metamaterial absorber for high-temperature solar thermal energy harvesting, *Sol. Energy Mater. Sol. Cells.* 137 (2015) 235–242.
- [46] I.E. Khodasevych, L. Wang, A. Mitchell, G. Rosengarten, Micro and nanostructured surfaces for selective solar absorption. *Adv Opt Mater* 3: 852–881, (2015).
- [47] A.A. Shah, M.C. Gupta, Spectral selective surfaces for concentrated solar power receivers by laser sintering of tungsten micro and nano particles, *Sol. Energy Mater. Sol. Cells.* 117 (2013) 489–493.
- [48] M.A. Kecebas, M.P. Menguc, A. Kosar, K. Sendur, Spectrally selective filter design for passive radiative cooling, *JOSA B.* 37 (2020) 1173–1182.
- [49] M.C. Gupta, D.E. Carlson, Laser processing of materials for renewable energy applications, *MRS Energy Sustain.* 2 (2015).
- [50] H.-J. Jeong, Y.-C. Kim, S.K. Lee, J.-H. Yun, J.-H. Jang, Enhanced spectral response of CIGS solar cells with anti-reflective subwavelength structures and quantum dots, *Sol. Energy Mater. Sol. Cells.* 194 (2019) 177–183.
- [51] A. Benamira, S. Pattanaik, Application of the Transfer Matrix Method to Anti-reflective Coating Rendering, in: *Comput. Graph. Int. Conf.*, Springer, 2020: pp. 83–95.
- [52] D.S. Hobbs, Random texture anti-reflection optical surface treatment, (2012).
- [53] C. Cho, H. Kim, S. Jeong, S.-W. Baek, J.-W. Seo, D. Han, K. Kim, Y. Park, S. Yoo, J.-Y. Lee, Random and V-groove texturing for efficient light trapping in organic photovoltaic cells, *Sol. Energy Mater. Sol. Cells.* 115 (2013) 36–41.
- [54] A. Goulas, S. Zhang, J.R. McGhee, D.A. Cadman, W.G. Whittow, J.C. Vardaxoglou, D.S. Engstrøm, Fused filament fabrication of functionally graded polymer composites with variable relative permittivity for microwave devices, *Mater. Des.* (2020) 108871.
- [55] C.M. Carbonaro, R. Corpino, M. Salis, F. Mocci, S.V. Thakkar, C. Olla, P.C. Ricci, On the emission properties of carbon dots: reviewing data and discussing models, *C—Journal Carbon Res.* 5 (2019) 60.
- [56] C. Chen, J. Wang, Y. Gao, Wavelength-Dependent Nonlinear Absorption in Palladium Nanoparticles, *Appl. Sci.* 11 (2021) 1640.
- [57] G. Baffou, F. Cichos, R. Quidant, Applications and challenges of thermoplasmonics, *Nat. Mater.* 19 (2020) 946–958.

- [58] G.P. Zograf, M.I. Petrov, S. V. Makarov, Y.S. Kivshar, All-dielectric thermonanophotonics, *ArXiv Prepr. ArXiv2104.01964*. (2021).
- [59] G.P. Zograf, M.I. Petrov, D.A. Zuev, P.A. Dmitriev, V.A. Milichko, S. V. Makarov, P.A. Belov, Resonant nonplasmonic nanoparticles for efficient temperature-feedback optical heating, *Nano Lett.* 17 (2017) 2945–2952.
- [60] M. Gandolfi, A. Crut, F. Medeghini, T. Stoll, P. Maioli, F. Vallée, F. Banfi, N. Del Fatti, Ultrafast thermo-optical dynamics of plasmonic nanoparticles, *J. Phys. Chem. C.* 122 (2018) 8655–8666.
- [61] S. Ishii, R.P. Sugavaneshwar, T. Nagao, Titanium nitride nanoparticles as plasmonic solar heat transducers, *J. Phys. Chem. C.* 120 (2016) 2343–2348.
- [62] M. Li, T. Lohmuller, J. Feldmann, Optical injection of gold nanoparticles into living cells, *Nano Lett.* 15 (2015) 770–775.
- [63] A. Kristensen, J.K.W. Yang, S.I. Bozhevolnyi, S. Link, P. Nordlander, N.J. Halas, N.A. Mortensen, Plasmonic colour generation, *Nat. Rev. Mater.* 2 (2016) 1–14.
- [64] M. Gandolfi, F. Banfi, C. Glorieux, Optical wavelength dependence of photoacoustic signal of gold nanofluid, *Photoacoustics.* 20 (2020) 100199.
- [65] M. Celebrano, D. Rocco, M. Gandolfi, A. Zilli, F. Rusconi, A. Tognazzi, A. Mazzanti, L. Ghirardini, E.A.A. Pogna, L. Carletti, Optical tuning of dielectric nanoantennas for thermo-optically reconfigurable nonlinear metasurfaces, *Opt. Lett.* 46 (2021) 2453–2456.
- [66] Y. Tian, A. Ghanekar, M. Ricci, M. Hyde, O. Gregory, Y. Zheng, A review of tunable wavelength selectivity of metamaterials in near-field and far-field radiative thermal transport, *Materials (Basel).* 11 (2018) 862.
- [67] Z. Wu, W. Xue, Y. Liu, D. Wei, J. Wang, L. Yin, Y. Wang, X. Liu, Q. Zhang, F. Cao, Toward versatile applications via tuning transition wavelength of the WTa-SiO<sub>2</sub> based spectrally selective absorber, *Sol. Energy.* 202 (2020) 115–122.
- [68] S.D. Calisgan, V. Villanueva-Lopez, V. Rajaram, Z. Qian, S. Kang, S.P. Hernandez-Rivera, M. Rinaldi, Spectroscopic chemical sensing based on narrowband MEMS resonant infrared detectors, in: *2018 IEEE SENSORS, IEEE, 2018*: pp. 1–4.
- [69] B. Zhao, M. Hu, X. Ao, Q. Xuan, G. Pei, Spectrally selective approaches for passive cooling of solar cells: A review, *Appl. Energy.* 262 (2020) 114548.
- [70] F.K. Khosroshahi, H. Ertürk, M.P. Mengüç, Optimization of spectrally selective Si/SiO<sub>2</sub> based filters for thermophotovoltaic devices, *J. Quant. Spectrosc. Radiat. Transf.* 197 (2017) 123–131.
- [71] A. Dan, J. Jyothi, K. Chattopadhyay, H.C. Barshilia, B. Basu, Spectrally selective absorber coating of WAlN/WAlON/Al<sub>2</sub>O<sub>3</sub> for solar thermal applications, *Sol. Energy Mater. Sol. Cells.* 157 (2016) 716–726.
- [72] S. Mehrabi, M.H. Rezaei, A. Zarifkar, Ultra-broadband solar absorber based on multi-

- layer TiN/TiO<sub>2</sub> structure with near-unity absorption, *JOSA B*. 36 (2019) 2602–2609.
- [73] S. Chattopadhyay, Y.F. Huang, Y.J. Jen, a. Ganguly, KH Chen and LC Chen, *Mater. Sci. Eng., R*. 69 (2010) 1–35.
- [74] M.M. Hossain, M. Gu, Radiative cooling: principles, progress, and potentials, *Adv. Sci.* 3 (2016) 1500360.
- [75] D. Zhao, A. Aili, Y. Zhai, S. Xu, G. Tan, X. Yin, R. Yang, Radiative sky cooling: Fundamental principles, materials, and applications, *Appl. Phys. Rev.* 6 (2019) 21306.
- [76] R. Family, M.P. Mengüç, Materials for radiative cooling: a review, *Procedia Environ. Sci.* 38 (2017) 752–759.
- [77] R. Family, M.P. Mengüç, Analysis of sustainable materials for radiative cooling potential of building surfaces, *Sustainability*. 10 (2018) 3049.
- [78] M. Sameti, A. Kasaeian, Numerical simulation of combined solar passive heating and radiative cooling for a building, in: *Build. Simul.*, Springer, 2015: pp. 239–253.
- [79] W. Li, Y. Shi, K. Chen, L. Zhu, S. Fan, A comprehensive photonic approach for solar cell cooling, *Acs Photonics*. 4 (2017) 774–782.
- [80] L. Zhu, A.P. Raman, S. Fan, Radiative cooling of solar absorbers using a visibly transparent photonic crystal thermal blackbody, *Proc. Natl. Acad. Sci.* 112 (2015) 12282–12287.
- [81] G.R. Wagner, W. Maltz, Comparing tablet natural convection cooling efficiency, *Eng. Edge*. 3 (2014) 42–45.
- [82] X. Sun, Y. Sun, Z. Zhou, M.A. Alam, P. Bermel, Radiative sky cooling: fundamental physics, materials, structures, and applications, *Nanophotonics*. 6 (2017) 997–1015.
- [83] E. Rephaeli, S. Fan, Absorber and emitter for solar thermo-photovoltaic systems to achieve efficiency exceeding the Shockley-Queisser limit, *Opt. Express*. 17 (2009) 15145–15159.
- [84] E. Sakr, P. Bermel, Thermophotovoltaics with spectral and angular selective doped-oxide thermal emitters, *Opt. Express*. 25 (2017) A880–A895.
- [85] X. Li, J. Peoples, P. Yao, X. Ruan, Ultrawhite BaSO<sub>4</sub> paints and films for remarkable daytime subambient radiative cooling, *ACS Appl. Mater. Interfaces*. 13 (2021) 21733–21739.
- [86] L. Zhou, J. Rada, H. Song, B. Ooi, Z. Yu, Q. Gan, Colorful surfaces for radiative cooling, *J. Photonics Energy*. 11 (2021) 42107.
- [87] E. Blandre, R.A. Yalçın, K. Joulain, J. Drévillon, Microstructured surfaces for colored and non-colored sky radiative cooling, *Opt. Express*. 28 (2020) 29703–29713.
- [88] A. Didari, M.P. Mengüç, Biomimicry designs for passive optical solutions for nanoscale radiative cooling applications, in: *Nanostructured Thin Film. XI*, SPIE, 2018: pp. 51–57.
- [89] P. Fallahzad, N. Naderi, M.J. Eshraghi, A. Massoudi, Combination of surface texturing and nanostructure coating for reduction of light reflection in ZnO/Si heterojunction thin

- film solar cell, *J. Mater. Sci. Mater. Electron.* 29 (2018) 6289–6296.
- [90] M.A. Kecebas, M.P. Menguc, A. Kosar, K. Sendur, Passive radiative cooling design with broadband optical thin-film filters, *J. Quant. Spectrosc. Radiat. Transf.* 198 (2017) 179–186.
- [91] C. Sheng, Y. An, J. Du, X. Li, Colored radiative cooler under optical Tamm resonance, *ACS Photonics.* 6 (2019) 2545–2552.
- [92] L. Zhu, A. Raman, S. Fan, Color-preserving daytime radiative cooling, *Appl. Phys. Lett.* 103 (2013) 223902.
- [93] G.J. Lee, Y.J. Kim, H.M. Kim, Y.J. Yoo, Y.M. Song, Colored, daytime radiative coolers with thin-film resonators for aesthetic purposes, *Adv. Opt. Mater.* 6 (2018) 1800707.
- [94] R.A. Yalçın, E. Blandre, K. Joulain, J. Drévilion, Daytime radiative cooling with silica fiber network, *Sol. Energy Mater. Sol. Cells.* 206 (2020) 110320.
- [95] T. Lee, J. Jang, H. Jeong, J. Rho, Plasmonic-and dielectric-based structural coloring: from fundamentals to practical applications, *Nano Converg.* 5 (2018) 1–21.
- [96] T. Xu, Y.-K. Wu, X. Luo, L.J. Guo, Plasmonic nanoresonators for high-resolution colour filtering and spectral imaging, *Nat. Commun.* 1 (2010) 1–5.
- [97] M. Zeyghami, D.Y. Goswami, E. Stefanakos, A review of clear sky radiative cooling developments and applications in renewable power systems and passive building cooling, *Sol. Energy Mater. Sol. Cells.* 178 (2018) 115–128.
- [98] J. Kou, Z. Jurado, Z. Chen, S. Fan, A.J. Minnich, Daytime radiative cooling using near-black infrared emitters, *Acs Photonics.* 4 (2017) 626–630.
- [99] E. Rephaeli, A. Raman, S. Fan, Ultrabroadband photonic structures to achieve high-performance daytime radiative cooling, *Nano Lett.* 13 (2013) 1457–1461.
- [100] C. Zou, G. Ren, M.M. Hossain, S. Nirantar, W. Withayachumnankul, T. Ahmed, M. Bhaskaran, S. Sriram, M. Gu, C. Fumeaux, Metal-Loaded dielectric resonator metasurfaces for radiative cooling, *Adv. Opt. Mater.* 5 (2017) 1700460.
- [101] M.M. Hossain, B. Jia, M. Gu, Metamaterials: A metamaterial emitter for highly efficient radiative cooling (advanced optical materials 8/2015), *Adv. Opt. Mater.* 3 (2015) 980.
- [102] L. Novotny, N. Van Hulst, Antennas for light, *Nat. Photonics.* 5 (2011) 83–90.
- [103] A. Ninawe, A. Dhawan, X. Xu, Numerical investigation of a narrowband absorber with a simple structure, *OSA Contin.* 3 (2020) 3582–3594.
- [104] V. Khoshdel, M. Shokooh-Saremi, Increased electric field enhancement and broad wavelength tunability by plasmonic bow-tie nano-antenna based on fractal geometry with grid, *Photonics Nanostructures-Fundamentals Appl.* 35 (2019) 100705.
- [105] C.H. Crouch, J.E. Carey, M. Shen, E. Mazur, F.Y. Genin, Infrared absorption by sulfur-doped silicon formed by femtosecond laser irradiation, *Appl. Phys. A.* 79 (2004) 1635–1641.

- [106] J.E. Carey, C.H. Crouch, M. Shen, E. Mazur, Visible and near-infrared responsivity of femtosecond-laser microstructured silicon photodiodes, *Opt. Lett.* 30 (2005) 1773–1775.
- [107] R. Torres, T.E. Itina, V. Vervisch, M. Halbwx, T. Derrien, T. Sarnet, M. Sentis, J. Ferreira, F. Torregrosa, L. Roux, Study On Laser-Induced Periodic Structures And Photovoltaic Application, in: *AIP Conf. Proc.*, American Institute of Physics, 2010: pp. 576–581.
- [108] A.M. Moloney, L. Wall, A. Mathewson, G. Healy, J.C. Jackson, Novel black silicon PIN photodiodes, in: *Semicond. Photodetectors III*, SPIE, 2006: pp. 94–101.
- [109] J.E. Carey, E. Mazur, High sensitivity silicon-based VIS/NIR photodetectors, in: *Conf. Lasers Electro-Optics, 2004.(CLEO).*, IEEE, 2004: pp. 2-pp.
- [110] Z. Huang, J.E. Carey, M. Liu, X. Guo, E. Mazur, J.C. Campbell, Microstructured silicon photodetector, *Appl. Phys. Lett.* 89 (2006) 33506.
- [111] M.U. Pralle, J.E. Carey, H. Homayoon, S. Alie, J. Sickler, X. Li, J. Jiang, D. Miller, C. Palsule, J. McKee, Black silicon enhanced photodetectors: a path to IR CMOS, in: *Infrared Technol. Appl. XXXVI*, International Society for Optics and Photonics, 2010: p. 76600N.
- [112] M. Halbwx, T. Sarnet, P. Delaporte, M. Sentis, H. Etienne, F. Torregrosa, V. Vervisch, I. Perichaud, S. Martinuzzi, Micro and nano-structuration of silicon by femtosecond laser: Application to silicon photovoltaic cells fabrication, *Thin Solid Films.* 516 (2008) 6791–6795.
- [113] H.-C. Yuan, V.E. Yost, M.R. Page, L. Roybal, B. To, P. Stradins, D.L. Meier, H.M. Branz, Efficient black silicon solar cells with nanoporous anti-reflection made in a single-step liquid etch, in: *2009 34th IEEE Photovolt. Spec. Conf.*, IEEE, 2009: pp. 141–145.
- [114] H.-C. Yuan, V.E. Yost, M.R. Page, P. Stradins, D.L. Meier, H.M. Branz, Efficient black silicon solar cell with a density-graded nanoporous surface: Optical properties, performance limitations, and design rules, *Appl. Phys. Lett.* 95 (2009) 123501.
- [115] L. Hu, G. Chen, Analysis of optical absorption in silicon nanowire arrays for photovoltaic applications, *Nano Lett.* 7 (2007) 3249–3252.
- [116] W. Wang, S. Wu, K. Reinhardt, Y. Lu, S. Chen, Broadband light absorption enhancement in thin-film silicon solar cells, *Nano Lett.* 10 (2010) 2012–2018.
- [117] C. Wu, C.H. Crouch, L. Zhao, J.E. Carey, R. Younkin, J.A. Levinson, E. Mazur, R.M. Farrell, P. Gothoskar, A. Karger, Near-unity below-band-gap absorption by microstructured silicon, *Appl. Phys. Lett.* 78 (2001) 1850–1852.
- [118] H. Jansen, M. de Boer, J. Burger, R. Legtenberg, M. Elwenspoek, The black silicon method II: The effect of mask material and loading on the reactive ion etching of deep silicon trenches, *Microelectron. Eng.* 27 (1995) 475–480.
- [119] T. Gimpel, I. Höger, F. Falk, W. Schade, S. Kontermann, Electron backscatter diffraction on femtosecond laser sulfur hyperdoped silicon, *Appl. Phys. Lett.* 101 (2012) 111911.



- [120] B. Franta, E. Mazur, S.K. Sundaram, Ultrafast laser processing of silicon for photovoltaics, *Int. Mater. Rev.* 63 (2018) 227–240.
- [121] X. Liu, P.R. Coxon, M. Peters, B. Hoex, J.M. Cole, D.J. Fray, Black silicon: fabrication methods, properties and solar energy applications, *Energy Environ. Sci.* 7 (2014) 3223–3263.
- [122] M. Otto, M. Algasinger, H. Branz, B. Gesemann, T. Gimpel, K. Fücksel, T. Käsebier, S. Kontermann, S. Koynov, X. Li, Black silicon photovoltaics, *Adv. Opt. Mater.* 3 (2015) 147–164.
- [123] F. Priolo, T. Gregorkiewicz, M. Galli, T.F. Krauss, Silicon nanostructures for photonics and photovoltaics, *Nat. Nanotechnol.* 9 (2014) 19–32.
- [124] Y. Wang, L. Yang, Y. Liu, Z. Mei, W. Chen, J. Li, H. Liang, A. Kuznetsov, D. Xiaolong, Maskless inverted pyramid texturization of silicon, *Sci. Rep.* 5 (2015) 1–6.
- [125] A.M. Gouda, N.K. Allam, M.A. Swillam, Efficient fabrication methodology of wide angle black silicon for energy harvesting applications, *RSC Adv.* 7 (2017) 26974–26982.
- [126] H. Jansen, H. Gardeniers, M. de Boer, M. Elwenspoek, J. Fluitman, A survey on the reactive ion etching of silicon in microtechnology, *J. Micromechanics Microengineering.* 6 (1996) 14.
- [127] Y. Liu, T. Lai, H. Li, Y. Wang, Z. Mei, H. Liang, Z. Li, F. Zhang, W. Wang, A.Y. Kuznetsov, Nanostructure formation and passivation of large-area black silicon for solar cell applications, *Small.* 8 (2012) 1392–1397.
- [128] S.H. Yueh, R. Kwok, F.K. Li, S. V Nghiem, W.J. Wilson, J.A. Kong, Polarimetric passive remote sensing of ocean wind vectors, *Radio Sci.* 29 (1994) 799–814.
- [129] J.T. Johnson, M. Zhang, Theoretical study of the small slope approximation for ocean polarimetric thermal emission, *IEEE Trans. Geosci. Remote Sens.* 37 (1999) 2305–2316.
- [130] I.K. Sendur, J.T. Johnson, B.A. Baertlein, Analysis of polarimetric IR phenomena for detection of surface mines, in: *Detect. Remediat. Technol. Mines Minelike Targets VI*, SPIE, 2001: pp. 153–163.
- [131] Y. Oh, K. Sarabandi, F.T. Ulaby, An empirical model and an inversion technique for radar scattering from bare soil surfaces, *IEEE Trans. Geosci. Remote Sens.* 30 (1992) 370–381.
- [132] L. Zheng, Y. Ma, S. Chu, S. Wang, B. Qu, L. Xiao, Z. Chen, Q. Gong, Z. Wu, X. Hou, Improved light absorption and charge transport for perovskite solar cells with rough interfaces by sequential deposition, *Nanoscale.* 6 (2014) 8171–8176.
- [133] H. Savin, P. Repo, G. Von Gastrow, P. Ortega, E. Calle, M. Garín, R. Alcubilla, Black silicon solar cells with interdigitated back-contacts achieve 22.1% efficiency, *Nat. Nanotechnol.* 10 (2015) 624–628.
- [134] H. Raether, Surface plasmons on smooth surfaces, in: *Surf. Plasmons Smooth Rough Surfaces Gratings*, Springer, 1988: pp. 4–39.

- [135] A. Hoffmann, Z. Lenkefi, Z. Szentirmay, Effect of roughness on surface plasmon scattering in gold films, *J. Phys. Condens. Matter.* 10 (1998) 5503.
- [136] G.A. Farias, A.A. Maradudin, Surface plasmons on a randomly rough surface, *Phys. Rev. B.* 28 (1983) 5675.
- [137] S. Ma, S. Liu, Q. Xu, J. Xu, R. Lu, Y. Liu, Z. Zhong, A theoretical study on the optical properties of black silicon, *AIP Adv.* 8 (2018) 35010.
- [138] K. Gorgulu, A. Gok, M. Yilmaz, K. Topalli, N. Bıyıklı, A.K. Okyay, All-silicon ultra-broadband infrared light absorbers, *Sci. Rep.* 6 (2016) 1–7.
- [139] Y.-B. Chen, Z.M. Zhang, Heavily doped silicon complex gratings as wavelength-selective absorbing surfaces, *J. Phys. D. Appl. Phys.* 41 (2008) 95406.
- [140] P. Bouchon, C. Koechlin, F. Pardo, R. Häıdar, J.-L. Pelouard, Wideband omnidirectional infrared absorber with a patchwork of plasmonic nanoantennas, *Opt. Lett.* 37 (2012) 1038–1040.
- [141] H. Tan, R. Santbergen, A.H.M. Smets, M. Zeman, Plasmonic light trapping in thin-film silicon solar cells with improved self-assembled silver nanoparticles, *Nano Lett.* 12 (2012) 4070–4076.
- [142] D. Bergström, J. Powell, A.F.H. Kaplan, The absorption of light by rough metal surfaces— A three-dimensional ray-tracing analysis, *J. Appl. Phys.* 103 (2008) 103515.
- [143] C. Niu, T. Zhu, Y. Lv, Influence of Surface Morphology on Absorptivity of Light-Absorbing Materials, *Int. J. Photoenergy.* 2019 (2019).
- [144] H. Sai, Y. Kanamori, Spectrally selective thermal radiators and absorbers with periodic microstructured surface for high-temperature applications, *Microscale Thermophys. Eng.* 7 (2003) 101–115.
- [145] L. Cao, K. Sendur, Surface Roughness Effects on the Broadband Reflection for Refractory Metals and Polar Dielectrics, *Materials (Basel).* 12 (2019) 3090.
- [146] A. Raza, A.S. Alketbi, R. Devarapalli, H. Li, T. Zhang, Refractory Ultrathin Nanocomposite Solar Absorber with Superior Spectral Selectivity and Thermal Stability, *Adv. Opt. Mater.* 8 (2020) 2000679.
- [147] F. Lumerical, Solutions, (2016).
- [148] E.D. Palik, Handbook of optical constants of solids, Academic press, 1998.
- [149] B. Liu, X. Xia, C. Sun, Scattering properties of solid rough surface of nickel skeleton, *Infrared Phys. Technol.* 93 (2018) 25–33.
- [150] Z. Liu, G. Liu, Z. Huang, X. Liu, G. Fu, Ultra-broadband perfect solar absorber by an ultra-thin refractory titanium nitride meta-surface, *Sol. Energy Mater. Sol. Cells.* 179 (2018) 346–352.
- [151] M. Shimizu, H. Yugami, Thermal radiation control by surface gratings as an advanced cooling system for electronic devices, *J. Therm. Sci. Technol.* 6 (2011) 297–306.

- [152] H. Sai, H. Yugami, Y. Kanamori, K. Hane, Solar selective absorbers based on two-dimensional W surface gratings with submicron periods for high-temperature photothermal conversion, *Sol. Energy Mater. Sol. Cells.* 79 (2003) 35–49.
- [153] I.S. Amiri, V.J. Sorger, P. Yupapin, Zinc Oxide nanowire gratings for light absorption control through polarization manipulation, *Phys. E Low-Dimensional Syst. Nanostructures.* 108 (2019) 68–73.
- [154] S. Wojciechowski, P. Twardowski, T. Chwalczuk, Surface roughness analysis after machining of direct laser deposited tungsten carbide, in: *J. Phys. Conf. Ser.*, IOP Publishing, 2014: p. 12018.
- [155] E. Maleki, S. Bagherifard, M. Bandini, M. Guagliano, Surface post-treatments for metal additive manufacturing: Progress, challenges, and opportunities, *Addit. Manuf.* (2020) 101619.
- [156] S. Hatefi, K. Abou-El-Hossein, Review of single-point diamond turning process in terms of ultra-precision optical surface roughness, *Int. J. Adv. Manuf. Technol.* 106 (2020) 2167–2187.
- [157] A. Ronchi, A. Sterzi, M. Gandolfi, A. Belarouci, C. Giannetti, N. Del Fatti, F. Banfi, G. Ferrini, Discrimination of nano-objects via cluster analysis techniques applied to time-resolved thermo-acoustic microscopy, *Ultrasonics.* 114 (2021) 106403.
- [158] R.L. Voti, G.L. Leahu, S. Gaetani, C. Sibilia, V. Violante, E. Castagna, M. Bertolotti, Light scattering from a rough metal surface: theory and experiment, *JOSA B.* 26 (2009) 1585–1593.
- [159] M.C. Larciprete, M. Centini, R.L. Voti, M. Bertolotti, C. Sibilia, Polarization insensitive infrared absorbing behaviour of one-dimensional multilayer stack: a fractal approach, *Opt. Express.* 22 (2014) A1547–A1552.
- [160] M.C. Larciprete, M. Centini, R.L. Voti, M. Bertolotti, C. Sibilia, Metallic oriented nanowires films for infrared radiation manipulation, *Appl. Phys. A.* 122 (2016) 343.
- [161] A.P. Raman, M.A. Anoma, L. Zhu, E. Rephaeli, S. Fan, Passive radiative cooling below ambient air temperature under direct sunlight, *Nature.* 515 (2014) 540–544.
- [162] M.W. Ribarsky, Titanium dioxide (TiO<sub>2</sub>)(rutile), in: *Handb. Opt. Constants Solids*, Elsevier, 1997: pp. 795–804.
- [163] H.R. Philipp, Silicon dioxide (SiO<sub>2</sub>)(glass), in: *Handb. Opt. Constants Solids*, Elsevier, 1997: pp. 749–763.
- [164] W. Xi, Y. Liu, W. Zhao, R. Hu, X. Luo, Colored radiative cooling: How to balance color display and radiative cooling performance, *Int. J. Therm. Sci.* 170 (2021) 107172.
- [165] R.A. Yalçın, E. Blandre, K. Joulain, J. Drévillon, Colored Radiative Cooling Coatings with Nanoparticles, *ACS Photonics.* 7 (2020) 1312–1322.
- [166] P. Saring, A. Lena Baumann, B. Schlieper-Ludewig, S. Kontermann, W. Schade, M. Seibt,

- Electronic and structural properties of femtosecond laser sulfur hyperdoped silicon pn-junctions, *Appl. Phys. Lett.* 103 (2013) 61904.
- [167] Y. Cui, K.H. Fung, J. Xu, H. Ma, Y. Jin, S. He, N.X. Fang, Ultrabroadband light absorption by a sawtooth anisotropic metamaterial slab, *Nano Lett.* 12 (2012) 1443–1447.
- [168] J. Zhou, A.F. Kaplan, L. Chen, L.J. Guo, Experiment and theory of the broadband absorption by a tapered hyperbolic metamaterial array, *ACS Photonics.* 1 (2014) 618–624.
- [169] P. Akhter, M. Huang, N. Kadakia, W. Spratt, G. Malladi, H. Bakhru, Suppressing light reflection from polycrystalline silicon thin films through surface texturing and silver nanostructures, *J. Appl. Phys.* 116 (2014) 113503.
- [170] J. Boroumand, S. Das, A. Vázquez-Guardado, D. Franklin, D. Chanda, Unified electromagnetic-electronic design of light trapping silicon solar cells, *Sci. Rep.* 6 (2016) 1–10.
- [171] Z.-H. Chen, N. Qiao, Y. Yang, H. Ye, S. Liu, W. Wang, Y. Wang, Enhanced broadband electromagnetic absorption in silicon film with photonic crystal surface and random gold grooves reflector, *Sci. Rep.* 5 (2015) 1–8.
- [172] K. Gorgulu, M. Yilmaz, K. Topalli, A.K. Okyay, Wideband ‘black silicon’ for mid-infrared applications, *J. Opt.* 19 (2017) 65101.
- [173] K.X. Wang, Z. Yu, V. Liu, Y. Cui, S. Fan, Absorption enhancement in ultrathin crystalline silicon solar cells with antireflection and light-trapping nanocone gratings, *Nano Lett.* 12 (2012) 1616–1619.
- [174] L. Novotny, Effective wavelength scaling for optical antennas, *Phys. Rev. Lett.* 98 (2007) 266802.
- [175] T.D.B. Jacobs, T. Junge, L. Pastewka, Quantitative characterization of surface topography using spectral analysis, *Surf. Topogr. Metrol. Prop.* 5 (2017) 13001.
- [176] S.W. Pang, D.D. Rathman, D.J. Silversmith, R.W. Mountain, P.D. DeGraff, Damage induced in Si by ion milling or reactive ion etching, *J. Appl. Phys.* 54 (1983) 3272–3277.
- [177] T.H. Fung, T. Veeken, D. Payne, B. Veetil, A. Polman, M. Abbott, Application and validity of the effective medium approximation to the optical properties of nano-textured silicon coated with a dielectric layer, *Opt. Express.* 27 (2019) 38645–38660.
- [178] F. Marquier, K. Joulain, J.-P. Mulet, R. Carminati, J.-J. Greffet, Engineering infrared emission properties of silicon in the near field and the far field, *Opt. Commun.* 237 (2004) 379–388.
- [179] A.A. Elsayed, Y.M. Sabry, D. Khalil, F. Marty, T. Bourouina, Optical diffuse reflectance of black silicon and its isotropicity, in: 2016 URSI Asia-Pacific Radio Sci. Conf. (URSI AP-RASC), IEEE, 2016: pp. 1944–1946.